TURUN
YLIOPISTO
UNIVERSITY
OF TURKU

# OPTIMIZED PINNING IN HIGH-TEMPERATURE SUPERCONDUCTOR THIN FILMS

Moe Moe Aye

TURUN YLIOPISTON JULKAISUJA – ANNALES UNIVERSITATIS TURKUENSIS
SARJA – SER. AI OSA – TOM. 717 | ASTRONOMICA – CHEMICA – PHYSICA – MATHEMATICA | TURKU 2024

TURUN
YLIOPISTO
UNIVERSITY
OF TURKU

# OPTIMIZED PINNING IN HIGH-TEMPERATURE SUPERCONDUCTOR THIN FILMS

Moe Moe Aye

TURUN YLIOPISTON JULKAISUJA – ANNALES UNIVERSITATIS TURKUENSIS
SARJA – SER. AI OSA – TOM. 717 | ASTRONOMICA – CHEMICA – PHYSICA – MATHEMATICA | TURKU 2024

## University of Turku

Faculty of Science
Department of Physics and Astronomy
Physics
Doctoral Programme in Exact Sciences

## Supervised by

Prof. Petriina Paturi
Wihuri Physical Laboratory
Department of Physics and Astronomy
University of Turku
Turku, Finland

Dr. Hannu Huhtinen
Wihuri Physical Laboratory
Department of Physics and Astronomy
University of Turku
Turku, Finland

## Reviewed by

Prof. Pavlo Mikheenko
Department of Physics
University of Oslo
Oslo, Norway

Dr. Jean-Claude Grivel
Department of Energy Conversion and Storage
Technical University of Denmark
Denmark

## Opponent

Dr. rer. nat. Jens Hänisch
Karlsruhe Institute of Technology
Institute for Technical Physics
Eggenstein-Leopoldshafen
Germany




ISBN 978-951-29-9779-4 (PRINT)
ISBN 978-951-29-9780-0 (PDF)
ISSN 0082-7002 (PRINT)
ISSN 2343-3175 (ONLINE)
Painosalama Oy, Turku, Finland, 2024

UNIVERSITY OF TURKU
Faculty of Science
Department of Physics and Astronomy
Physics
AYE, MOE MOE: Optimized Pinning in High-Temperature Superconductor Thin Films
Doctoral dissertation, 118 pp.
Doctoral Programme in Exact Sciences
August 2024

## ABSTRACT

This doctoral dissertation aims to enhance the critical current density ($J_c$) of high-temperature superconductors (HTS) based on $YBa_2Cu_3O_{7-\delta}$ (YBCO) to maximize their potential. Achieving high $J_c$ in superconductors involves balancing the impact of crystalline perfection on self-field critical current density, $J_c(0)$, and the influence of artificial pinning centers (APCs) on in-field critical current density, $J_c(B)$. The study explores the intricate balance between maximizing pinning efficiency through higher APC density and enhancing crystalline quality in YBCO to optimize $J_c(0)$ and $J_c(B)$. The research aims to find the optimal strain level to stabilize conflicting requirements in APC/YBCO nanocomposite films. Investigations include $BaZrO_3$ (BZO)-doped YBCO thin films on miscut $SrTiO_3$ (STO) substrates, revealing the influence of modified strain produced by the substrate on YBCO and BZO nanorod growth and their impact on critical current densities. The study then extends to superconducting multilayer structures, examining alternating YBCO films doped with different BZO nanocolumn densities and heteromultilayer structures. Experimental outcomes reveal the interplay of crystalline quality and flux pinning, emphasizing the potential of demonstrated multilayer structures to address challenges in achieving optimal $J_c$ for future HTS power applications.

KEYWORDS: BZO-doped YBCO, critical current density, artificial pinning center, vortex pinning, multilayer thin film

TURUN YLIOPISTO
Matemaattis-luonnontieteellinen tiedekunta
Fysiikan ja tähtitieteen laitos
Fysiikka
AYE, MOE MOE: Optimized Pinning in High-Temperature Superconductor Thin Films
Väitöskirja, 118 s.
Fysikaallisten ja kemiallisten tieteiden tohtoriohjelma
Elokuu 2024

## TIIVISTELMÄ

Tämä väitöskirja pyrkii tehostamaan korkean lämpötilan suprajohteiden (HTS), erityisesti $YBa_2Cu_3O_{7-\delta}$ (YBCO), kriittistä virrantiheyttä ($J_c$) niiden potentiaalin maksimoimiseksi. Korkean $J_c$:n saavuttaminen suprajohteessa edellyttää tasapainoa kiteisen täydellisyyden vaikutuksen ja itse kenttäkriittisen virrantiheyden, $J_c(0)$, sekä keinotekoisten lukkiutumiskeskusten (APC) vaikutuksen välillä kentässä kriittisen virrantiheyden, $J_c(B)$, suhteen. Tutkimuksessa tutkitaan hienovaraista tasapainoa, jonka avulla lukkiutumistehokkuutta voidaan maksimoida korkeammalla APC-tiheydellä ja YBCO:n kiteisen laadun tehostamista, jotta $J_c(0)$ ja $J_c(B)$ voidaan optimoida. Tutkimuksen tavoitteena on löytää optimaalinen rasitustaso, joka vakauttaa ristiriitaiset vaatimukset APC/YBCO-nanokomposiittikalvoissa. Tutkimukset sisältävät $BaZrO_3$ (BZO)-doopatut YBCO-ohutkalvot miscut $SrTiO_3$ (STO) substraateilla, paljastaen substraatin tuottaman muokatun rasituksen vaikutuksen YBCO:n ja BZO-nanotankojen kasvuun ja niiden vaikutukseen kriittisen virrantiheyden suhteen. Tutkimus laajenee sitten suprajohtaviin monikerrosrakenteisiin, jotka tarkastelevat vuorottelevia YBCO-kalvoja, joissa on erilaisia BZO-nanopylvästiheyksiä, ja heteromultikerrosrakenteita. Kokeelliset tulokset käsittelevät kiteisen laadun ja vuon lukkiutumisen vuorovaikutusta, korostaen osoitettujen monikerrosrakenteiden potentiaalia ratkaista haasteita optimaalisen $J_c$:n saavuttamisessa tulevaisuuden HTS-sovelluksissa.

ASIASANAT: BZO-dopatut YBCO, kriittinen virrantiheys, synteettinen lukkiutumiskeskus, vorteksi lukkiutumisen, monikerrosohutkalvo

# Acknowledgements

The research related to the thesis was carried out at the Wihuri Physical Laboratory, University of Turku, spanning from 2019 to 2024. The generous financial support from the Jenny and Antti Wihuri Foundation, along with the Doctoral Program of the University of Turku Graduate School, has been invaluable and deeply appreciated. I am thankful to Prof. Pavlo Mikheenko and Dr. Jean-Claude Grivel for their insightful reviewing of my thesis and their valuable feedback, which significantly contributed to its enhancement. Likewise, I extend my thanks to Dr. rer. nat. Jens Hänisch; it is indeed an honor to have you as my opponent. I dedicate my deepest gratitude to Prof. Petriina Paturi for providing me with the opportunity to pursue this PhD research as part of the Magnetism and Superconductivity research group. Her experienced guidance has been invaluable and instrumental in making my thesis possible. I express my sincere gratitude also to Dr. Hannu Huhtinen for his indispensable guidance, support, and insightful contributions throughout the journey of completing my PhD thesis. Furthermore, I am deeply thankful to Dr. Elmeri Rivasto for his collaboration, expertise, and outstanding contributions to this research project, and his kind support and assistance on many occasions during this journey. Special thanks are also dedicated to Dr. Ilari Angervo for always being available to assist me at a moment's notice. I wish to express my gratitude to all my other colleagues in our research group, former and present. Also, I would like to express my deepest gratitude to my Prof. Khin Khin Win (retired) who created to me the opportunity to continue my research career in Finland. Both to my dear families in Finland and Myanmar, I owe an immeasurable debt of gratitude for all your unwavering understanding throughout this challenging journey. Lastly, I dedicate my most profound gratitude to my beloved for all your caring and support; I am truly grateful to have had you by my side on this remarkable journey.

August 2024
*Moe Moe Aye*

...

# Table of Contents

# Abbreviations

| | |
|---|---|
| APCs | Artificial Pinning Centers |
| BZO | $BaZrO_3$ |
| CCs | Coated Conductors |
| CSD | Chemical solution deposition |
| $B_c$ | Critical magnetic field |
| $J_c$ | Critical current density |
| $T_c$ | Critical temperature |
| FWHM | Full-width half-maximum |
| GL | Ginzburg-Landau |
| HTS | High-Temperature Superconductor |
| HTScc | High-Temperature Superconducting coated conductor |
| IBAD | Ion beam assisted deposition |
| IL | Irreversibility line |
| LTS | Low-Temperature Superconductor |
| MOCVD | Metal organic chemical vapor deposition |
| PLD | Pulsed laser deposition |
| PPMS | Physical Property Measurement System |
| RABiTS | Rolling assisted biaxially textured substrate |
| REBCO | Rare earth barium copper oxide |
| STEM | Scanning transmission electron microscopy |
| STO | $SrTiO_3$ |
| W-H | Williamson-Hall |
| XRD | X-ray diffraction |
| YBCO | $YBa_2Cu_3O_{7-\delta}$ |

# List of Original Publications

This dissertation is based on the following original publications, which are referred to in the text by their Roman numerals:

I M. M. Aye, E. Rivasto, M. Z. Khan, H. Rijckaert, H. Palonen, H. Huhtinen, I. Van Driessche and P. Paturi, Multilayering BZO nanocolumns with different defect densities for YBCO high field applications, New Journal of Physics, 2021; 23, 113031

II M. M. Aye, E. Rivasto, H. Rijckaert, H. Palonen, H. Huhtinen, I. Van Driessche and P. Paturi, Optimized $BaZrO_3$ nanorod density in $YBa_2Cu_3O_{6+x}$ matrix for high field applications, Superconductor Science and Technology, 2022; 35, 075006

III M. M. Aye, E. Rivasto, H. Rijckaert, H. Huhtinen, I. Van Driessche and P. Paturi, Controlled BZO nanorod growth and improved flux pinning in YBCO films grown on vicinal STO substrates, Crystal Growth & Design, 2023; 23, 7971

IV M. M. Aye, E. Rivasto, H. Huhtinen and P. Paturi, Enhanced critical current density in heterostructural YBCO/Ca-doped YBCO multilayers, Crystal Growth & Design, 2024; 24, 4545

**Articles relevant to this work but not included in the thesis**

V M. M. Aye, M. Z. Khan, E. Rivasto, J. Tikkanen, H. Huhtinen and P. Paturi, Role of columnar defect size on angular dependent flux pinning properties in YBCO thin films, IEEE Transactions on Applied Superconductivity, 2019; 29, 8000805

VI E. Rivasto, M.Z. Khan, M. Malmivirta, H. Rijckaert, M. M. Aye, T. Hynninen, H. Huhtinen, I. Van Driessche and P. Paturi, Self-assembled nanorods in YBCO matrix – a computational study of their effects on critical current anisotropy, Scientific Reports, 2020; 10, 3169

VII M. M. Aye, E. Rivasto, M. Z. Khan, H. Rijckaert, E. Salojärvi, C. Haalisto, E. Mäkilä, H. Palonen, H. Huhtinen, I. Van Driessche and P. Paturi,

Control of the nanosized defect network in superconducting thin films by target grain size, Scientific Reports, 2021; 11, 6010

VIII M. M. Aye, E. Rivasto, H. Rijckaert, S. Granroth, H. Palonen, H. Huhtinen, I. Van Driessche and P. Paturi, Role of deposition distance on nanorod growth and flux pinning in BZO doped YBCO thin films: Implications for superconducting tapes, ACS Applied Nano Materials, 2022; 5, 18159

IX A. Tuomola, E. Rivasto, M. M. Aye, Y. Zhao, H. Huhtinen and P. Paturi, Defining optimal thickness for maximal self-field $J_c$ in YBCO/$CeO_2$ multilayers grown on buffered metal, Journal of Physics: Condensed Matter, 2023; 35, 475001

X M. M. Aye, E. Rivasto, T. Vaimala, Y. Zhao, H. Huhtinen and P. Paturi, Improved crystalline quality and self-field $J_c$ in sequentially vacuum-multilayered YBCO thin films on buffered metallic templates, IEEE Transactions on Applied Superconductivity, 2023; 33, 6601806

XI E. Rivasto, M. M. Aye, H. Huhtinen and P. Paturi, Enhanced critical current density in optimized high-temperature superconducting bilayer thin films, Journal of Physics: Condensed Matter, 2024; 36, 135702

XII M. M. Aye, E. Rivasto, Y. Zhao, H. Huhtinen and P. Paturi, Enhanced current-carrying capability in YBCO coated conductor bilayers for high-field applications, Physica Scripta, 2024 (Accepted)

XIII T. Vaimala, M. M. Aye, E. Rivasto, Y. Zhao, H. Huhtinen and P. Paturi, Maximizing flux pinning in YBCO coated conductor films for high-field applications, Physica C: Superconductivity and its applications, 2024 (submitted)

# 1 Motivation

In the dynamic landscape of high-temperature superconductors (HTS), a profound paradigm shift has unfolded, challenging preconceived boundaries and unlocking unprecedented possibilities. These remarkable materials have ushered in an era where superconductivity thrives at elevated temperatures, triggering a cascade of transformative effects across diverse technological domains such as electronics, communications, electric power infrastructure, medicine, research, and transportation [1]. The groundbreaking discovery of copper oxide-based superconductors heralded a new era [2], where HTS cables now outperform conventional counterparts, carrying five times more power, boasting zero dc resistance, and offering heightened efficiency. This breakthrough presents a more environmentally friendly alternative to current infrastructure, holding the potential to address the world's growing energy demands in the $21^{st}$ century. Spanning over three decades of focused development, the evolution of HTS has transitioned from cables to second-generation coated conductors (HTScc), promising a future across diverse technological domains characterized by heightened efficiency, reliability, and a steadfast commitment to environmental consciousness [3–5].

The strategic incorporation of pinning centers has propelled HTS into new realms, addressing challenges in applications that demand maximum current density and magnetic field utilization [6–9]. Artificial pinning centers (APCs), notably $BaZrO_3$ (BZO) within nanocomposites [10–13], have been found to self-assemble into $c$-axis aligned 1D APCs within APC/rare earth barium copper oxide (REBCO) nanocomposites, results in robust correlated pinning leading to enhanced critical current density ($J_c$) up to several Teslas at/near 77 K and reduced $J_c$ anisotropy [7, 10, 14–16], and these nanocomposites present a highly promising option for various power applications. During the early stages of coated conductors (CCs), REBCO films' performance on a single crystal was initially viewed as the maximum achievable; however, it significantly falls below the theoretical limit. The critical current density, where superconductivity is disrupted without any extrinsic material issues, is known as the depairing current and is approximately three to four times higher than the best $J_c$ values achieved today on any $YBa_2Cu_3O_{7-\delta}$ (YBCO) film. This revelation opens the possibility of CCs with performances well beyond those of thin YBCO films on a single crystal, showcasing the untapped potential in pushing the boundaries of superconducting capabilities. In the early days of CCs, performance was

often constrained by a lack of understanding and control over the properties of complex materials of REBCO. While advancements have been made in enhancing $J_c$ in APC/REBCO nanocomposites, achieving a mature technology necessitates a deeper understanding and control of the intricate properties of these materials [11, 17, 18]. This includes the preparation of epitaxially grown single crystalline thin films with precisely designed morphology, orientation, density, and APC/REBCO interface.

Addressing critical questions in the realm of HTSs, this study tackles pivotal inquiries within the HTS domain, concentrating on the synchronization of crystalline perfection, attainment of controllable APCs, and the fabrication of high-quality epitaxial nanocomposite films. The primary objectives revolve around understanding how these nanostructures can be effectively incorporated into YBCO materials during processing and which nanostructures offer superior pinning properties. The research explores the potential for further elevating the current-carrying capabilities of HTS materials, with a specific emphasis on their application in coated conductors technology. The study centers on the development of epitaxial HTS thin films using YBCO material combined with a secondary phase material of BZO to probe their superconducting properties. The distinct thin film designs are employed as investigative tools to uncover new experimental findings. Through precise experimentation, this study seeks to unveil new frontiers in high-temperature superconductors, pushing the boundaries of current knowledge and deepening our understanding of intricacies in optimizing these materials for practical applications. Ultimately, this research constitutes a crucial step towards harnessing the full potential of HTS and achieving transformative advancements in superconducting technology.

# 2 Introduction

## 2.1 A quick background of superconductivity

Heike Kamerlingh Onnes' groundbreaking discovery in 1911 transformed the landscape of physics, setting off a wave of exploration into superconductors. Onnes observed a remarkable change in impure mercury samples, reaching a state of zero electrical resistance below 4 K and aptly naming it "superconductivity" [19]. This phenomenon, found in certain materials, enables them to conduct electric current without any resistance, allowing for an infinite flow of electricity without losing energy as heat. Additionally, superconductors showcase the Meissner effect, expelling magnetic fields from their core, a revelation demonstrated by Meissner and Ochsenfeld in 1933 [20]. The delicate balance between superconducting and normal states is characterized by critical parameters—critical temperature ($T_c$), critical magnetic field ($B_c$), and critical current density ($J_c$). Together, these parameters weave the intricate fabric of the superconducting critical surface, illustrated in Figure 1 across various materials. Classified by their reaction to magnetic fields, superconductors can be divided into two categories: the conventional "Type I" and the distinctive "Type II". "Type I" superconductors, often metallic or simple compounds, show superconductivity at very low temperatures, expelling the magnetic field completely below the $H_c$. This expulsion results in perfect diamagnetism, where the magnetization ($M$) and applied field ($H$) are equal but opposite ($\chi = M/H$ = -1 in SI unit). Beyond $H_c$, the material swiftly returns to its normal state. The $H_c$, the critical field to revert a superconductor to normal, is temperature-dependent as follows:

$$H_c(T) \approx H_c(0)[1 - (T/T_c)^2], \tag{1}$$

where $H_c(0)$ is the critical field at absolute zero. Figure 2(b) illustrates the $M$ variation concerning the $H$ for type I and type II superconductors. Most of the elemental superconductors like Pb, Hg, Sn, etc. [21], an alloy (e.g., $TaSi_2$) [22], and a compound (e.g., SiC with heavy B doping) [23] predominantly display type I superconductivity. Type I superconductors typically have lower $T_c < 10$ K and $H_c$ ranging from 5 to 200 mT [21]. Due to their limited $T_c$ and $H_c$ values, type I superconductors find constrained utility.

On the flip side, "Type II" superconductors, encompassing metallic compounds, alloys, and intricate oxide ceramics, uphold superconductivity at elevated temperatures. Type II superconductors feature two critical magnetic fields: the lower critical

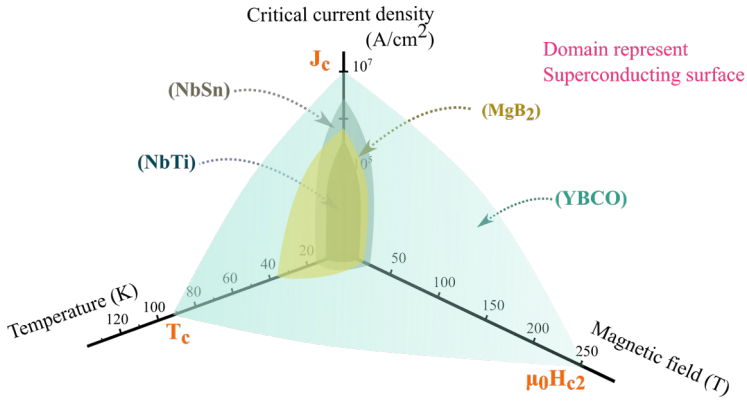


**Figure 1.** Superconducting critical surface of different superconducting materials.

field ($H_{c1}$) and the upper critical field ($H_{c2}$), depicted in Figure 2(a). Below $H_{c1}$, the superconductor mirrors type I, maintaining the Meissner state by wholly expelling magnetic flux. In the range $H_{c1} > H > H_{c2}$, discrete bundles called "flux lines" begin penetrating the sample, rendering it unable to carry a resistanceless current in a perfectly clean sample. Beyond $H_{c2}$, the superconductor transitions into the normal state and Figure 2(b) visually outlines the behavior of both superconductor types under applied magnetic fields. Because of the boasting elevated critical magnetic fields and superior current-carrying capacities, type II superconductors present practical advantages for real-world applications. Conveniently, the classification of type I and type II superconductors can be determined by the Ginzburg-Landau (GL) parameter, $\kappa$, a ratio ($\lambda/\xi$) where $\lambda$ is the penetration depth and $\xi$ is the coherence length. Both lengths scale with temperature, diverging as $(T_c - T)^{-1/2}$ approaching $T_c$. The $GL$ parameter ($\kappa$) acts as a distinctive marker, with type I ($\kappa < 1/\sqrt{2}$) and type II ($\kappa > 1/\sqrt{2}$) superconductors differentiated by this criterion.

## 2.2 High temperature superconductors and their characteristics

The 1986 discovery of cuprate-perovskite ceramic materials by researchers Georg Bednorz and K. Alex Müller, boasting critical temperatures above 30 K, defied expectations and birthed "high-temperature superconductors" [2]. The HTS has revolutionized superconductivity research, breaking free from the constraints of low-temperature superconductors. Unlike traditional ones requiring near absolute zero temperatures, HTS materials exhibit superconductivity at much higher temperatures, ranging from approximately (100–73 K). Typically composed of complex compounds with intricate layered crystal structures and specific elements, HTS materials possess

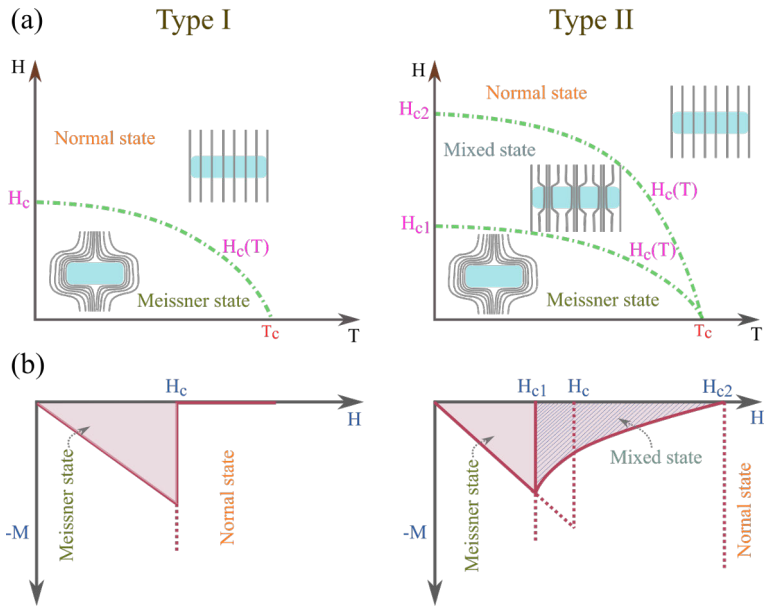


**Figure 2.** (a) Depiction of the $H$–$T$ phase diagram for both type I and type II superconductors. (b) Representation of magnetization variation in response to applied magnetic field for type I and type II superconductors.

distinct properties such as not only perfect diamagnetism but also high critical current densities in magnetic fields. These characteristics set them apart from traditional superconductors. More than three decades since their discovery [24], cuprate HTS remains a focal point in physics, sparking ongoing debates on the mechanism of superconductivity [25, 26].

Prominent HTS materials, including yttrium-barium-copper oxide (YBCO) with a $T_c$ of 92 K [24] and bismuth-strontium-calcium-copper oxide (BSCCO-2223) a $T_c$ of 110 K [25], have proven pivotal and underscore the significance of HTS. As type II superconductors, they demonstrate flux pinning behavior, enabling the trapping of magnetic flux lines within their structure. The ability to pin the vortices equips them to carry high currents under externally applied magnetic fields, making HTS materials highly practical for a diverse range of applications.

In contrast to low-temperature superconductors (LTS), where $T_c$ is influenced by tuning atomic mass and lattice spacing to enhance phonon coupling [27], HTS, like YBCO and iron-based superconductors, do not rely on electron-phonon interactions. HTS materials exhibit a pseudogap above $T_c$, and $T_c$ is determined by intrinsic pairing strength through electron correlations. However, the exact mechanisms governing high-temperature superconductivity remain an active area of research, involving unconventional behaviors, pressure, and doping dependencies. This divergence in

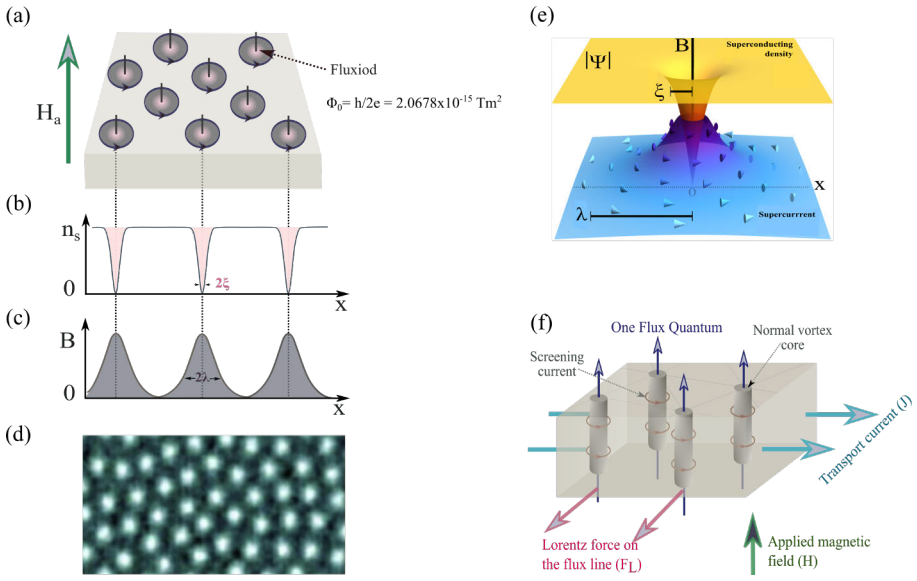


**Figure 3.** Mixed state in a type II superconductor. (a) Magnetic flux penetration within the sample occurs through the formation of small 'tubes' known as vortices, each characterized by a quantized flux $\phi_0 = h/2e$. (b) The variation of superconducting electron concentration changes according to position. (c) Variation of magnetic flux density. (d) When flux enters an ideal type-II superconductor, it gives rise to individual normal vortices surrounded by induced screening currents, leading to the formation of a triangular lattice that serves to minimize energy [28]. (e) The variation of the superconducting order parameter ($\Psi$) and magnetic flux density ($B$) in relation to position ($x$) from the center of an isolated vortex core [29]. (f) A schematic illustration depicts an ideal type-II superconductor subjected to a uniform external magnetic field while carrying a transport current, highlighting its behavior in such conditions.

critical temperature theories reflects the diverse underlying physics in these material classes compared to LTS. In HTS that belong to the type II superconductors, the critical current density is more complex due to the conductor undergoing changes at two field strengths. According to the Ginzburg-Landau theory [30], critical fields for type II superconductors are defined as

$$H_{c1} = \phi_0/4\pi\mu_0\lambda^2 \quad \text{and} \quad H_{c2} = \phi_0/4\pi\mu_0\xi^2, \tag{2}$$

while for type I superconductors, $H_c = \phi_0/4\pi\mu_0\lambda\xi$. In HTS, the extremely high value of $H_{c2}$ (up to 120 T) [31] whereas $H_{c1}$ may be small (several mT), highlighting the significance portion of the mixed state between the critical fields in the phase diagram, which is the regime of technological interest. In this mixed state, vortices emerge when the external magnetic field is between $H_{c1}$ and $H_{c2}$ [32, 33]. These vortices have a normal-conducting core with a diameter of $2\xi$ and are surrounded by circulating supercurrents that decay within a characteristic length, $\lambda$, generating a magnetic flux quantum $\phi_0 = h/2e$ as seen in Figure 3(a-c). The repelling cir-

cular currents give rise to the formation of an ordered hexagonal lattice known as the Abrikosov vortex lattice. This lattice, depicted in Figure 3(d), exhibits a vortex density ($n_v$) scaling proportionally with the applied magnetic field ($H_a$). Figure 3(e) illustrates the magnetic flux density and order parameter magnitudes for an isolated flux line as a function of position away from the vortex core [28]. The magnetic flux density is maximized at the vortex core ($x = 0$), while the order parameter is minimized. The squared magnitude of the order parameter is proportional to the number density of superconducting charge carriers. As the order parameter approaches zero at the origin, indicating the restoration of the normal state, the material fully admits magnetic flux. In the presence of a transport current in the superconductor, vortices interact with it through the Lorentz force ($\mathbf{F}_\mathrm{L} = \mathbf{J} \times \mathbf{B}$), as depicted in Figure 3(f). Due to the non-superconducting nature of the vortex core, their motion causes energy dissipation, rendering the material unable to transport current with zero electrical resistance. Consequently, the capability for resistanceless current flow in HTS is limited, even in the mixed state. However, given specific conditions like pinning the flux line through the introduction of pinning centers into the superconducting body and creating a gradient in the flux line density, it becomes feasible to achieve resistanceless current flow throughout the bulk. For instance, the abundant defects naturally occurring in REBCO films result in significantly elevated $J_\mathrm{c}$ up to 3–7 MA/cm$^2$ at 0 T, 0.02–0.5 MA/cm$^2$ at 1–5 T, in contrast to the low $J_\mathrm{c}$ of single crystals at 77 K [6], whereas polycrystalline bulk samples of YBCO were observed to have very low $J_\mathrm{c}$ ($10^2$ A/cm$^2$).

### 2.2.1 YBCO structure and characteristics

The YBCO compound was first discovered in 1987 [2]. It features a more complex crystallographic structure compared to LTSs, as depicted by the distorted perovskite structure in Figure 4(a-c). Microscopically, YBCO crystallites possess a unit cell with six parallel layers aligned perpendicular to the $c$-axis, consisting of CuO (chain), BaO, $CuO_2$ (plane), Y, $CuO_2$, and BaO. Notably, oxygen sites on the CuO chain can be either partially or completely vacant. Compounds with less than 7 oxygen atoms per formula unit are denoted as $YBa_2Cu_3O_{7-\delta}$, where $\delta$ represents the oxygen deficiency, particularly at the basal plane ($z$ = 0), of the CuO chains.

Exploring the $YBa_2Cu_3O_{7-\delta}$ notation further, when $\delta$ varies from 0 to 1, a notable transition occurs. When $\delta \geq 0.65$, the structure is tetragonal, and $\delta$ = 1 leads to vacant chain oxygen sites, causing a non-superconducting state (see Figure 4(b)). As $\delta$ decreases below the critical point of $\delta$ = 0.65, the structure undergoes an orthorhombic symmetry shift, rendering it superconducting. In the orthorhombic YBCO lattice ($0 \leq \delta \leq 0.65$), oxygen ions are fully ordered, forming a one-dimensional CuO chain oriented parallel to the $b$-axis. Optimal superconducting properties manifest in orthorhombic YBCO when $\delta$ is approximately 0.07 with the

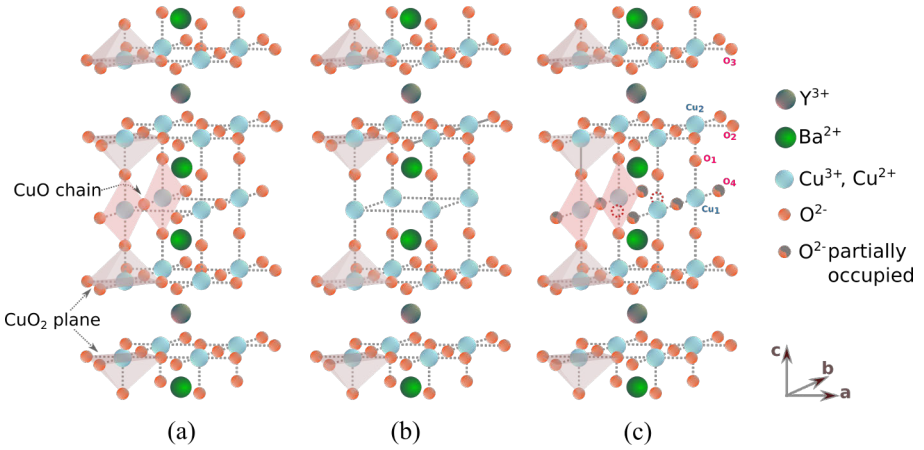


**Figure 4.** Crystal structure of (a) $YBa_2Cu_3O_7$ (b) $YBa_2Cu_3O_6$ (c) $YBa_2Cu_3O_{7-\delta}$. The presence of the CuO chains introduces an orthorhombic distortion of the unit cell [34].

unit cell parameters of $a$ = 3.8185 Å, $b$ = 3.8856 Å, and $c$ = 11.6804 Å [35, 36] and at this point, almost all O4 sites are occupied with few vacancies (see Figure 4(c)).

The charge conduction in YBCO is comprehended by analyzing the valence states of different atoms within the unit cell. The Y and Ba are completely ionized, and assigned +3 and +2 valence, indicating their decoupling from charge conduction. In contrast, Cu and O valence states depend on oxygen deficiency $\delta$. The insulating nature of the oxygen-depleted ($\delta$ = 1) compound implies ionic Cu-O bonds. As oxygen vacancies on the CuO chain are filled, electrons transfer from $CuO_2$ planes to maintain charge neutrality, introducing holes into the $CuO_2$ planes as mobile charge carriers. Experimental verification confirms the transition from insulating to metallic behavior (above $T_c$) and superconductivity (below $T_c$) through hole doping. The charge conduction in both normal and superconducting states primarily occurs in the $CuO_2$ planes, establishing them as conduction slabs, while the CuO chains serve as charge reservoirs. Thus, cuprate superconductors share the common feature of $CuO_2$ conduction slabs and CuO chains as charge reservoirs.

Due to the limited connection between the $CuO_2$ planes and the higher carrier density concentrated within these planes, the transport properties in both the normal and superconducting states display a significant anisotropy. Specifically, the strength of superconductivity is notably weaker along the $c$-axis when compared to the $ab$ planes [37]. Furthermore, the YBCO superconductor displays anisotropic and temperature-dependent characteristics in its $\xi_c$ and $\lambda_c$. Notable approximate values include $\xi_c$ ranging from 0.14 to 0.8 nm, $\xi_{a-b}$ from 1.2 to 4 nm, $\lambda_c$ from 800 to 1121 nm, and $\lambda_{a-b}$ from 150 to 210 nm. These values, distinguished by subscripts indicating lengths along the $c$-axis and the $ab$-plane, respectively, demonstrate

a temperature influence, with lower values at $T$ = 0 K and larger values at $T$ = 77 K [32, 37–40]. The relatively small coherence lengths of YBCO, such as $\xi_{\mathrm{ab}}$ and $\xi_{\mathrm{c}}$ for $T \rightarrow$ 0 K, are comparable to the lattice parameters which present limitations for the percolation of electrical current across grain boundaries [41].

Over the years, advancements in fabrication and processing techniques, including pulsed laser deposition (PLD), chemical solution deposition (CSD), and metal organic chemical vapor deposition (MOCVD), have facilitated the preparation of highly $c$-axis oriented YBCO thin films. This development has significantly enhanced the current carrying capability of YBCO, resulting in a high $J_{\mathrm{c}}$ of 1–5 MA/cm$^2$ at 77 K in a self-field [14]. Moreover, significant progress has been achieved in developing nanoscale APCs in YBCO, enhancing in-field $J_{\mathrm{c}}$ performance. This enhancement, influenced by factors like field orientation and temperature, underscores its promising potential for practical applications in second-generation CCs. Innovative substrate technologies like the rolling assisted biaxially textured substrate (RABiTS) process and ion beam assisted deposition (IBAD) process facilitate the production of long-length, flexible coated conductors with a textured surface. Hence, HTS coated conductors (HTScc) have unequivocally fulfilled the demanding criteria for power applications, while the latest breakthroughs in YBCO coated conductors present unprecedented opportunities for the creation of all-superconducting magnets with the capability to reach magnetic fields surpassing 30 T.

## 2.3 Vortex pinning mechanisms in HTS

Vortex pinning in superconductors involves the immobilization of vortices, also known as flux lines, at defects or irregularities called pinning centers. These pinning centers create a flux pinning force, resisting vortex movement under the influence of the Lorentz force ($F_{\mathrm{L}}$), expressed as pinning force density ($F_{\mathrm{p}}$). Defect sites, energetically surrounded by a barrier, require overcoming this barrier for a pinned vortex to move [32]. The Lorentz force effectively lowers this barrier, reaching a critical current density when the pinning force balances the Lorentz force. If the Lorentz force exceeds the local pinning force, vortex motion occurs, introducing resistance. Global pinning theory suggests that any non-superconducting region of size $d$, equivalent to a few nanometers or approximately the size of a vortex core radius, can act as a pinning center. The pinning energy of a vortex is given by

$$u_p = (B_{\mathrm{c2}}(T)/2\mu_0)\pi\xi_{GL}^2 d, \tag{3}$$

where $B_{\mathrm{c2}}$ is the thermodynamic critical field, and $\xi_{GL}$ is the Ginzburg–Landau coherence length. Each vortex, individually pinned by a non-superconducting core region and with elastic energies considerably smaller than pinning energies, contributes to the $F_{\mathrm{p}}$. This force is calculated by taking into account the individual

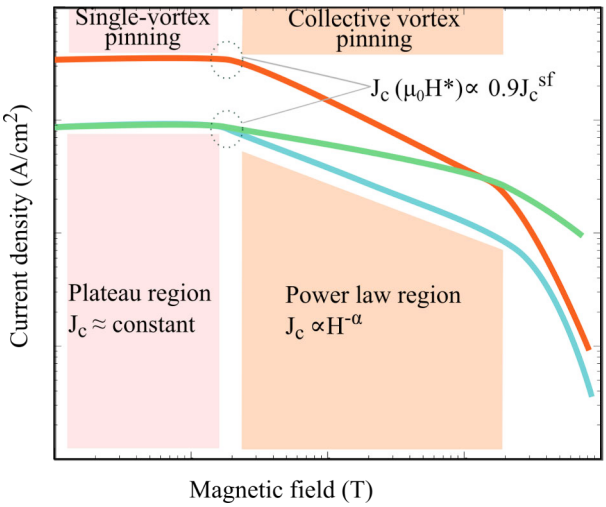


**Figure 5.** An illustration demonstrates the relationship between critical current density ($J_c$) and magnetic field strength, plotted on a log-log scale, highlighting three distinct regions. The $J_c$ in a magnetic field is influenced by three key factors: the self-field value, the extent of the plateau, and the rate of decay beyond the plateau. The light blue and red curves have the same plateau and $\alpha$ but higher $J_c$ in the red curve. The green curve demonstrates an alternative approach to increasing $J_c$ at higher magnetic field strengths, characterized by a lower $\alpha$ value. For PLD YBCO, typical $\alpha$ values range between 0.5 and 0.6, but many enhancement methods aim to reduce $\alpha$ significantly, sometimes achieving values as low as 0.2.

pinning of each vortex [16]

$$F_p = \Sigma f_p = N(a_0 d_p) f_p. \tag{4}$$

Here, $N$ is the density of non-superconducting precipitates, $d_p$ and $a_0$ are the average separation among pinning centers and flux lines, and $f_p$ is the elementary pinning force associated with one vortex pinned by one particle, given by $f_p \approx U/\xi_{GL}$. Note that Eq. (4) assumes that the pinning sites are strong enough to break the vortex lattice [42].

For one vortex pinned at one pinning center, the matching field $H_m = n\phi_0$ illustrates a peak of pinning force density $F_{\mathrm{p,max}}$ corresponding to the field $H_{\mathrm{max}}$, reflecting the pinning strength of the individual center. The peak location $H_{\mathrm{max}}$ is proportional to the concentration of the pinning centers. The global pinning force ($\mathbf{F}_{\mathrm{p}} = \mathbf{J}_{\mathrm{c}} \times \mathbf{B}$) is directly proportional to the $N$, so that the critical current is expressed by

$$J_{\mathrm{c}} = (NB_{c2}/2\mu_0 B)\pi\xi_{GL} d. \tag{5}$$

Empirically, the $J_{\mathrm{c}}$ as a function of the magnetic field is described by three regions in a log $J_{\mathrm{c}}$ vs. log $H$ plot [43], as seen in Figure 5. The accommodation

field ($B^*$) marks the transition from a low-field single vortex pinning regime to a higher slope, indicating collective pinning. The presence of $B^*$ is defined as the magnetic field fulfilling the relation $J_c(B^*)/J_c(0) = 0.9$ [44, 45], signaling a change in dominant pinning mechanisms with magnetic field and temperature. Below $B^*$, the significant influence of crystalline quality results in $J_c$ being nearly independent of the applied magnetic field [46]. The magnitude of $B^*$ correlates with the prevailing high defect density, usually remaining below a few tesla [43, 47]. Above $B^*$, vortex-vortex interaction becomes important, and $J_c$ degradation follows a power-law dependence [43, 47–49], $J_c(B) \propto B^{-\alpha}$. The power-law exponent $\alpha$, indicative of the field dependence of $J_c$, varies with the dominant pinning mechanism and tends to decrease with increasing pinning strength.

### 2.3.1 Vortices' characteristics in HTS

In HTSs, vortices interacting with structural defects exhibit distinct phases, as depicted in Figure 6. The phase diagram of vortices in superconductors displays a varied spectrum of ordered, glassy, liquid, and dynamic states, influenced by three competing effects. The repulsive vortex-vortex interaction promotes ordered vortex lattices, the attractive vortex–pinning site interaction induces disordered glassy vortex states, and thermal fluctuations transform the vortex lattice into a liquid state. In nearly defect-free crystals at low temperatures, an Abrikosov vortex lattice forms with very low critical current density. The introduction of weak random point defects leads to a vortex glass state, marked by broken symmetry and high critical currents due to pinning [50–52]. Correlated disorder may result in a Bose glass state [53]. At lower temperatures and fields, vortices freeze into various solid phases, including different types of "glasses" [51, 53].

At higher temperatures, thermal energy prevails, transitioning the solid phase into a liquid state depicted by the melting line, known as the irreversibility line (IL), in Figure 6 [51, 55, 56]. In the liquid phase, reduced pinning allows vortices to flow around defects, resembling electrical resistance in a normal metal. Above the IL, a finite order parameter corresponds to easy flux motion, while below the IL, effective flux pinning defines the transition to a vortex liquid state with zero resistance. Hence, the $J_c$ generally decreases with rising temperature and magnetic field, reaching zero at the irreversibility line, $H_{irr}(T)$. Above this line, loss-free current transport becomes impossible. In HTS, the higher transition temperatures and anisotropy result in significant influence from thermal fluctuations on vortex dynamics [51, 53, 56] leading to the unique characteristic results in a substantial portion of the phase diagram occupied by the vortex liquid. Additionally, the orientation of the applied magnetic field strongly influences vortex properties, depending on the material's anisotropy, often arising from a layered stacking structure.

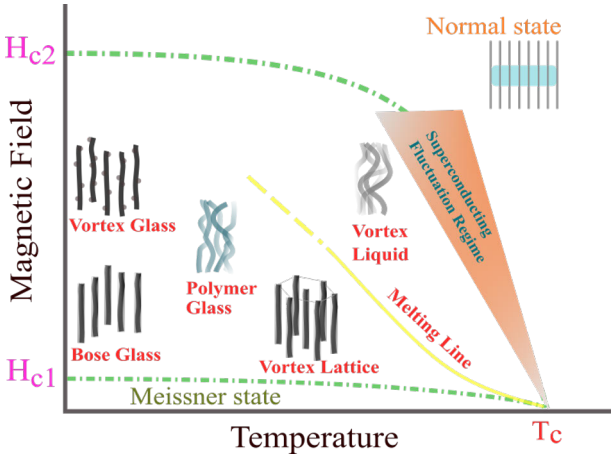


**Figure 6.** Schematic representation of a magnetic phase diagram for HTS, showing the different vortex phases that may appear [54].

### 2.3.2 Types of vortex pinning

In HTS, the pinning force primarily stems from natural and artificial mechanisms. Natural pinning arises from inherent lattice imperfections like antiphase boundaries, grain boundaries, stacking faults [43, 57–60], voids, impurities, dislocations [43], oxygen vacancies, and twins [61–63] in materials like epitaxial YBCO films fabricated by PLD [64] or chemical pathways such as trifluoroacetate-metal oxide deposition (TFA-MOD) [65] and MOCVD [66]. These defects act as spontaneous pinning centers, enhancing vortex pinning. Intrinsic pinning is more effective at lower temperatures ($T < 77$ K), where the $\xi_c$ becomes much smaller than the insulating block distance [67], and is most efficient when the magnetic field is applied parallel to the $ab$-plane. Despite their low density, these growth defects provide robust vortex pinning for applied magnetic fields up to 1–2 T, classifying them as weak pinning centers [68]. For YBCO, self-field critical current density ($J_{\mathrm{c,self}}$) typically reaches a few MA/cm$^2$ at zero magnetic field but experiences a tenfold reduction at around 1 T, posing challenges for high-field applications.

In HTS, APCs are intentionally introduced defects, inclusions, or structures designed to trap and immobilize magnetic flux vortices. Global pinning theory posits that an APC can be any non-superconducting region, characterized by a size $d$ equivalent to a few nanometers or approximately matching the vortex core radius. These can include nanoparticles, nanorods, defects, magnetic inclusions, etched patterns, and various engineered microstructures. Acting as obstacles for magnetic flux vortices, these APCs enhance the critical current density of the superconductor. Engineered pinning centers offer tunability in size, shape, and distribution, providing precise customization beyond the capabilities of natural defects. The uniform dis-

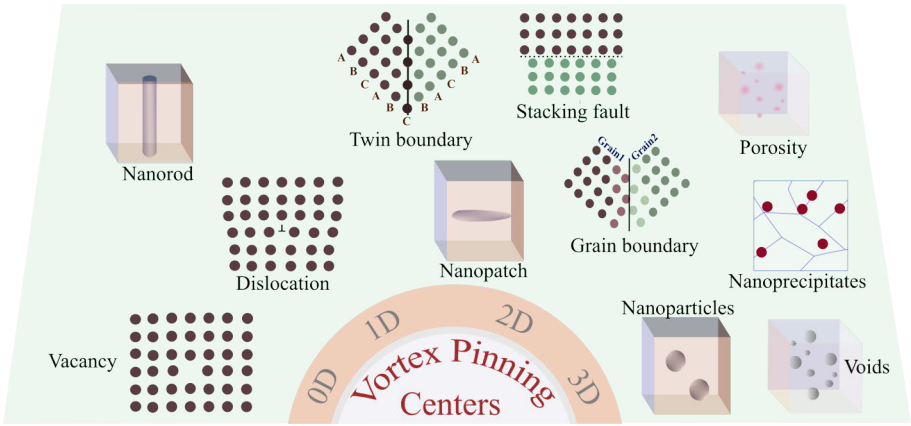


**Figure 7.** Classification of defects in crystals based on dimensionality.

tribution ensures consistent improvements, and their reduced sensitivity to external conditions enhances overall stability. Additionally, the design flexibility allows for higher operating temperatures, expanding the practical temperature range of HTS materials.

Based on size and shape of pinning center in HTS, added pinning centers are categorized into zero-dimensional (0D), like oxygen vacancies and cation disorder, one-dimensional (1D) structures such as dislocations and columnar defects, two-dimensional (2D) features like twin boundaries and grain boundaries, and three-dimensional (3D) pins like nanoparticles or precipitates [6], seen in Figure 7. The small size of 0D pins provides crucial pinning mainly at low temperatures, but their high density makes them valuable for very high field use. The 1D column pinning shows a much stronger enhancement of $J_c$ and $H_{irr}$ at high temperatures, especially when the pinning center is parallel to the magnetic field direction [69, 70]. The 2D planar pins, such as those induced by antiphase boundaries in YBCO films, exhibit strong enhancement in $J_c$ values due to their large interaction interface [71]. The 3D pins, represented by nanoparticles or precipitates, prove most effective for improving $J_c$ over the full angular range due to their strong and isotropic pinning [15, 65, 72–80]. Notably, significant efforts have been made to introduce additional pinning centers with specific properties, focusing on the tunability and controllability of pinning disorder.

## 2.4 Overview of existing techniques for vortex pinning in HTS

In the pursuit of enhancing superconductor performance, particularly HTS, various critical pinning techniques have been developed. These techniques involve inten-

tional modifications such as introducing magnetic centers, chemical doping, ion irradiation, nanostructuring, self-assembled nanoparticles, and geometric features.

- Magnetic pinning centers, including ferromagnetic or superparamagnetic particles, can be incorporated into HTS to create effective pinning sites [81].
- Chemical doping entails introducing specific elements or compounds into the crystal structure of HTS, altering electronic properties, and generating defects that serve as pinning sites for vortices [82, 83].
- Ion irradiation involves bombarding HTS material with high-energy ions, inducing lattice defects and disorder, thereby enhancing resistance to vortex motion [84].
- Nanostructuring, introducing nanoscale defects or inclusions within the HTS material, is a powerful pinning technique, offering numerous pinning sites due to high surface area and controlled distribution [70, 85].
- Self-assembly techniques arrange ordered arrays of pinning centers within HTS materials, utilizing natural or induced forces [86, 87].
- Nanostructure patterning involves creating specific patterns or arrays of defects on the material's surface, acting as pinning centers for vortices [88].

Moreover, advanced simulation and modeling techniques are indispensable for the progress of high-temperature superconductor research. They empower researchers to predict material properties and optimize experimental parameters, facilitating the design of superconducting materials and providing a deeper comprehension of superconductivity's underlying mechanisms. These techniques encompass modeling and analyzing various facets of superconducting materials, including vortex pinning, defects, impurities, and external perturbations. For instance, Ginzburg-Landau (GL), Molecular dynamics (MD), and Monte Carlo (MC) simulations form a comprehensive toolkit for designing pinning landscapes in high-performance superconductors [46, 89]. Looking ahead, the integration of state-of-the-art machine learning and artificial intelligence algorithms holds promise for automating the prediction of optimal pinning landscapes and the synthesis protocols, ultimately determining resulting critical currents [90].

### 2.4.1 Self-assembled pinning centers

It is generally accepted that the strain distribution within the crystal plays a critical role in the self-assembly APCs in YBCO film, especially concerning nucleation sites like BZO [16, 87]. Epitaxial APC/REBCO nanocomposite films, grown layer by layer through *in situ* deposition processes like PLD, sputtering, and MOCVD, exhibit

phase segregation of impurity APC materials from the REBCO matrix during the initial growth stage. This results in three primary strain interfaces at APC/REBCO, APC/substrate, and REBCO/substrate interfaces, stemming from the mismatch between crystal lattices of the materials involved, requiring forced strain to accommodate them. The strain field generated acts as the driving force for the strain-mediated self-organization of APCs in APC/RE-123 nanocomposites [87]. This process leads to the formation of self-assembled nanostructures, including randomly oriented nanoparticles, nanocolumns, and vertical arrays of nanocolumns within the YBCO matrix through the influence of various secondary phases. The morphology, dimensionality, and orientation of self-assembled APCs are shaped by an optimal level of interfacial strain, with a suggested lattice mismatch range of 5–12 % for superior 1D vortex pinning [91]. Additionally, higher concentrations of APC dopants enhance defect density, improving pinning at higher magnetic field intensities [92]. However, the reduced nanorod separation introduces microstructural interactions between the inclusions.

Studies reveal that columnar APCs grown along the $c$-axis of REBCO films exhibit robust vortex pinning, resulting in high $J_\mathrm{c}$ when the magnetic field aligns with the $c$-axis up to several teslas at/near 77 K [7, 10, 14] and also reduced anisotropy [7, 14, 70, 93–95]. Correlated pinning is enhanced at $B \parallel c$-axis if $B$ is comparable to or less than the field $B_{max} = n_{1\mathrm{D}}\Phi_0$, where $n_{1\mathrm{D}}$ is the areal concentration of 1D APCs. Goyal et. al. reported the vertical alignment of self-assembled BZO columnar phases in YBCO films, enhancing pinning along the $c$-axis direction due to the high lattice mismatch between BZO and YBCO, resulting in a high defect density semi-coherent BZO/YBCO heterointerface [87, 91, 96]. While the strain-mediated mechanism aligns with the observed self-assembly of BZO nanorods, the growth mechanisms governing the alignment direction, size, and nearly cylindrical shape of the inclusions remain not fully understood, leaving some questions unanswered.

### 2.4.2 Challenges and constraints in current pinning techniques

Advancements in pinning techniques for HTSs have indeed been impressive. However, there are several notable challenges and limitations that researchers and engineers encounter while optimizing these materials for practical applications. Firstly, the complexity of HTS materials, often composed of intricate compounds with complex crystal structures, presents a challenge [97, 98]. Introducing pinning centers can disrupt the delicate balance within the material, potentially affecting its superconducting properties. Striking the right balance between enhanced pinning and maintaining desired superconducting characteristics is a significant challenge. Secondly, determining the optimal density of pinning sites is a non-trivial task. Too few pinning sites may not effectively trap vortices, while too many can result excessive doping, which reduces the effective superconducting area and induces strain in

YBCO, hindering superconductivity [7, 10, 99]. Finding the right balance is highly application and material-dependent, making it a challenging optimization problem.

Thirdly, materials engineerings, such as creating and incorporating nanoscale pinning centers or tailored dopants, can be technically demanding and costly [100]. The precise engineering of these materials requires sophisticated techniques and equipment, limiting their widespread adoption, especially in resource-constrained environments. For instance, ion irradiation, although effective in creating pinning defects, can also cause structural damage to the HTS material [84]. Excessive irradiation can degrade the superconducting properties, necessitating careful control and optimization of irradiation parameters. Moreover, the effectiveness of pinning centers in HTS materials can be temperature and magnetic field dependent, which limits their versatility across different operating conditions. Accurate control over the size and distribution of nanoscale pinning centers can be challenging, impacting the reproducibility and reliability of HTS materials. The production of HTS materials with optimized pinning configurations can be costly, and scaling up manufacturing processes while maintaining desired properties remains a challenge, particularly for large-scale applications like power transmission. Finally, advanced simulations and modeling to predict optimal pinning configurations can be computationally intensive, requiring significant computational resources and expertise [46, 89, 90].

## 2.5 Current research challenges and limitations

To maximize the absolute critical current density $J_\mathrm{c}$ of YBCO thin films and coated conductors at high magnetic fields favourable for electric power applications [10, 37, 101–103], requirements of both the high crystalline quality and optimal flux pinning properties should be fulfilled [46, 104, 105]. The value of $J_\mathrm{c}$ under the high-field range can be substantially increased by enhancing the vortex pinning via increased APC within the superconducting lattice [106]. However, the addition of any impurities within the superconducting lattice (doping) always degrades the overall superconducting properties seen as substantially reduced $J_\mathrm{c}(0)$ along with superconducting transition temperature [14, 107, 108]. In particular, we have previously observed that the concentration of the BZO nanorods has been observed to degrade the $J_\mathrm{c}(0)$ in a linear manner [96].

As illustrated in Figure 8, the improvement in $J_c$ in the in-field region, facilitated by the optimized pinning from the BZO nanorod columnar network in the YBCO film, is considerable [14, 48, 87, 111], yet it does not signify the overall maximized $J_c$, given the significant decrease in zero-field critical current density compared to a pure YBCO film [16, 42, 46, 112, 113]. Thus, it is crucial to address this aspect attentively. In the zero- and low-field applications below $\approx 100\,\mathrm{mT}$, the crystalline structure of YBCO is solely responsible for maximum $J_\mathrm{c}$ and in the mid-field applications between 100 mT and $\approx 2\,\mathrm{T}$, the $J_\mathrm{c}$ at the zero-field unambiguously limits the

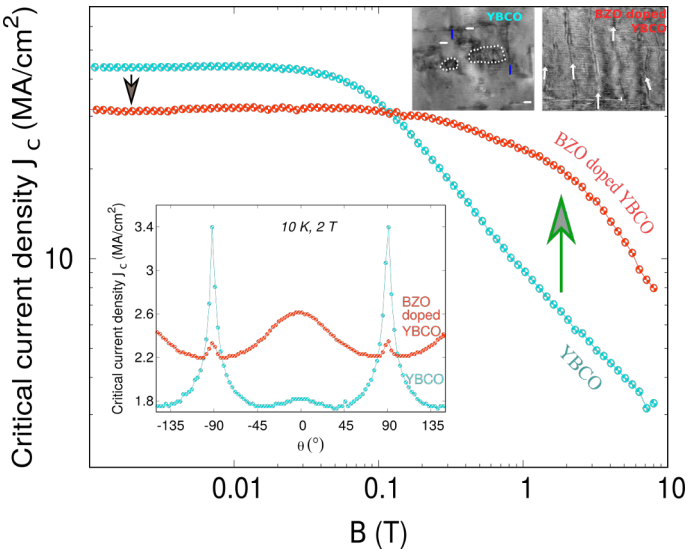


**Figure 8.** The $J_c$ dependence on magnetic field for YBCO and BZO doped YBCO thin films on STO(100) substrate is presented, recorded at 10 K. TEM images of both films are displayed in the top right corner. The inset figure illustrates their angular $J_c$ dependence at 2 T. Notably, the YBCO film exhibits the highest current density when the field is oriented in the $ab$-plane, while the BZO-doped YBCO film achieves the highest $J_c$ when the field aligns with the $c$-axis direction [109, 110].

in-field properties [105].

In the YBCO film with APCs, strain originates from mismatch affecting epitaxial growth, sharp interfaces, and strain release by crystal structure defects [17, 114]. As seen in Figure 9(a-d), when two materials with a lattice misfit meet, they can form fully coherent, semicoherent, or incoherent interfaces based on the magnitude of the mismatch and growth conditions. Thin films may deposit coherently with lattice distortions in very thin films, but as thickness increases, a critical threshold may be reached, leading to the nucleation of misfit dislocations. Complications in the misfit dislocation region, particularly in metal oxides, involve strain disrupting local chemical bonding. A coherent interface satisfies all bonding, while a semicoherent one leads to unfavorable anion-anion and/or cation-cation interactions [115]. An incoherent interface arises with disordered atomic arrangements, directly impacting current densities and critical temperatures of the produced thin films.

As previously noted, YBCO films often have a high density of natural defects, emphasizing the importance of tunability and controllability of pinning disorder [14, 72]. Moreover, the reactivity and susceptibility to oxygen out-diffusion in orthorhombic YBCO pose challenges during micro- and nano-fabrication processes, leading to a deterioration in superconducting properties. On the other hand, in the

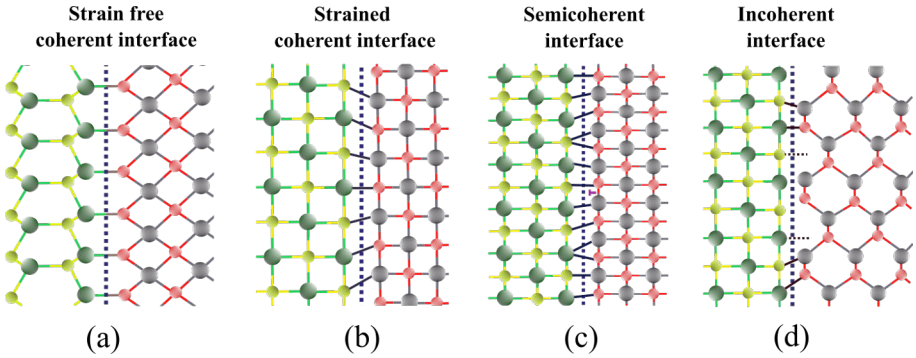


**Figure 9.** Schematic representation of interfaces (a) strain-free coherent, (b) strained coherent, (c) semicoherent, and (d) incoherent. In instances where both phases possess different lattices without a mismatch at the interface, a misfit strain-free coherent interface is observed. Depending on the magnitude of the mismatch and growth conditions, either a fully coherent or semicoherent interface can emerge, even when both phases share the same atomic arrangement. Conversely, an incoherent interface arises when both phases exhibit disordered atomic arrangements at the interface.

strain-mediated self-assembled APCs formation in the YBCO matrix, significant strain not only impacts APC growth but also compromises superconducting performance, affecting flux pinning and $J_c$ [18, 108, 116, 117]. Despite the anticipated optimal pinning efficiency with an atomically sharp APC/YBCO interface, the interface between 1D APCs and the YBCO matrix is generally strained and defective in practical situations. Thus, achieving a delicate balance between the optimal morphology of self-assembled APCs and the maximal crystalline quality of the YBCO matrix is a critical challenge in maximizing the performance of YBCO films for synergistic enhancement between $J_c(0)$ and $J_c(B)$.

# 3 Experiment

## 3.1 HTS targets and films

### 3.1.1 Preparation of different types of targets

The preparation of PLD targets with precise metal stoichiometry and the elimination of impurities are indispensable prerequisites for crafting high-quality YBCO thin films. To create advanced HTS thin film with APCs, YBCO targets infused with the secondary phase BZO were prepared. To achieve diverse APC compositions in the deposited films, BZO concentrations were systematically altered, ranging from 0 to 14 wt.%. In this thesis, two distinct types of targets were prepared: one with a micro-grain size and the other with a nano-grain size.

For the micro-grain size target, a solid-state reaction method was employed. Commercial-grade micron-sized yttrium oxide ($Y_2O_3$), barium carbonate ($BaCO_3$), cupric oxide (CuO), and yttria stabilized zirconia (YSZ) raw powders with a purity of 99.99% were carefully weighed, thoroughly mixed, and pelletized to maintain the stoichiometric ratios. The powder was heat treated at 950/920 °C for 24 hours in an air atmosphere. Subsequently, the same grinding and pelletizing process was repeated, followed by sintering at the same temperatures for an additional 24/48 hours. The final annealing step was carried out in an oxygen atmosphere at 500 °C for 24 hours to produce the micro-grain size YBCO target.

For the nanocrystalline target, a citrate-gel method, inspired by the work of [118, 119] was employed. Precursor solutions were prepared using high-purity reagents, including yttrium nitrate hexahydrate ($Y(NO_3)_3{\cdot}6H_2O$), barium nitrate ($BaNO_3)_2$, cupric nitrate hemi(pentahydrate) ($Cu(NO_3)_2$ $2.5H_2O$), and zirconyl nitrate hydrate ($Zr(NO_3)2H_2O$) dissolved separately in distilled water. Then, the mixture solution of stoichiometric quantities of Y:Ba:Cu nitrate in a 1:2:3 ratio was stirred with the magnetic stirrer, and citric acid was added. Ethylenediamine was slowly added drop by drop while constantly stirring to adjust the pH to approximately 6. The solution was then heated, and water was evaporated at 80 °C until it formed a viscous blue-colored gel. The gel was heated gradually to 450 °C for 30 minutes to obtain the precursor powder. After a gentle grinding, the precursor powder was calcinated at 725 °C for 2 hours, followed by cooling to room temperature. Finally, the calcinated powder was pressed into a pellet and sintered for 30 minutes at 900 °C, then annealed at 450 °C for 12 hours in an oxygen atmosphere to create a nano-grain size YBCO

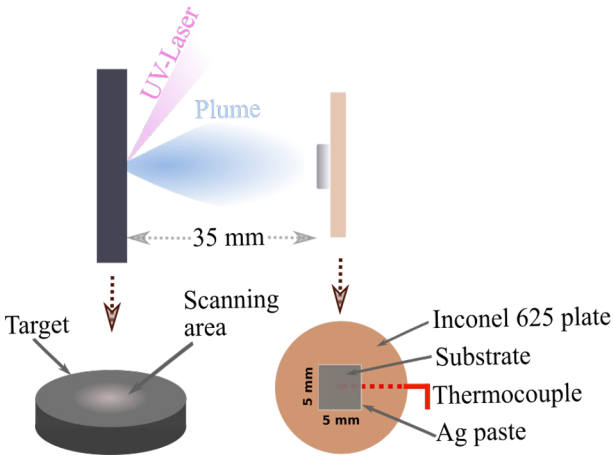


**Figure 10.** Illustration of pulsed laser deposition (PLD) process for thin film fabrication.

target. Both fabrication methods yielded targets with a diameter of approximately 2 cm and a thickness of 2.5 – 3 mm. A solid-state reaction target has a grain size of several micrometers, while in the citrate-gel targets the grain size is 50 nm or even less. To ensure the quality of the prepared targets, their phase formation and impurity content were rigorously confirmed through x-ray diffraction analysis. In this work, targets made with the solid state reaction method are referred to as $\mu$-target and with the citrate-gel method as $n$-target.

### 3.1.2 Fabrication of HTS thin films

Since its inception by Smith and Turner in 1965 [120], pulsed laser deposition (PLD) has risen to prominence as a leading method for depositing complex material films, with the groundbreaking achievement of epitaxial HTS film fabrication credited to Dijkkamp at Bell Communications Research in 1987 [121]. PLD's strength lies in its simplicity, allowing precise control through adjustments in critical parameters such as laser energy density, pulse duration, repetition rate, target-substrate distance, growth temperature, and oxygen partial pressure. Moreover, PLD's versatility extends beyond film replication, making it a valuable tool for systematically introducing defects into YBCO films. Furthermore, PLD facilitates the construction of multilayer structures by aligning different targets beneath the laser beam with unparalleled precision. Hence, in this dissertation study, PLD serves as the primary technique for producing YBCO films.

The PLD relies on the utilization of a high-energy pulsed laser, typically operating in the nanosecond range with carefully calibrated energy levels. When the laser pulse impacts the target material, a fraction of the material is vaporized, giving rise

to a plasma plume comprising atoms, ions, and molecules. This plume formation is driven by the rapid heating and vaporization of the target material, and it extends outward from the target surface. As the atoms and molecules within the plume come into contact with the substrate's surface, they undergo condensation and deposition, gradually forming a thin film [122]. By fine-tuning deposition parameters, PLD enables the attainment of specific film characteristics, such as thickness, composition, and crystalline structure, making it a versatile technique in materials science and thin-film technology. However, PLD is sensitive to parameters such as target quality, target-to-substrate distance, laser fluence, background pressure, and substrate temperature. These factors can influence the formation of various nanoscale defect structures within the superconductor, particularly under non-equilibrium conditions during film growth. Consequently, they affect the flux pinning characteristics and can notably enhance the critical current densities of HTS films. Thus, optimizing deposition parameters has a critical role in high-quality film and preliminary studies were necessary.

To optimize the deposition temperature, several systematic studies had been done in our previous research and the optimized deposition temperature of 750 °C observed in these studies was used in this work [123]. The target used in this work was made because the target grain size has a significant impact on the PLD film growth process as was seen in [109]. Using nano-grain size targets instead of micro-grain targets alters the growth mechanism on the substrate, resulting in a different distribution of naturally formed nanosized defects, including a greater number of grain boundaries that can act as vortex pinning centers within the YBCO lattice. Moreover, the result clearly shown in [124] proved the influence of the deposition distance on the growth of self-assembled BZO nanorods. The perfectly aligned and distinctly longer self-assembled BZO nanorods within the YBCO matrix were observed by the optimized deposition distance. Hence, in this dissertation study, the optimized deposition parameters determined by preliminary studies were used for producing high-quality YBCO films.

The illustration of the deposition process used in this work is shown in Figure 10. During the fabrication process, the XeCl excimer laser generates a pulsed ultraviolet (UV) beam with a wavelength of 308 nm, which is directed into a vacuum chamber through UV transparent components. The raw laser beam, with an output energy of approximately 63 mJ, is focused onto the target surface with an energy density of roughly 1.3 J/cm$^2$ using an external lens and 5 Hz repetition frequency. The target-to-substrate distance was kept at 35 mm. The substrate's temperature is maintained in the range of 750 °C, while oxygen pressure is dynamically controlled by 175 mTorr. Following deposition, the film undergoes additional oxygenation at 725 °C for 10 minutes, facilitating the formation of the YBCO crystal lattice structure and enabling control of oxygen stoichiometry.

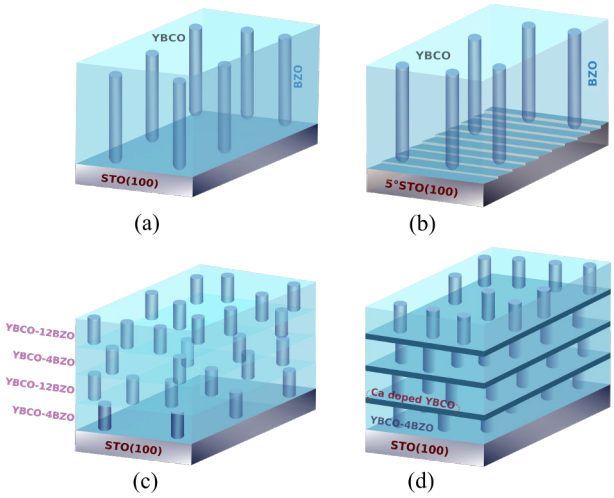


**Figure 11.** Schematic illustration of different film designs (a) BZO-doped YBCO film on STO substrate (b) BZO-doped YBCO film on 5° miscut STO substrate (c) multilayer film (d) heterostructure multilayer film.

### 3.1.3 Thin film designs for optimization of superconducting properties

To optimize the superconducting properties, aiming for higher $T_c$, as well as high $J_c(0)$ and $J_c(B)$, various film designs were used. In the first set of experiments, BZO-doped YBCO thin films, approximately 190 nm thick, were deposited on single-crystalline $SrTiO_3$ (STO) (100) substrates as well as on STO (100) substrates with a 5° miscut angle along the [010] direction, as seen in Figure 11(a-b), from [**III**]. The YBCO $\mu$-target with various BZO weight percentages (ranging from 0 to 10 wt.%) were utilized to introduce different APCs composition in the YBCO matrix.

In the second set of experiments, multilayer films on STO (100) substrate were created by 4 wt.% BZO and 12 wt.% BZO, as presented in Figure 11(c), from [**I**]. The multilayer structures consisted of alternating layers of 4BZO and 12BZO with total of 4, 8, and 20 layers (4ML, 8ML, and 20ML). Sequential deposition of each layer was achieved by changing the PLD target *in situ* [125], and the deposition was stopped for around 120 s during which the PLD target was changed. The total thickness of the films was kept constant, around 200 nm.

In the last set of experiments, the heterostructure multilayer films with incorporating heterolayers of 4 wt.% BZO-doped YBCO and 30 wt.% Ca-doped YBCO were fabricated on single-crystalline STO (100) substrates, from [**IV**]. The multilayer structures consisted of 4 and 8 layers of BZO-doped YBCO (4L and 8L), with approximately 20 nm thickness of Ca-doped YBCO deposited between them, as illustrated in Figure 11(d). The same deposition process done by the previous multi-

layer was performed with the YBCO $n$-target to get heteromultilayer film. The total thickness of BZO-doped YBCO was maintained at around 360 nm throughout the deposition.

## 3.2 Structural characterization

### 3.2.1 X-ray diffraction

X-ray diffraction (XRD) is an indispensable tool for characterizing thin films and it offers a wealth of information about the material, including their crystalline phase and lattice parameters, degree of crystallinity, preferential orientation or texture of crystalline grains, grain size, dislocation density, residual stress/strain, composition via lattice parameters, and even film thickness. When x-rays interact with a sample, they scatter off its crystal planes, leading to constructive interference determined by Bragg's law ($n\lambda = 2d_{hkl}\sin(\theta_B)$). This law connects the Bragg angle ($\theta_B$) to the crystallographic plane's Miller indices ($hkl$) and the lattice spacing ($d$), with '$n$' representing the diffraction order. This foundational equation underpins all XRD measurements. For exploring thin film structure analysis, the starting point is the $2\theta/\omega$ scan (see Figure 12(a)), where $\omega$ is half of $2\theta$ and the pattern is plotted as a function of $2\theta$. The $2\theta$ plot allows us to discern critical information about a material's characteristics. Residual stresses, substrate-induced strain, and compositional changes within a film can be revealed through an examination of peak positions, while the peak shape provides insights into grain size, compositional gradients, and strain distributions, offering a comprehensive understanding of the material's structural attributes (see Figure 12(b)). However, it is essential to recognize that a $2\theta/\omega$ scan alone cannot provide a complete epitaxial assessment and distinguish texture in all three principal axes of the film. Therefore, additional techniques such as pole figures or $\phi$-scans are typically required to assess in-plane orientation and construct a comprehensive picture of the film's orientation.

To assess in-plane orientation, a precise procedure involves sample tilting and rotation, aligning lattice planes with the Bragg plane. The sample is aligned like in a $2\theta/\omega$ scan, and then, incrementally tilted in $\psi$ and rotated in $\phi$. Diffraction of planes with a $d$-spacing corresponding to the Bragg angle results in an intensity map. Alternatively, a $\phi$-scan involves moving the diffractometer to a specific Bragg reflection, tilting the sample in $\psi$, and scanning while rotating through $\phi$ = 0 to 360 degrees (see Figure 12(d)). The number of observed maxima during a $\phi$-scan indicates a single in-plane orientation, revealing crystal symmetry and out-of-plane orientation.

Moreover, to gauge the quality of intended epitaxial growth or preferred orientation, the full width at half-maximum (FWHM) of the rocking curve is often documented. In this measurement, the Bragg angle is fixed at the centroid position

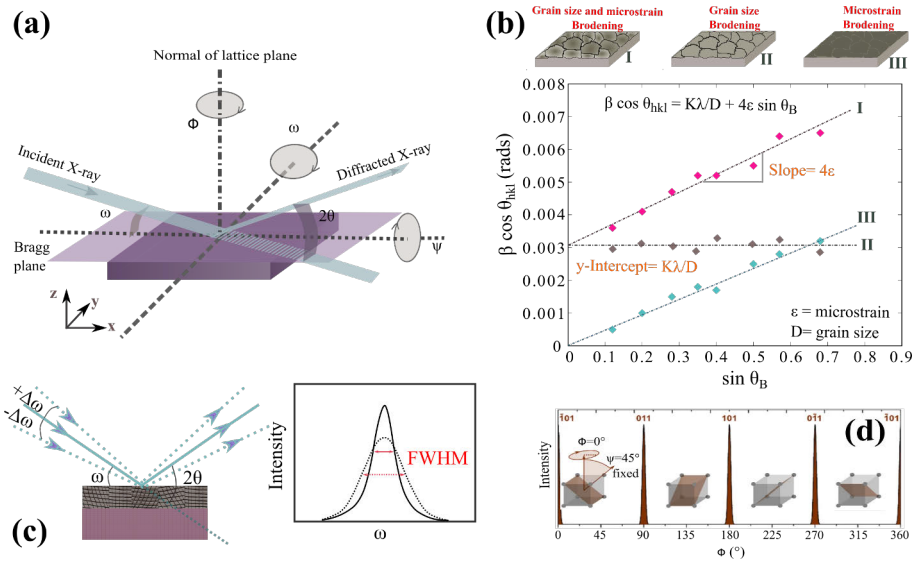


**Figure 12.** (a) Schematic of the notation used for the angles and degrees of freedom in a typical diffractometer used for thin film measurements (b) Williamson-Hall plot for a polycrystalline film where the peak broadening is dominated by either the grain-size, microstrain or a combination of the two (c) Schematic of a rocking curve measurement and (d) Schematic $\phi$-scans for a cubic (001) oriented film for the (110) reflection at a $\psi$ = 45°.

of a specific reflection from the $2\theta/\omega$ scan. The sample is then tilted, or "rocked," along the $\omega$ axis, causing planes not parallel to the sample surface to enter the Bragg plane. The result is a single bell curve, known as a rocking curve, which provides information distinct from that of the $2\theta/\omega$ scan. A highly oriented film, such as an epitaxial film or one with dominant columnar growth, typically exhibits a Gaussian-shaped curve with an FWHM ranging from a few tenths of a degree to a couple of degrees. Conversely, a more disoriented film may display a broader curve with a larger FWHM, indicating reduced alignment (see Figure 12(c)).

In this thesis, extensive measurements were conducted using the PANalytical Empyrean diffractometer, which operates with a Empyrean tube Cu LFF HR ($CuK_\alpha$ = 1.54060 Å) at 45 kV and 40 mA. The four-circle diffractometer, equipped with the $\omega$-axis for sample rotation, $\phi$-axis for in-plane rotation, $\psi$-axis for tilting, and the $2\theta$ axis for detector scanning, was employed. Thin films were analyzed with a collimated incident x-ray beam using a Bragg–Brentano HD mirror, a 1/4° divergence slit, and a 0.04 rad Soller. Purity of the films was assessed through ($\theta$-$2\theta$)-scans at 10°–120° with $\psi$ = 0. The $c$-axis lattice constants of the nanocomposite films were quantitatively determined from the YBCO (005) peak, and inhomogeneous strain ($\varepsilon$) was analyzed using Williamson-Hall (W-H) plots, as seen in Figure 12(b)). The out-of-plane misorientation spread was estimated by conducting $\omega$-scan (rocking curve)

measurements of YBCO thin films. These measurements focused on the YBCO(005) reflection at $2\theta \approx 38.5°$ and BZO(002) reflection at $2\theta \approx 43.5°$ in YBCO thin films. The in-plane texture quality was assessed through 2D($2\theta - \phi$)-scans for YBCO (102) with different $\psi$ values for $c$- and $a$-axis oriented grains, as well as for BZO (110). Similar ($2\theta - \phi$)-scans were taken for YBCO (212) to quantify twinning. To determine crystallographic orientations and to confirm the epitaxial growth of the YBCO on the substrate, extensive measurements in $2\theta$, $\psi$, and $\phi$ directions were carried out on YBCO (102) and BZO (110) peaks.

### 3.2.2 Scanning transmission electron microscopy (STEM)

TEM is a technique in which a thinned sample is irradiated with a highly coherent electron beam instead of light. The transmitted and scattered electrons are imaged, and the sample structure can thereby be observed at a high magnification [126]. When electrons hit the thin specimen, some travel straight through it, while others are subject to scattering by the atomic lattice. The scattering can broadly be either elastic or inelastic. By selecting the electrons according to their scattering nature, we can gain knowledge of the morphology, crystal structure, composition, and electronic states inside the sample. The electron gun generates a collimated and hairline electron beam with defined kinetic energy, serving as the source for TEM. The primary electron beam is focused or defocused into a constant focal distance by a series of condenser lenses as required, and several apertures are also used to collimate the beam. The focused electron beam then travels through the specimen, producing either an image or a diffraction pattern. Subsequently, the transmitted beam then traverses a series of lenses and ultimately reaches a fluorescent screen and the final TEM image is obtained. The schematic diagram of TEM system is illustrated in Figure 13. To minimize unwanted electron scattering during its journey and prevent sample contamination, TEM conducts all its procedures within a high-vacuum environment.

The optimal method for visualizing YBCO's internal structural details, including defects and atomic arrangement, is through high-angle annular dark field (HAADF) imaging using aberration-corrected scanning transmission electron microscopy (STEM). HAADF STEM relies on high-angle scattering to create Z-contrast images, making it ideal for characterizing and identifying structural defects within a distorted Y123 matrix. The microstructure of the films as well as the defect formation was investigated with JEOL JEM 2200FS bright-field transmission electron microscopy (BF-TEM) using 200 kV operating voltage. The samples for BF-TEM were prepared by cutting a cross-sectional lamella via the focused ion beam (FIB) technique in a FEI Nova 600 Nanolab Dual Beam FIB-SEM, using the *in situ* lift out procedure with an Omniprobe extraction needle. The ImageJ software was employed for statistical nanocrystal measurements in cross-sectional regions.

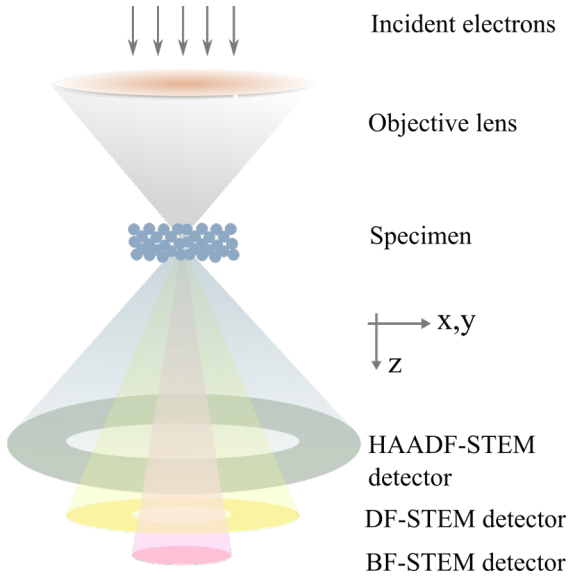


**Figure 13.** A basic STEM schematic is provided, illustrating the use of transmitted electron beams detected by various detectors, including bright-field (BF), dark-field (DF), and high-angle annular dark-field (HAADF). The DF detector, designed for optimal signal collection, can be adapted for both DF and HAADF imaging by modifying the scattering angle range.

## 3.3 Superconducting properties' characterization

### 3.3.1 Magnetic measurements

Superconducting properties of YBCO films were comprehensively examined using a Physical Property Measurement System (PPMS) with the ACMSII option. The investigations relied on a magnetometer, an accurate temperature controller, and a superconducting coil capable of generating a highly uniform magnetic field up to 8 T. This unique setup facilitated both $AC$ susceptibility measurements and $DC$ magnetic moment measurements. A set of pick-up coils is strategically positioned within the superconducting coils for precise detection. Schematic presentation of PPMS is presented in Figure 14. In all the experiments, the epitaxially grown YBCO films were oriented with their $c$-axis parallel to the external magnetic field. The critical temperature ($T_c$) and superconducting transition width ($\Delta T_c$) were determined by conducting magnetization vs. temperature measurements with a 0.1 mT $AC$ field at a frequency of 113 Hz, spanning from 100 K down to 10 K. Identified on the $M(T)$ curve, the onset critical temperature is marked by the deviation between the real and imaginary parts of the sample's magnetization, indicating the transition from normal to superconducting states. All $T_c$ values in our study correspond to the onset values. Furthermore, $\Delta T_c$ was defined as the transition width in an $M(T)$ curve, indicat-

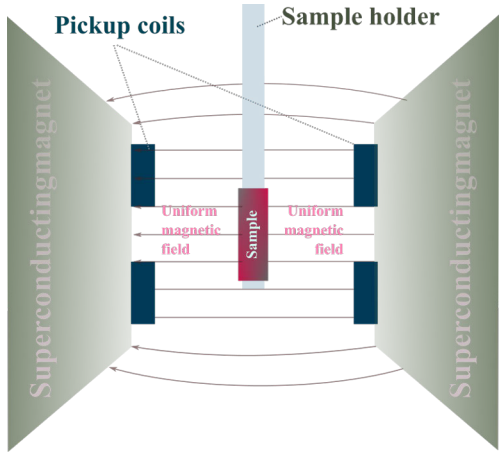


**Figure 14.** Schematic presentation of PPMS magnetometer.

ing the temperature range from normal to superconducting states, was determined by the temperature difference between zero magnetization and where magnetization decreases to 90 % of its peak value. Assessing the superconducting performance, particularly the $J_c$ of YBCO films, was further conducted through $DC$ measurements of magnetic moments performed with the PPMS. The $DC$ magnetic measurements allowed quantification of magnetization in a sample magnetized by a constant magnetic field. The magnetic moment was measured as a function of the applied field, producing a $DC$ magnetization curve $M(H)$. These $DC$ magnetization measurements were carried out as the magnetic field was varied from 8 T to -8 T and back at different temperatures, resulting in the hysteresis loops. From the hysteresis loops, the $J_c$ value of the films can be calculated by using the Bean model for square films [127] as follows

$$J_c = 2\Delta m/[a(1 - a/3b)V], \tag{6}$$

where $\Delta m$ is corresponding to the opening of the magnetization hysteresis loop, $a$ and $b$ are the width and the length of the film sample ($a \leq b$), respectively, and $V$ is the volume of the film.

### 3.3.2 Angular dependence measurements of $J_c$

In order to determine the transport properties of the material, precise measurements of the $J_c$ were conducted employing a standard four-probe technique. Prior to commencing the measurements, microbridges featuring current stripes approximately 50 $\mu$m in width were meticulously fabricated on the film through a standard photolithography process, described in Figure 15(a). This involved applying a pho-

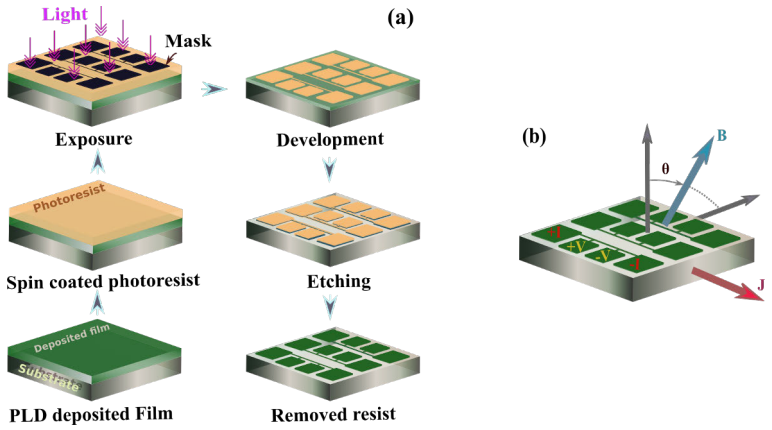


**Figure 15.** (a) Illustration of a standard photolithography process. (b) Angular dependence $J_c$ measurement system for YBCO film.

toresist to the film surfaces by spin-coating with 6000 revolutions per minute for 25 seconds. Then, subjecting them to 500 W UV exposure for a duration of 70 seconds, and then developing them for 50 seconds, followed by a 2 minutes etching step using a 0.2 M of $H_3PO_4$ solution. The remaining photoresist was removed with acetone followed by a rinse off using isopropyl alcohol (IPA) solution. Subsequently, contacts were established on the films using aluminum wire of 33 $\mu$m, bonded with a TPT HB05 Wire Bonder to prepare the electrical connections to the bridges for resistivity measurement of these films.

Critical current $I_c$ was determined using a standard 1 $\mu$V/cm criterion from measured IV curves. The $I_c$ is defined as the maximum current that can flow in a superconductor without dissipation. Critical current density $J_c$ was then calculated dividing $I_c$ by the cross-sectional area of microbridges. The measurement of the critical current density of YBCO films was performed in the presence of an applied magnetic field $B$ as a function of the angle $\theta$, as well as its dependence on temperature ($J_c$ ($\theta, H, T$)). The angle $\theta$ denotes the orientation between the applied magnetic field and sample normal, $J_c$ measurements were performed in the maximum Lorentz force configuration, (i.e., $I \perp B$). The measurement arrangement for YBCO film with the four-probe technique is illustrated in Figure 15(b). The determination of anisotropic critical current values ($J_c$ ($\theta$)) entailed a comprehensive investigation under a wide range of temperatures and magnetic fields, where $\theta$ was systematically varied from 0° to 360° in angular increments of 3°. This versatile experimental setup was made possible through the employment of a horizontal rotator option available in the PPMS.

# 4 Results and discussion

## 4.1 Optimized $J_c$ with varying APC concentration using different substrates

In YBCO films the intentional growth of defect structures provides a tailored vortex pinning landscape. For instance, the strain-mediated self-assembly of $c$-axis aligned 1D APCs in YBCO films garners significant interest, as it offers correlated pinning to magnetic vortices when the magnetic field aligns parallel to the 1D APCs, while tilted nanocolumns or mixed APC morphology further augment overall vortex pinning and angular isotropy across various field orientations [70, 99, 117, 128, 129]. Especially, there is a significant improvement in correlated pinning of 1D APCs leading to enhanced $J_c$ at B$\|$ $c$-axis when $B \leqslant B_{max}$, as mentioned earlier. This clearly shows that adjusting thin film growth for specific applications, for instance, such as increased magnetic field intensity, involves increasing the density of defects through APCs and that could be done by increasing the dopant concentration. However, elevated dopant concentrations negatively affect the growth of YBCO thin films. The resultant deterioration of the YBCO superconducting phase and the APCs/YBCO interface [11, 85, 130], induced by strain fields and chemical contamination in BZO-doped YBCO films, raises significant concerns for YBCO films incorporating self-assembling APCs.

Because of the complex nature of $J_c$, influenced by both intrinsic and extrinsic properties of HTS materials, the adverse effects of increased strain in BZO-doped YBCO films lead to degradation in not only the $T_c$ but also absolute $J_c$ [14, 18, 85, 131]. A noticeable change occurs in the growth of BZO-doped YBCO with varying BZO concentrations depicted clearly in the accompanying Figure 16(a-c). This shift becomes more pronounced as $c$-axis oriented BZO nanorods extend across the $ab$-plane when BZO content reaches 12 wt.% as corroborated by the TEM image (see Figure 16(d)). This result suggests that the maximum pinning density of $c$-axis oriented BZO nanorods might be achieved when the BZO concentration is increased up to 10 wt.%. Despite the increased pinning density observed with BZO concentrations surpassing 10 wt.%, optimal $J_c(B)$ at elevated fields is attained with 4 wt.% BZO doping, as evidenced in [**II**]. These results emphasize that although dopant concentration can regulate strain fields to manipulate the orientation and density of APCs, the detrimental impact of excessive strain in BZO-doped YBCO films

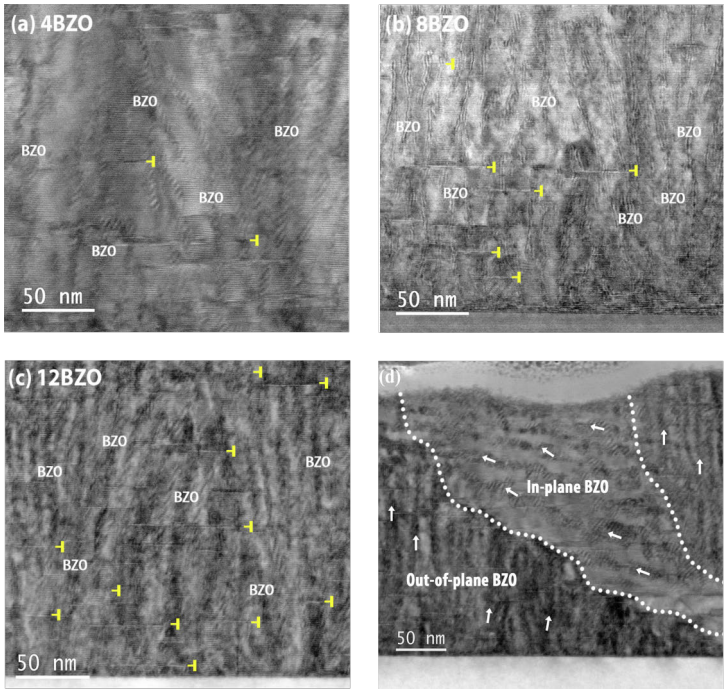


**Figure 16.** Images from cross-sectional STEM reveal (a) 4 wt.%, (b) 8 wt.% and (c) 12 wt.% BZO doped YBCO films, from [**II**], with labeled BZO columns and stacking faults highlighted by yellow vectors. (d) The STEM image of a 12 wt.% BZO-doped YBCO film, from [**II**], shows that approximately 10 % of BZO nanorods, predominantly situated at the film's top layer, are aligned parallel to the in-plane direction. The direction of BZO columns is indicated by white arrows.

manifests in decreased self-field $J_c$ and flux pinning [14, 18, 85, 131]. Alternatively, the depiction of interfacial and surface effects at the miscut substrate/film interface of YBCO films illustrates their influence on growth mechanisms. The excess strain stemming from the miscut substrate, compared to a pristine one, results in various phenomena such as lattice misfit-induced defect modifications [132, 133], anisotropic critical current density [71, 134], twin domain alterations [135], vortex channeling [136], and $c$-axis tilt changes observed in vicinally grown YBCO films [137]. The vicinal substrate surface, experiencing modulation in morphology and energy from strain induced by lattice misfit and its step-and-terrace structure [92, 138] dictated by the vicinal angle, serves as a means to precisely tune crystalline perfection and the landscape of vortex pinning. Hence, the interplay of lattice misfit strain, dopant concentration, and surface-step dimension might provide a tunable parameter to investigate defect formation and geometry, aiming to craft a controlled vortex pinning landscape, with nanocolumn formation aiding in strain accommodation and defect density reduction in the YBCO matrix. Building on this knowledge,

our study focuses on BZO-doped YBCO films with different BZO contents (0 – 10 wt.%) deposited on 5° miscut STO(100) substrate. The ensuing exploration aims to understand the modified strain's effect on self-field and in-field critical current densities, with a comparative analysis against YBCO films on commonly used pristine STO(100) substrates.

### 4.1.1 Crystalline quality and microstructure

In the BZO-doped YBCO film grown on pristine STO substrate, the lattice mismatch between YBCO and BZO significantly influences the formation of BZO nanocolumnar defects. Despite a minor role from substrate-induced strain, the large lattice mismatch of approximately 9 % at the YBCO/BZO interface triggers significant semi-coherent interface strain [18, 114, 139], influencing YBCO crystalline properties. Hence, the increase in misfit dislocations, stemming from this strain primarily found in BZO-doped YBCO films on pristine STO substrate, contributes to a decrease in the overall quality of the YBCO matrix between BZO nanorods. The elevation of BZO concentration induces amplified isotropic strain, consequently causing a notable reduction in crystalline quality and an upsurge in defect densities, as evident in Figure 16(a-d), from [**II**]. The degradation of both out-of-plane and in-plane texture in the YBCO matrix with higher BZO content, as discussed in [**II**], is clearly correlated with the increased $\Delta\omega$ and $\Delta\phi$ values observed in the XRD results. Additionally, the linear increase in the $c$-axis lattice parameter with BZO content is pronounced, as seen in Figure 17(a), from [**III**]. Moreover, there is a notable increase in stacking faults with BZO content, which also impacts the length of nanorods, as seen in Figure 16.

Analyzing the growth mechanism of the 5°STO film highlights a significant departure from that of the pristine STO film. In the 5°STO film, the miscut surface induces anisotropic crystallinity, altering substrate/film interface strain compared to well-oriented STO substrates. Furthermore, the existence of substrate steps, resulting from a vicinal off-cut (with 5° angles), has a significant impact on the migration of adsorbed particles and, consequently, on the growth mode [140]. Hence, both the semi-coherent interface strain triggered by YBCO/BZO and the film/substrate anisotropic strain play crucial roles in the behavior of the 5°STO film, contributing to its distinct characteristics. As seen in Figure 17(a), the tensile strain in $ab$-plane caused by the miscut substrate surface notably decreases the $c$-lattice parameter. The step edges of the YBCO film exhibit curvature and irregularity, leading to a more pronounced deviation from perfect alignment along the $c$-axis in the orthogonal direction of the interface region, as shown in an enlarged image in Figure 18, from [**III**]. The XRD results affirm that the fabricated films exhibit growth on the crystallographic STO(100) surface and epitaxially oriented $c$-axis growth, as depicted in the inset of Figure 17(a). Interestingly, within the studied range of BZO content, the

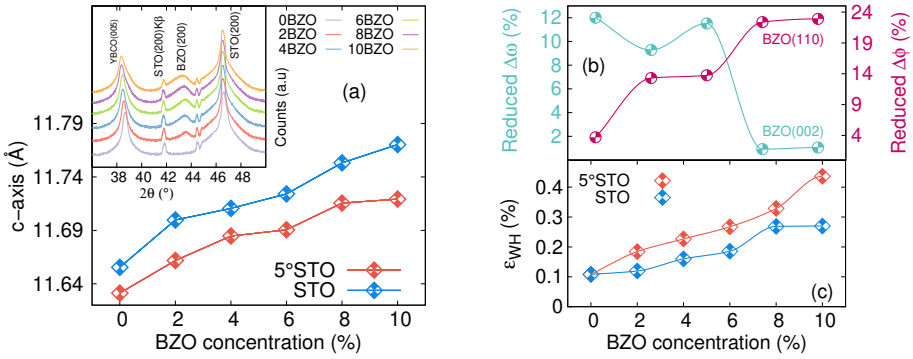


**Figure 17.** (a) The relationship between BZO dopant concentrations and the $c$ lattice parameter is depicted for both 5°STO and pristine STO films, with the inset figure displaying the x-ray diffractograms of BZO-doped YBCO films on 5°STO substrates, from [**III**]. (b) The variation of reduced peak width corresponds to the in-plane and out-of-plane directions of BZO in the 5STO film relative to pristine STO film, as analyzed through the widths of BZO(002) and BZO(110). The reduced widths are calculated using the formula: ($\Delta\omega/\Delta\phi$(5°STO) - $\Delta\omega/\Delta\phi$(STO)) / $\Delta\omega/\Delta\phi$(STO) and (c) the variation in BZO concentration corresponds to the nonuniform microstrain observed between 5°STO and pristine STO films, from [**III**].

observed $c$-axis parameter in 5°STO remains consistently smaller, while a gradual elongation of the $c$-axis is observed with increasing BZO content, as seen in Figure 17(a).

However, the microstrain observed in the 5°STO film surpasses that of the pristine STO, as illustrated in Figure 17(c). This divergence can be attributed to the distinct mechanisms of strain relaxation between miscut and pristine STO substrates. In films grown on miscut substrates, the additional strain induced by the substrate's misalignment, anisotropic crystallinity, and mismatch between film unit cells and substrate terrace width cannot be released through edge dislocations, unlike in films grown on pristine substrates. Curiously, these findings reveal a reduced relaxation of strain in the YBCO on the vicinal substrate, hindering defect formation and promoting enhanced growth of BZO nanorods in both the in-plane and out-of-plane directions. Furthermore, the combined strain stemming from the accommodated unit cells between the film and the substrate terrace might play a role in the structural evolution of BZO nanorods within the YBCO matrix. Consequently, the enhanced growth of BZO nanorods in both directions is evidenced by the narrower XRD peak widths of BZO, as depicted in Figure 17(b).

The TEM measurements also reveal that the nanorods exhibit increased length compared to those grown on pristine STO substrates, although their distribution appears slightly more random rather than the homogeneous pattern observed in pristine STO films. Most nanocolumns tilt by approximately 5° from the out-of-plane direction of YBCO (see Figure 19(a) top), while some nanorods exhibit an approximate

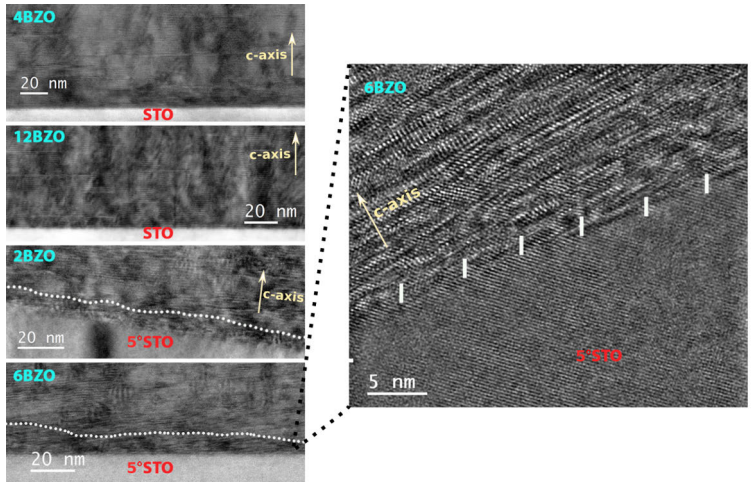


**Figure 18.** STEM images of the substrate/film interface are provided for 4BZO/STO, 12BZO/STO, 2BZO/5°STO, and 6BZO/5°STO configurations, from [**III**]. The strained region adjacent to the 5°STO substrate interface is marked by a white dotted line, while the $c$-axis direction of YBCO is indicated by a yellow arrow. Additionally, the right panel offers a magnified view of the 6BZO/5°STO substrate interface, along with corresponding terrace widths ranging from 4.92 to 5.99 nm.

tilt of ≈30° at the top of strained zones, as illustrated in Figure 19(a) bottom. Furthermore, within the 5° film, the microstructure demonstrates enhancement as the distance from the substrate increases. This enhancement stems from the growth mechanism on the miscut substrate, favoring step-flow growth of YBCO [133], thereby decreasing the probability of defect formation in contrast to the island growth often seen on pristine STO substrates. Moreover, the necessary layer thickness for microstructure relaxation notably surpasses the critical thickness of $c$-axis oriented YBCO films on pristine STO [141].

As the BZO content reaches 10 wt.%, the morphology of 5°STO sample shifts to a mixture featuring a higher number of in-plane ($c$-axis) and out-of-plane ($ab$-plane) directions, illustrated in Figure 19(b). This shift can be attributed to the reduction of strain field overlap, achieved by dispersing the 1D APCs and potentially adjusting their alignment away from the $c$-axis towards the $ab$-plane of the YBCO matrix. Consequently, numerous nanorods oriented along both the $c$-axis and $ab$-plane directions permeate through the thickness of the film. Conversely, as the BZO contents increase, the strain field overlap within pristine STO samples diminishes, prompting the development of a conspicuously flawed microstructure. This is evidenced by the notable presence of stacking faults, disrupting the continuity of BZO nanorods, as discussed previously. Furthermore, on the pristine STO(100) substrate, about 10 % of BZO nanorods are observed to align along the ab-plane in the 12 wt.% BZO sam-

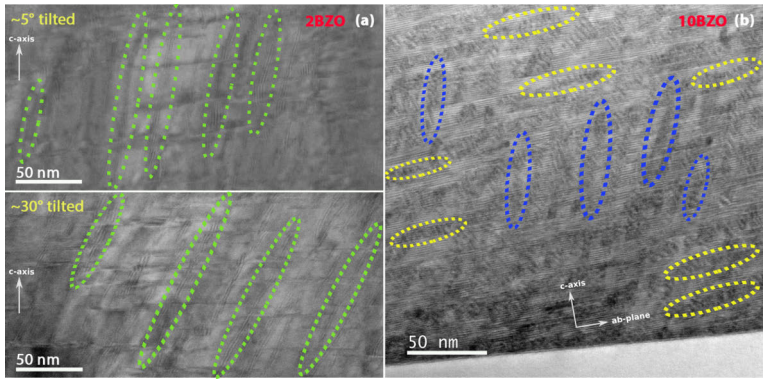


**Figure 19.** (a) Cross-sectional STEM images show differently tilted BZO nanorods in 2BZO film, with tilting angles of 5° (top) and 30° (bottom), while the white arrow indicates the $c$-axis direction of YBCO, from [**III**]. (b) In 10BZO films grown on 5°STO, from [**III**], a multitude of BZO nanorod-like defects is observed, extending across the film in both in-plane and out-of-plane directions. While white arrows indicate the $c$-axis and $ab$-plane directions of YBCO, these defects are highlighted and identified by yellow (in-plane) and blue (out-of-plane) ovals.

ple, whereas approximately 90 % of BZO nanorods align along the YBCO $c$-axis, as depicted in Figure 16(d). Upon inspection of the TEM images of pristine STO samples containing 4 wt.% and 8 wt.% BZO, it is apparent that their microstructures are largely alike, with the primary distinction lying in nanorod and stacking fault densities. Despite variations in BZO contents in all deposited films, there is no clear variation in nanorod diameter (5.4–5.9 nm). However, the average diameter of BZO nanorods on a 5°STO substrate has slightly increased from 6 to 6.9 nm. Thus, the structural and microstructural analyses provide clear evidence of reduced strain relaxation in YBCO, effectively curbing defect formation and promoting the growth of BZO nanorods in both in-plane and out-of-plane orientations, thereby maintaining a coherent interface between the two materials.

### 4.1.2 Strain-affected superconducting properties

Even though the BZO-doped YBCO films experience significant strain on the pristine STO substrate, which leads to degradation in superconducting performance [70, 86, 131, 142], the modified strain on a miscut substrate has proven advantageous. This modified strain may alter the strain field distribution and improve the overall pinning landscape, leading to enhanced $T_c$ and $J_c$. Clearly, the $T_c$ observed in 5°STO is higher, as seen in Figure 20(a), from [**III**], particularly noticeable at higher BZO concentrations, leading to an approximately 5 K increase in $T_c$ at 10 wt.% BZO compared to pristine STO films. When examining the dependence of $T_c$ on BZO content, it is apparent that the decrease in $T_c$ is more pronounced in the pristine STO samples,

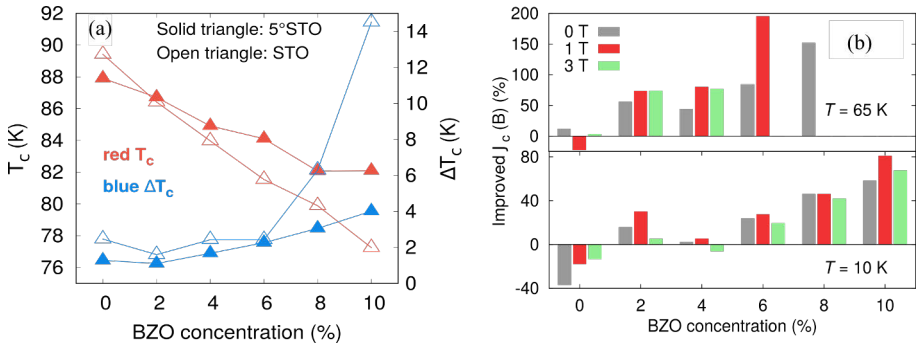


**Figure 20.** (a) The critical temperature $T_c$ and transition width $\Delta T_c$ vary with the dopant concentration, from [**III**] and (b) enhancements in $J_c$ are observed in 5°STO samples at temperatures of 10 and 65 K across varying magnetic fields of 0, 1, and 3 T, relative to the values of BZO-doped YBCO films on pristine STO substrates, from [**III**].

although there is a linear decline in $T_c$ with increasing BZO concentration observed in both sets of films, attributed to the expanding intrinsic strain field [143, 144]. The 5°STO films display a narrower transition width, $\Delta T_c$, which is particularly noticeable at higher BZO concentrations, indicating better overall crystalline quality compared to pristine STO samples. Consequently, the evident improvement in $J_c$ observed in 5°STO samples compared to those on pristine STO substrates is clearly illustrated across different magnetic fields and temperatures, as depicted in Figure 20(b), from [**III**]. Unlike pristine STO samples where BZO nanorods align along the $c$-axis up to 12 wt.% BZO and exhibit a high density of crystalline defects, the 5°STO sample showcases longer, splayed BZO nanorods, with slightly tilted stacking faults and nanorods aligned along the $ab$-plane, offering potential vortex pinning capabilities.

Furthermore, the accommodation field ($B^*$), contributing to the generation of a quantity of individual nanoscale defects, is distinctly noticeable in 5°STO. The $B^*$ value observed in 5°STO exceeds that in pristine STO samples across all films, and the decreasing trend in $B^*$ with BZO content in 5°STO samples is less prominent compared to pristine STO films, as seen in the inset of Figure 21(b). Conversely, the reduction in $B^*$ observed in pristine STO samples with a 10 wt.% BZO content is notably significant. Consequently, a remarkable enhancement of $J_c(B)$ of 5°STO films, reaching nearly 200 %, is achieved in the 6 wt.% BZO-doped sample at 1 T when measured at 65 K, and a noticeable 60-80 % improvement at 10 K, particularly evident in the 10BZO sample across a broad magnetic field range up to 3 T (see Figure 20(b)). While there is a clear overall rise in $J_c(0)$ observed in 5°STO films across all BZO-doped samples, with enhanced $J_c(B)$, particularly noticeable at higher BZO dopant concentrations (see Figure 21(a-b)), from [**III**], the $J_c(0)$ in 5°STO films without BZO is notably lower compared to pristine STO, as depicted in

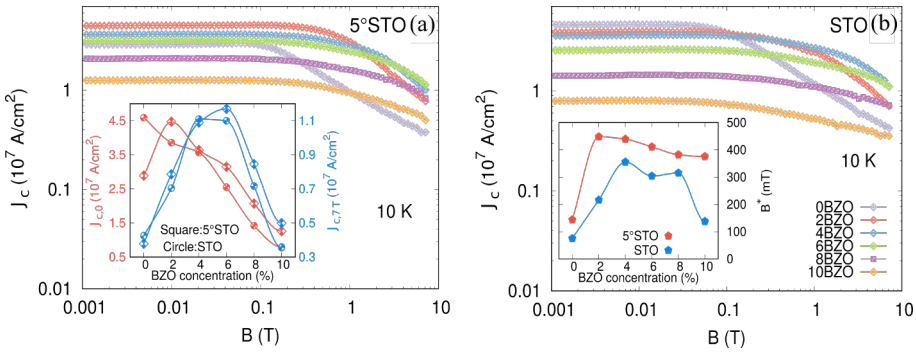


**Figure 21.** The critical current density ($J_c$) as a function of the applied magnetic field is depicted in a double-logarithmic plot for (a) 5°STO and (b) pristine STO films, from [**III**]. A comparison of the dopant concentration dependence of $J_c$(0), $J_c$(7 T) and accommodation field, B$^*$, is presented in the inset of (a) and (b).

the inset of Figure 21(a). This could be ascribed to the diminished YBCO crystalline quality, accompanied by a slight decrease in $T_c$ observed in the 0BZO sample. This outcome distinctly underscores the impact of the altered strain field due to the miscut substrate in YBCO film with BZO, whereas the substrate miscut-induced strain exerts a varied effect on the YBCO growth of 5°STO films without BZO.

Further examination of the magnetic field angle dependence with the $J_c(\theta)$ curve offers a clear illustration of pinning behavior, showcasing the influence of geometric factors within the pinning landscape. Both pristine STO and 5°STO films exhibit clear $c$-axis peaks in their $J_c(\theta)$ curves when the magnetic field aligns parallel to the $c$-axis, as demonstrated in Figure 22(a) recorded at 2 T, 10 K, from [**III**]. The observed outcome can be attributed to the strong $c$-axis pinning facilitated by BZO nanocolumnar defects in BZO-doped YBCO films. However, the presence of robust pinning nanocolumns diminishes the intrinsic pinning effect within the $ab$-plane of YBCO, resulting in the suppression of $J_c$ peaks along the $ab$-plane. Clearly, for both substrates, there is a decline in $J_c(\theta)$ along the $ab$-plane observed in both the 4BZO and 6BZO samples, along with distinct shoulders evident at 2 T. This observation might be understood by the idea of the vortex path model [145, 146], wherein the critical current at various angles correlates directly with both the strength and probability of pinning. The strongest pinning is observed at $\theta = 0°$, while partial pinning becomes more prominent as angles increase, a phenomenon mitigated by multicolumn pinning. With a higher magnetic field, repulsive vortex-vortex interactions increase, potentially stabilizing vortices outside pinning centers. This enhances pinning probability, particularly for $c$- and $ab-$directions. Weaker multicolumn pinning near $ab$-peak favors intense $c$-peak even at low fields, with $ab$-peak emerging at higher fields due to increased vortex-vortex interactions. Hence, the $J_c(\theta)$ curves re-

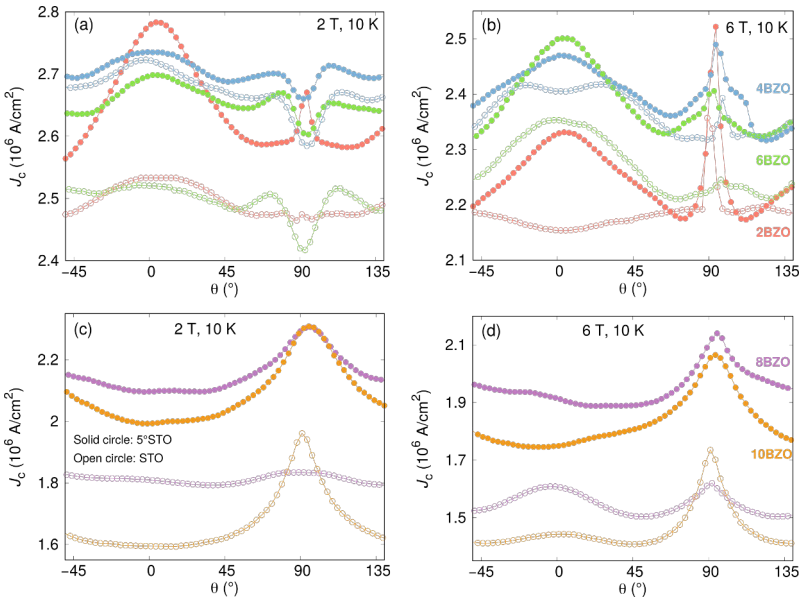


**Figure 22.** The magnetic field angle-dependent critical current anisotropies for samples with different BZO concentrations are observed at 10 K under applied fields of 2 T (a) and (c), and 6 T (b) and (d), from [**III**]. Angle $\theta$ = 90° corresponds to the YBCO $ab$-plane, while $\theta$= 0° corresponds to the YBCO $c$-axis.

veal peaks at both the $c$-axis and $ab$-plane directions when the magnetic field is raised to 6 T, although some noticeable differences are observed in the $J_c(\theta)$ between the 5°STO and pristine STO samples, as seen in Figure 22(b). Specifically, the wider $J_c$ $c$-peak in 6BZO, the double-peaked nature of $J_c$ for 4BZO, and the absence of a $J_c$ peak in 2BZO are clearly observable in pristine STO when the magnetic field aligns with the $c$-axis. Meanwhile, the $c$-axis $J_c$ peak produced by 2-6 wt.%BZO samples of 5°STO remains stronger compared to that of the pristine STO samples. Upon increasing the BZO content to 8 wt.%, a distinct broad $J_c$ peak along the $ab$-plane, without peaks along the $c$-axis, becomes pronounced in 5°STO at 2 T, as depicted in Figure 22(c). At 10 wt.% BZO, a higher $J_c$ peak along the $ab$-plane with a more concave curve in the $c$-axis direction is observed. A similar pattern is observed in the $J_c(\theta)$ curves with the increase in magnetic field to 6 T (see Figure 22(d)). Understanding the results involves the decrease in the concentration of $c$-axis aligned BZO nanorods with short segments, which arises from the formation of nanorods in the $ab$-plane direction. This change decreases the pinning efficiency in the $c$-axis direction, thereby augmenting the $J_c$ peak in the $ab$-plane direction. However, this distinction is absent in pristine STO. In pristine STO films, the $J_c$ curves demonstrate prominent $J_c$ peaks in both $c$-axis and $ab$-plane directions at 8BZO and 10 BZO under 6 T, despite the $J_c$ peak along the $c$-axis being smaller in 10BZO (see Figure

22(d)). At 2 T, the unusually flat $J_c(\theta)$ curve in 8BZO is due to strong multicolumn pinning, comparable to single-column pinning across all angles, as discussed previously. Similarly, the higher nanorod density in 10BZO suggests a substantial increase in pinning efficiency with increasing $\theta$, likely attributed to enhanced multi-column pinning and pinning probability. Consequently, $c$- and $ab$-peaks emerge in the high field range due to increased vortex-vortex interactions, while the $c$-axis peak is absent at 2 T. The result highlights the geometric effects of the pinning landscape in 5°STO and pristine STO films, which can effectively manipulate flux pinning in BZO-doped YBCO film. Although there are variations in superconducting properties, the results indicate a coherent overall increase $J_c$ in vicinal samples of BZO-doped YBCO via modified strain with miscut surfaces across the magnetic fields and temperature range under investigation.

## 4.2 Optimized $J_c$ by mutilayer architecture with varying APC densities

The critical objective for HTScc currently is not only to enhance $J_c$ but also to maximize the thickness of the superconducting layer without compromising performance. Overcoming the challenge posed by the monotonic decrease of $J_c$ with increased crystalline defects in HTS films as their thickness increases is imperative in depositing thick, high-quality YBCO films [14, 147]. Through careful engineering of interfaces and deposition techniques, multilayer films offer a flexible foundation for enhancing YBCO superconductors' performance in thicker films, making them a crucial component in advancing superconducting technologies. Multilayer films facilitate the induction of various flux pinning mechanisms and the reduction of defect densities, resulting in higher $J_c$ values, owing to their provision of tailored microstructures and additional pinning sites. Thus, significant advancements have been made in exploring various designs of multilayered YBCO films, including structures with thin oxide layers like $CeO_2$ or $SrTiO_3$ [148–150], alternating layers of APC-free YBCO and APC-added YBCO such as YBCO/BZO [108, 151, 152], YBCO/BSO [153], and APC-added YBCO with different APC structures such as YBCO/BZO with YBCO/$Y_2O_3$ [154] and YBCO/$BaCeO_3$ (BCO) [155]. These studies have demonstrated remarkable enhancements in the potential of superconducting properties for respective multilayered structures.

Typically, maximizing $J_c$ at high magnetic fields requires finding the optimal balance between $J_c(0)$ and $J_c(B)$ [16, 103]. Exclusively focusing on improving coherence length, penetration depth, and electron mean free path through advancements in crystalline perfection to impact the depairing current is just one aspect limiting progress. At higher magnetic fields, the determination of $J_c$ is largely governed by vortex pinning characteristics, encompassing pinning force and the irreversibility field [16, 42, 103]. For that, the critical aspect in establishing an ideal pinning

**Table 1.** Structural parameters such as $c$-axis lattice constant ($c$), FWHM of the $2\theta$(005) peaks ($\Delta\theta$ ), FWHM of YBCO (005)rocking curve ($\Delta\omega$), the lattice coherence length ($r_c$) determined by XRD, along with superconducting parameters such as the onset temperatures ($T_c$), the superconducting transition width ($\Delta T_c$), the exponent value from power law ($\alpha$) for the single layer and multilayer BZO doped YBCO films, from **[I]**.

| Film | c (Å) | $\Delta\theta$ (°) | $\Delta\omega$ (°) | $r_c$ (nm) | $T_c$ (K) | $\Delta T_c$ (K) | $\alpha$ |
|---|---|---|---|---|---|---|---|
| 4BZO | 11.7103 | 0.0949 | 0.2665 | 16.0282 | 84.65 | 2.86 | -0.3500 |
| 12BZO | 11.7788 | 0.2128 | 0.3872 | 11.0946 | 72.89 | 9.45 | -0.1996 |
| 4ML | 11.7214 | 0.3152 | 0.2982 | 14.3367 | 83.58 | 2.13 | -0.2288 |
| 8ML | 11.7272 | 0.3395 | 0.3533 | 12.1050 | 82.51 | 2.43 | -0.2481 |
| 20ML | 11.7356 | 0.1595 | 0.3147 | 13.5996 | 81.68 | 2.49 | -0.1989 |

landscape for various magnetic field and temperature conditions appears to involve optimizing nanorod diameter, density, and distribution [12, 92, 156–158]. Hence, research attention has turned to YBCO multilayer films integrating APCs doped YBCO, yielding noteworthy outcomes [154, 155]. Incorporating APCs enhances flux pinning properties relative to films lacking APCs, thereby improving electron mean free path effectiveness, while simultaneously compromising vortex trapping capabilities [148–150].

However, to achieve optimal performance from high-temperature superconductors (HTS) in practical applications, it is essential to maximize both self-field and in-field capabilities, aiming for the highest $J_c$ at desired temperatures and magnetic fields. The absence of nanorod density variation in previous APCs-doped YBCO film configurations has obstructed a complete understanding. Thus, in order to synchronize crystallographic enhancement with vortex pinning performance, we have developed superconducting YBCO with multilayer structures by depositing alternating layers of BZO-doped YBCO with varying thicknesses and distinct BZO nanocolumn densities. A series of multilayer films, comprising alternating 4 %BZO and 12 %BZO layers, with a total of 4, 8, and 20 layers on STO(100) substrate. denoted as 4ML, 8ML and 20ML, were fabricated. The multilayers were structurally, magnetically, and resistively characterized, and the results were compared to single-layer YBCO films doped with 4 % and 12 % BZO nanorods (4BZO and 12BZO) for analysis.

### 4.2.1 Effect of multilayering on crystalline quality

The findings obtained from XRD analysis, as shown in Table 1, from [**I**], provide a clear indication of the differences in crystalline properties between single and multilayer films. The single-layer film of 12BZO, the conspicuous elongation of the $c$-axis is evident, which can be ascribed to a substantial increase in lattice strain leading to the degradation of the YBCO structure with the wider peak width and the shorter $r_c$, whereas $r_c$ is the lattice coherence length and calculated from the width of the (005)

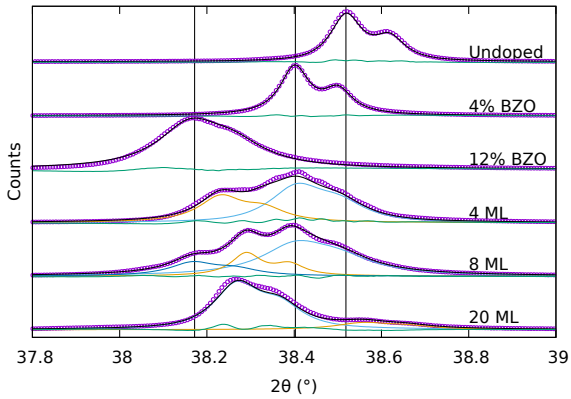


**Figure 23.** The YBCO 2$\theta$ (005) peaks exhibit variations in their evolution across undoped single-layer 4BZO and 12BZO films, as well as multilayer 4ML, 8ML, and 20ML films, from [**I**].

rocking curve by using $r_c = 1/\pi.d/l\Delta\omega$. This is further supported by the TEM results (refer to Figure 16(c)), where the shorter nanorods are observed due to the prevalence of numerous stacking faults, primarily located between two nanorods and often spanning the entire film. The 12BZO film has denser nanorod arrangement, with three times smaller inter-rod spacing than the 4BZO film, maximizing nanorod density while minimizing other defects in the YBCO matrix. As a result, the YBCO lattice in the 12BZO film shows significant $c$-elongation caused by heightened misfit-induced strain resulting from higher levels of BZO dopant, setting it apart from the 4BZO film. Clearly, fewer stacking faults, mostly located between the nanorods and near the YBCO/STO substrate interface, alongside longer nanorods observed in 4BZO, suggest superior crystalline quality and a favorable vortex pinning landscape (see Figure 16(a)).

Upon analyzing multilayer films containing 4BZO and 12BZO, the findings underscore the significant role of multilayer functionality in guiding the crystalline growth of YBCO and BZO nanorods APCs. Unlike multilayer films, continuous deposition without interruptions in single-layer films hampers effective diffusion of adatoms into positions of minimum energy, leading to the induction of dislocations and defects during film growth. This exacerbates the affiliation of new unit cells to the surface, resulting in a rapid decline in crystalline quality as film thickness increases, as reflected in increasing surface roughness. Despite the reduced strain, single-layer films are anticipated to demonstrate significantly poorer crystalline quality on average compared to multilayer films. This does not apply to the multilayer films. The multilayer films show a clear reduction in lattice elongation, particularly enhancing both in-plane and out-of-plane aspects, as seen in Table 1. In multilayer films, the improved overall crystalline quality primarily stems from reduced strain

and fewer defects in the YBCO lattice, a phenomenon explained by the theory of film critical thickness ($t_c$) [159]. During growth, epitaxial thin films conform to the template of the substrate, influencing the interface with a misfit. If the thickness exceeds a critical value, favorable misfit dislocations form due to strain energy. YBCO thin film grown on STO, YBCO exhibits a slight -1.35 % lattice misfit on $SrTiO_3$, ensuring good epitaxy. However, adding BZO induces ≈7 % ($c$-axis) and ≈8 % ($ab$-plane) lattice mismatch, intensifying interfacial effects and promoting aligned dislocation formation, particularly in single films. For instance, considering the 1.4 % lattice mismatch between STO and 4BZO, a critical thickness of 5 nm is suggested, as detailed in [**I**]. As single-layer films approach a thickness of approximately 200 nm, the reduction in critical thickness with BZO-doping coupled with increased overall thickness results in a substantial decrease in crystalline quality, driven by a growing number of defects as the film thickness rises [160, 161]. The findings underscore the effectiveness of employing a multilayer configuration within a single film. Nonetheless, precise management of layer thickness is vital to maintain equilibrium between crystalline perfection and pinning properties.

Examining multilayer films, featuring a 10 nm layer thickness in the 20ML film, fails to achieve ample lattice strain relaxation compared to the 4ML film with approximately 50 nm thickness, as validated by XRD analysis. Clearly, the (005) diffraction peaks in multilayer films consist of multiple sub-peaks, with the peak groups positioned between those of single-layer films containing 4BZO and 12BZO, as seen in Figure 23, from [**I**]. However, the ratios of 4BZO and 12BZO vary considerably depending on both the number and thickness of the layers. In the 4ML film, distinct peaks associated with 4BZO and 12BZO are clearly evident, with the predominance of the 4BZO peak suggesting adequate layer thickness for YBCO growth relaxation in the 4ML film. With an increase in number of layers, the situation becomes intricate, making it challenging to distinguish individual layers. Consequently, the 20ML film lacks clear separable YBCO layers and well-defined unit cell structures, leading to higher average strain and explaining the deteriorated crystalline properties as compared to the 4ML film. Therefore, the structural results affirm that the 4ML film demonstrates superior epitaxy and crystallinity compared to the 8ML and 20ML films.

### 4.2.2 Effect of multilayering on superconducting properties

As we expected, the structural and microstructural modifications observed in multilayer films significantly influence their superconducting properties. Remarkably, the enhanced crystalline quality evident in structural analyses results in higher $T_c$ and smaller $\Delta T_c$ in multilayer films compared to 12BZO, as seen in Figure 24(a), from [**I**]. As mentioned earlier, the deformation of the YBCO matrix structure leads to a significant drop in $T_c$ to 72.9 K and an increase in $\Delta T_c$ to 9.5 K in 12BZO (re-

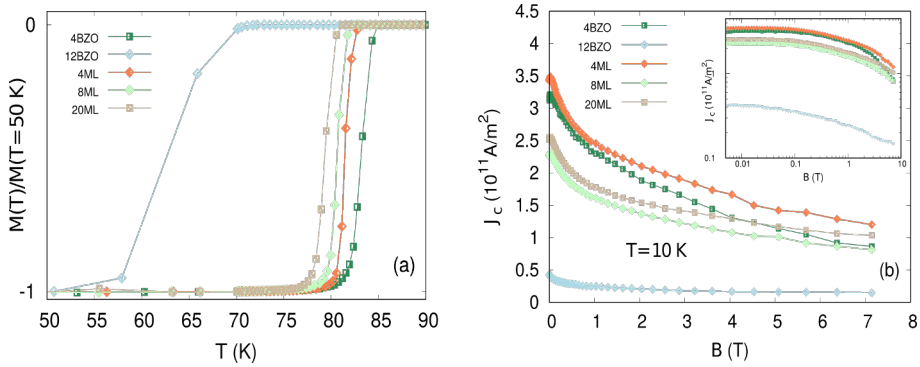


**Figure 24.** (a) Comparative analysis of temperature-dependent normalized $ac$ magnetization in single and multilayer films. (b) In the main plot, the magnetic field dependence of $J_c$ curves is shown, while the inset features their double logarithmic curves measured at 10 K for both single and multilayer films, from **[I]**.

fer to Table 1). Although multilayer films outperform 12BZO in terms of $T_c$ and $\Delta T_c$, 4BZO demonstrates the smallest $\Delta T_c$ while retaining a $T_c$ comparable to that of multilayer films.

The multilayer films exhibit higher $J_c$ compared to 12BZO, with 4ML displaying the highest $J_c$ across all applied magnetic field ranges. Because of the highly correlated pinning resulting from nanorod inclusion, the $J_c$ value in the 4BZO film exceeds that of the 8ML and 20ML films, particularly evident in low magnetic fields. Nevertheless, there is a clear cross-over between the 4BZO and 20ML films at 4 T, demonstrating the effectiveness of increased defect density in the multilayer film under high fields. The result aligns with the observed $\alpha$-values. The significant decrease in $\alpha$-values ($\alpha \approx 0.20$–$0.25$) observed in multilayer films, as opposed to those of 4BZO with 0.35, indicates strong $c$-axis pinning and weak field dependence of $J_c$. The reduced $\alpha$-value signifies less degradation of $J_c$ with the magnetic field, highlighting the significant impact of artificial pinning sites. Remarkably, the $\alpha$-value in 12BZO of 0.19 is comparably low to that in multilayer films implying that the correlated pinning centers persist prominently along the $c$-axis. However, due to the diminished pinning strength resulting from excess doping in 12BZO, the $J_c$ observed in 12BZO is the smallest. In multilayer films, with comparable $\alpha$-values and negligible discrepancies in $J_c$ behavior, it is presumed that the nature of pinning sites remains consistent across all multilayer samples. However, in multilayer films $J_c$ exhibits dependence on layer thickness. As depicted in Figure 24(b), from **[I]**, a correlation exists between decreasing layer thickness and the decrease in $J_c$, closely linked to a nearly linear decline in $T_c$. In particular, the increase in $J_c$ throughout the entire magnetic field range in 4ML is noted to be up to ten times higher than that of 12BZO, with only a marginal rise in $J_c$ ($H \parallel c$) compared to 4BZO.

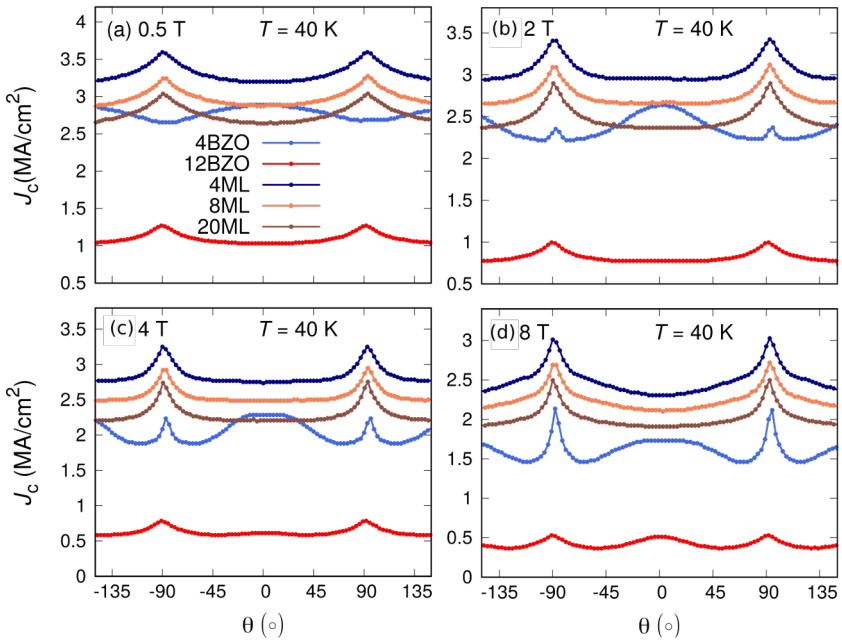


**Figure 25.** The magnetic field angle-dependent critical current anisotropies for single layer and multilayer samples measured at 40 K with different applied magnetic fields (a) 0.5 T (b) 2 T, (c) 4 T and (d) 8 T, from [**I**].

The relationship between $J_c$ and the orientation of the applied magnetic field provides additional insights into the nature of flux pinning. Examining $J_c(\theta)$ curves measured at 40 K over a wide range of magnetic fields ($B$ = 0.5, 2, 4, and 8 T) reveals varied vortex pinning behaviors arising from structural modulation, as seen in Figure 25, from [**I**]. Clearly, in multilayer films, $J_c$ peaks in $J_c(\theta)$ curves align with the $ab$-direction, with none evident in the $c$-axis across all magnetic field ranges. This observation is in line with documented cases of $c$-axis reduction in multilayer structures, as highlighted in previous research [52, 152, 162–165]. Additionally, the heightened occurrence of short, variably dense nanorod dispersions in multilayer films may preferentially enhance multicolumn pinning at higher angles. There is a marked increase in absolute $J_c(\theta)$ relative to single-layer films, even though no visible $c$-axis peak is present in any multilayer structure. This indicates that multilayering could enhance either the intrinsic superconducting properties of YBCO, the flux pinning properties across a broad angular range, or potentially both.

In contrast, the 4BZO film prominently displays a peak along the $c$-axis across the magnetic field range, alongside a peak along the $ab$-plane, notably pronounced around 2 T, and also evident in 12BZO above 2 T. The presence of longer and more continuous nanorods in the single-layer film, as observed in the microstructure, cor-

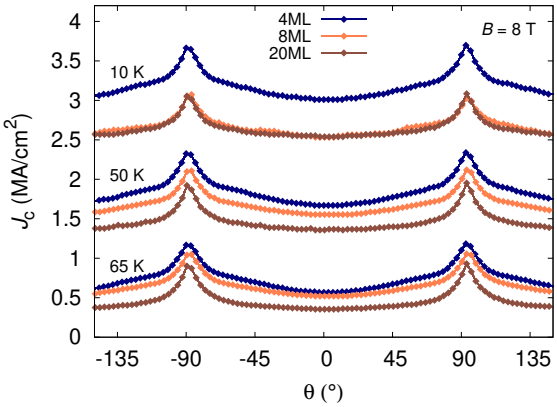


**Figure 26.** The angular dependence of $J_c$ for multilayer samples at 10 K, 50 K, and 65 K is compared under 8 T field, from [**I**].

relates with an increase in $J_c(\theta)$ at $H \parallel c$. This behavior, characterized by each vortex being securely pinned by continuous nanorods, aligns with single-vortex pinning attributes. The consistent shape of $J_c(\theta)$ curves across multilayer films confirms comparable flux pinning behavior, while the gradual decline in $J_c$ with increasing layers serves as a clear indicator of crystalline perfection, resulting in the highest $J_c$ observed in the 4ML configuration.

Interestingly, at higher temperatures, multilayer films demonstrate increased pinning center effectiveness with the number of layers. Despite 8ML and 20ML consistently displaying reduced $J_c$ values at 10 K compared to 4ML across the full angular range, the $J_c$ curve of 8ML converges towards that of 4ML at 50 K and 65 K, as depicted in Figure 26, from [**I**]. This trend suggests a moderate enhancement in pinning performance attributed to the increased number of layers and the presence of defects at elevated temperatures. Hence, multilayer films designed with alternating layers of YBCO featuring different concentrations of the same APC material show decreased structural distortion, higher defect concentration, and less degradation in $T_c$, resulting in a significant enhancement in $J_c$, especially in high applied magnetic field ranges. However, the greater improvement in superconducting properties necessitates the finer optimization of multilayers.

## 4.3 Optimized $J_c$ with heteromutilayer architecture

While there has been promising advancement in prior multilayer structures of YBCO films, opportunities remain for further improving the YBCO crystalline quality and pinning efficiency. One of the breakthrough results combining YBCO and Ca-doped YBCO films produced a multilayer system with remarkably high $J_c$, demonstrating

**Table 2.** Structural parameters such as FWHM of the 2$\theta$(005) peaks ($\Delta\theta$ ), FWHM of YBCO (102)peaks ($\Delta\phi_{102}$), $I$(005)/$I$(004), the lattice coherence length ($r_c$), FWHM of BZO (002)rocking curve ($\Delta\omega_{002}$), FWHM of BZO (110)peaks ($\Delta\phi_{110}$) for heteromultilayer of BZO doped YBCO samples 1L, 4L and 8L deposited on STO substrates, from **[IV]**.

| Film | $\Delta\theta_{005}(^\circ)$ | $\Delta\phi_{102}(^\circ)$ | $I$(005)/$I$(004) | $r_c$(nm) | $\Delta\omega_{002}(^\circ)$ | $\Delta\phi_{110}(^\circ)$ |
|---|---|---|---|---|---|---|
| 1L | 0.16 | 1.91 | 16.6 | 9.2 | 3.01 | 5.10 |
| 4L | 0.16 | 1.94 | 14.3 | 9.5 | 2.85 | 4.97 |
| 8L | 0.15 | 1.89 | 12.9 | 12.1 | 2.72 | 4.81 |

how Ca doping repairs large-angle grain boundaries in YBCO films. These findings significantly impact the large-scale fabrication of HTScc, propelling the development of techniques like IBAD and RABiTS to enhance $J_c$ through optimal grain alignment [166, 167]. Moreover, recent research demonstrates that incorporating Ca-doped YBCO space layers between BZO/YBCO layers in BZO/YBCO nanocomposites repairs defective interfaces, boosting pinning performance and superconducting properties. Ca diffusion into YBCO enlarges the $c$-axis through partial Cu replacement, mitigating lattice mismatch and preventing interface defects, resulting in highly coherent BZO/YBCO interfaces and improved $J_c$ and $F_p$ [168]. However, as per existing literature, the partial substitution of $Ca^{2+}$ ions at $Y^{3+}$ sites in YBCO brings about alterations in carrier concentration, influencing the transfer of charges from CuO chains to conducting $CuO_2$ planes [169, 170]. Hence, the fixed charge is completely counteracted by oxygen defects, resulting in a slightly reduced equilibrium oxygen content and contributing to a lower superconducting transition temperature [171]. Interestingly, the research also shows that the various aliovalent atomic substitutions in YBCO have been acknowledged for their capacity to enhance the oxygen diffusion rate by up to a factor of 100 [169, 170]. This process may, in turn, modify the distorted YBCO matrix through the inclusion of APC nanorods, bringing it closer to the optimal YBCO state, akin to the role of Ca doping in repairing large-angle grain boundaries in YBCO films [166, 167].

On the other hand, Ca-doped YBCO demonstrates average in-plane and out-of-plane lattice parameters ($a$ = 3.83 Å, $b$ = 3.88 Å, and $c$ = 11.71 Å), as analyzed by XRD, closely resembling those of BZO-doped YBCO. This alignment is notably closer than what's observed in undoped YBCO, suggesting a potential effect on the interface of these two materials for epitaxial purposes. Hence, the utilization of a multilayer design with BZO-doped YBCO and Ca-doped YBCO should allow precise control over factors such as strain relaxation and defect formation, facilitating increased film thickness while maintaining enhanced crystalline properties. To substantiate this hypothesis, our study explores multilayer films composed of heterolayers comprising 4 wt.% BZO doped YBCO and 30 wt.% Ca-doped YBCO deposited

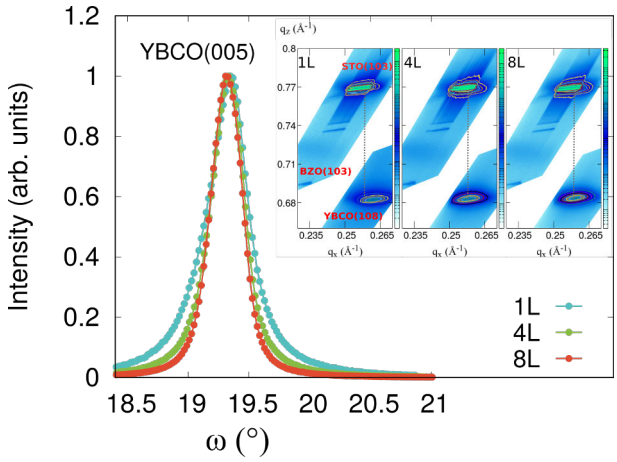


**Figure 27.** The normalized XRD rocking curves ($\omega$-scans) of the YBCO(005) peaks (the main panel) and the insets show the reciprocal space mapping (rsm) of the films, from [**IV**].

on STO(100) substrates. The heteromultilayer structures, denoted as 4L and 8L, consist of 4 and 8 layers of BZO-doped YBCO, respectively, with Ca-doped YBCO layers deposited between them. For comparison, a single-layer of BZO-doped YBCO (1L) is also prepared. A comprehensive analysis of the structural, magnetic, and resistive properties is conducted to compare and discuss the characteristics of these heteromultilayer structures in relation to single-layer films of BZO-doped YBCO.

### 4.3.1 Improved crystallographic properties in heteromultilayer films

Like the previous multilayer film, heteromultilayer films demonstrate improved crystallinity upon analysis using XRD and TEM. The narrower measured peak width presented in Table 2, from [**IV**], correlated with out-of-plane and in-plane quality clearly indicates a significant improvement in texture quality of 4L and 8L films compared to the 1L counterpart. As seen in Figure 27, from [**IV**], the enhanced out-of-plane crystallographic quality with decreased width of $\Delta\omega$ leading to a longer lattice coherence length ($r_c$) (see Table 2). The reciprocal space map, depicted in the inset of Figure 27, unveils highly epitaxial growth among the YBCO matrix, BZO dopant, and STO substrate in 4L and 8L films, with minimal disorder evident in both $ab$-planes and the $c$-axis, signifying highly epitaxial growth.

However, the rsm image of the 1L film presents a distinct view, revealing a shifted $q_x$ component suggestive of partial relaxation. Further examination of the microstructure via STEM studies, as depicted in Figure 28(a-c), from [**IV**], highlights notable differences between multilayer and single-layer films. A thorough examina-

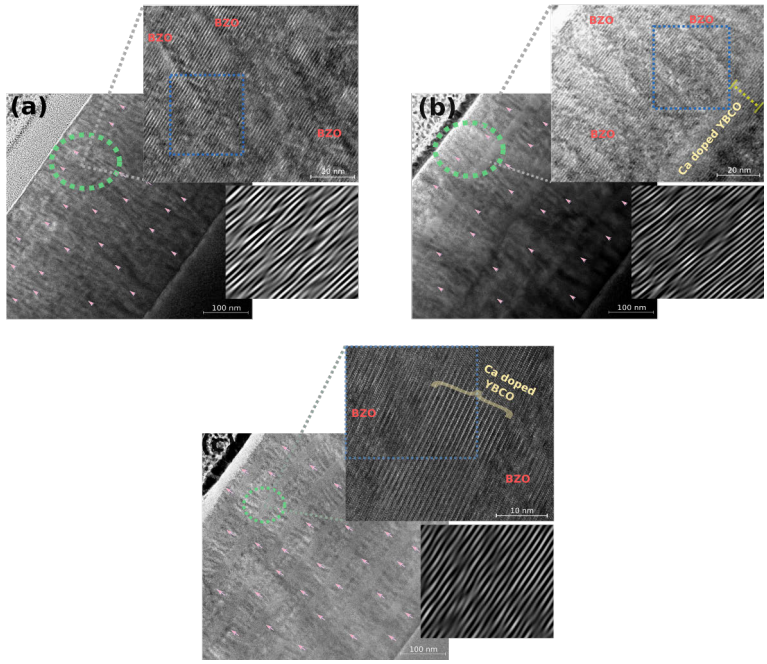


**Figure 28.** Cross-sectional STEM images depict (a) 1L, (b) 4L, and (c) 8L heteromultilayer films, highlighting BZO nanocolumns with pink arrows. Enlarged images from the green circle are displayed in the top right corner of each figure, while inverted fast Fourier transform (IFFT) images from the blue square region are presented in the bottom figures, from [**IV**].

tion of the enlarged images, depicted in the inset of Figure 28(a-c) top, showcases the dispersion of the BZO secondary phase within the YBCO matrix, revealing consistent lattice disorder and defects such as stacking faults and dislocations throughout the films. However, noticeable deterioration of crystallinity and an increased occurrence of structural defects are observed in the 1L film, supported by an inversed fast Fourier transform (IFFT) image shown in Figure 28(a-c), bottom. Remarkably, multilayered films demonstrate, on average, reduced lattice distortion and subsequently lower defect density compared to the 1L film. The results unequivocally demonstrate that the heteromultilayer structure affords precise control over critical factors such as strain relaxation and defect formation. This control mechanism facilitates the attainment of increased film thickness while concurrently preserving enhanced crystalline properties [46, 172, 173]. As seen in Figure 29(a), from [**IV**], enhanced alignment between BZO-doped YBCO and Ca-doped YBCO is anticipated to significantly reduce strain from the underlying layer during multilayer film growth. As anticipated, smooth and epitaxial growth of BZO-doped YBCO directly above the Ca-doped YBCO layer is clearly evident, with no distorted layers observable at the interface, as depicted in Figure 29(b) bottom. This is in contrast to the multilayer

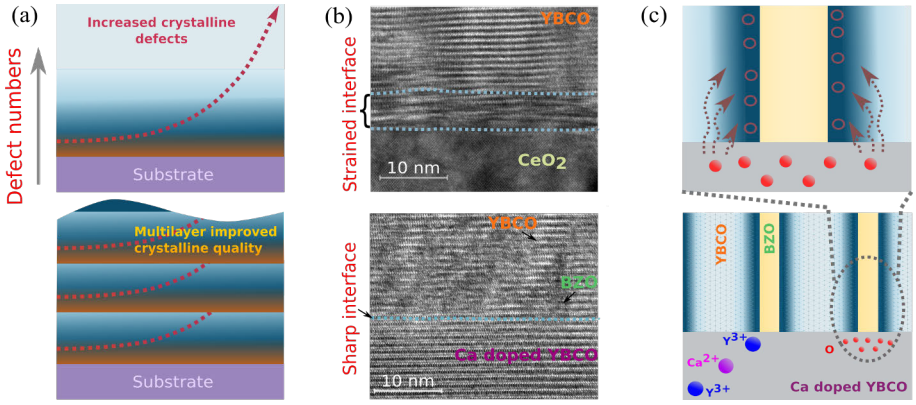


**Figure 29.** A schematic depicts mechanisms aimed at reducing dislocations and YBCO lattice distortions while enhancing crystalline quality, (a) illustrates the impact of heteromultilayer, highlighting the crucial roles of strain relaxation, a growing number of lattice distortions, and critical thickness, and the strained region at the substrate/film interface is indicated by the appearance of an orange color, (b) demonstrates the contrasting effects between the Ca-doped YBCO layer and the $CeO_2$ layer interface, considering the influence of lattice mismatch and epitaxial growth at the layer interface, and (c) the strain-induced oxygen vacancies formed around the BZO nanorods are compensated for by the diffusion of mobile oxygen atoms from the equilibrium state in the Ca-doped YBCO layer, from [**IV**].

YBCO film incorporating a $CeO_2$ interlayer or implementing sequential vacuum treatments during film growth interruptions [172, 173]. A strain region of approximately 5 nm both above and below the thin $CeO_2$ interlayer, as seen in Figure 29(b) top, has proven highly effective not only in enhancing the crystalline quality of each sublayer but also in reducing the likelihood of defect formation [172]. The results indicate the significant role of employing a heterolayer compared to using a $CeO_2$ interlayer. Additionally, the decreased oxygen deficiency ($\delta$), estimated from the intensity ratio of (005) and (004) reflections from XRD results (see Table 2), confirms the increased oxygen concentration in multilayer films [174]. This result contrasts with the previous observation that partial substitution of $Ca^{2+}$ ions at $Y^{3+}$, resulting in a slight reduction in equilibrium oxygen content due to the charge balance [18, 175]. Despite these influences, the augmented oxygen concentration in multilayer films can be linked to the potential accelerated oxygen diffusion rates via varied aliovalent atomic substitutions in YBCO. This suggests that thermodynamically driven mobile oxygen can efficiently migrate into vacant sites, particularly within the strain-induced distorted BZO/YBCO interface. Consequently, this process triggers adjustments in the distorted interface, bringing it closer to the optimal YBCO state, as demonstrated in Figure 29(c). Hence, the multilayer film shows improved crystallinity and potentially enhanced coherence at the YBCO/BZO interface by the heterolayer fashion, and the noteworthy advancement in both in-plane and out-of-

plane crystallography is particularly evident in the 8L film, showcasing exceptional enhancements.

### 4.3.2 Improved superconducting properties in heteromultilayer films

Despite the effective enhancement of grain boundary coupling and subsequent reduction in transition temperature achieved through Ca-doping [169–171], the primary contributor to the enhanced performance of Ca-doped multilayered films lies in the observed oxygen migration and improvement of crystal structure. The uniformity in $T_c$ of ≈89 K in all deposited films clearly shows the influence of Ca-doped YBCO in the heterolayer architecture not significantly affecting transition temperatures, as seen in the inset figure of Figure 30(d), from [**IV**]. Moreover, the reduced $\Delta T_c$ values of 2.6 K and 2.1 K, for 4L and 8L respectively, compared to the 1L film with 3.4 K, showcase the strong impact of the heterolayer architecture processing conditions on the crystalline quality.

Notably, the 4L and 8L films consistently demonstrate higher $J_c$ compared to 1L counterparts across various magnetic fields and temperature ranges, as depicted in Figure 30(a-c), from [**IV**]. However, the variation in the $J_c$ curve, along with the subsequent slight decrease in $J_c$ with magnetic field observed in heteromultilayer films, suggests a noticeable reduction in correlated pinning, compared to 1L film. This phenomenon can be attributed to the influence of segmented nanorods and enhanced crystalline perfection within the multilayered structure. Consequently, the $B^*$ values at 10 K noted in 4L and 8L films, standing at 105 mT and 103 mT, distinctly fall below the 1L counterpart, boasting a higher $B^*$ of 367 mT. This discrepancy can be attributed to the abundance of pinning sites resulting from the poorer structural quality of the 1L film. Furthermore, the slightly elevated $\alpha$-values detected in the 4L and 8L films with 0.22 and 0.23 respectively, compared to 0.19 for 1L are effectively linked to reduced pinning of the segmented nanorod caused by reducing layer thickness [108, 176]. As a result, the 1L film demonstrates robust $c$-axis pinning, characterized by a weak field dependence of $J_c$, attributable to the highly correlated pinning facilitated by the presence of elongated nanorods.

Nonetheless, the heteromultilayer films exhibit a significant improvement in $J_c$ across a range of magnetic fields, with particularly noticeable enhancements observed in the percentage of $J_c$ at different magnetic field strengths (0, 1, 2, and 3 T), as depicted in Figure 30(d). These results also highlight the temperature sensitivity of the pinning, underscoring its reliance on temperature in magnetic fields surpassing the matching field ($B_\phi$). As seen in Figure 30(d), the 8L film demonstrates a remarkable exponential rise in high-field $J_c$ compared to the conventional 1L film, boasting an impressive over 250 % improvement at 65 K. However, the enhancement in $J_c(0)$ diminishes with increasing temperature. The seemingly temperature-dependent vor-

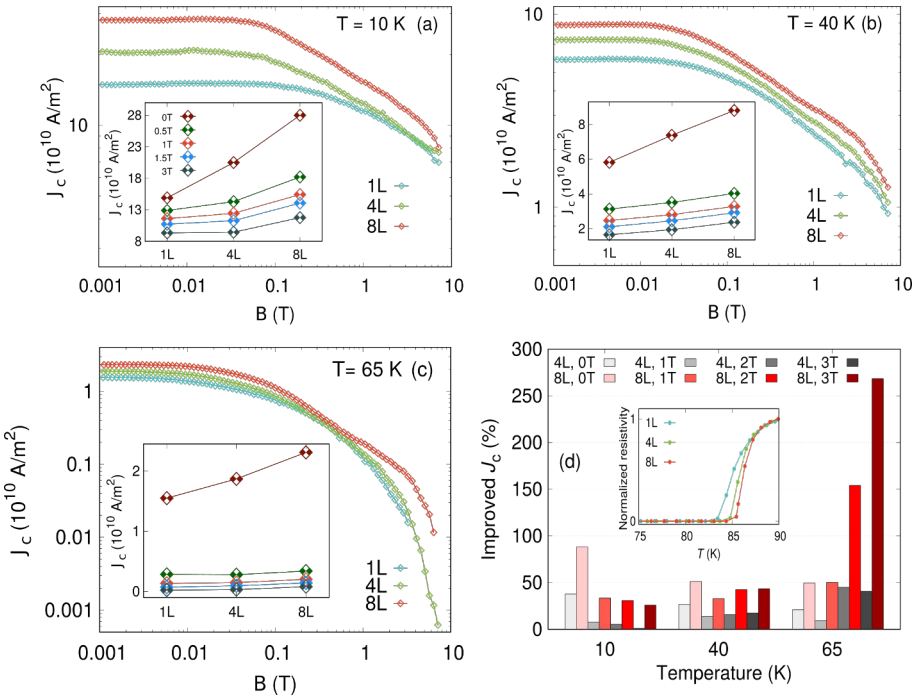


**Figure 30.** The critical current density ($J_c$) as a function of the applied magnetic field is depicted in double-logarithmic plots measured at (a) 10 K (b) 40 K and (c) 65 K for 1L, 4L and 8L films. The thickness dependent $J_c$ behaviour measured at different magnetic fields ($B$ = 0, 0.5, 1, 1.5 and 3 T) for multilayer films are presented in the insets of respective figures. (d) The enhanced $J_c$ in heteromultilayer films at various temperatures compared to the $J_c$ values of single-layer films. In the inset, a graph shows normalized resistivity versus temperature, from [**IV**].

tex pinning mechanisms suggest a connection to the superior high-field $J_c$ observed in the 8L film. At high temperatures, the likelihood of a more coherent BZO/YBCO interface is expected to bolster resistance against thermal depinning of vortices and enhance $J_c$, which is limited by vortex dynamics, as discussed earlier.

The thorough examination of the shape and anisotropy of $J_c$ with respect to angle ($\theta$) offers compelling evidence for the existence of a network comprising continuous nanorod-type dopants. As seen in Figure 31(a–b), from [**IV**], the prominent peaks along the $c$-axis in the $J_c(\theta)$ curve highlight strong nanocolumnar pinning. At 40 K and under an 8 T field (see Figure 31(a)), the narrow and intense $c$-axis peak in the 1L film is explained by nanorod alignment, as observed with numerous edge dislocations around the BZO nanorod, accommodating increased amounts of vortices at high fields [87, 177]. However, due to enhanced pinning parallel to the $ab$-plane by multilayer structure or the presence of shortened and tilted nanocolumns, multilayered films exhibit a sharper $J_c$ peak along the $ab$-plane, coupled with the broadening of the $c$-axis peak and its double-peak structure [178]. The observed variation in

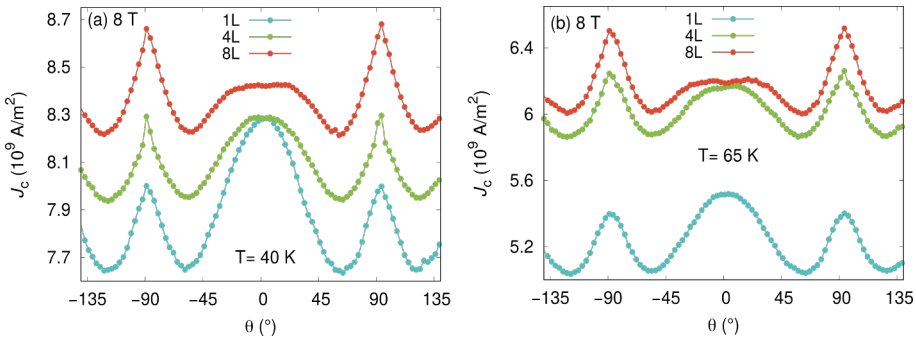


**Figure 31.** The magnetic field angle-dependent critical current anisotropies for 1L, 4L and 8L samples measured in 8 T field at different temperatures (a) 40 K and (b) 65 K. The angles $\theta$= -90° and 90° correspond to the $ab$-plane and $\theta$= 0° the YBCO $c$-axis, from [**IV**].

$J_c(\theta)$ in the heteromultilayer film aligns with previous research findings on multilayer structures, as documented earlier in [152, 155, 162–164, 179]. Furthermore, 4L and 8L films display notably higher absolute $J_c$ at 65 K compared to the 1L film, as illustrated in Figure 31(b), indicating the significantly enhanced pinning performance of multilayer films at elevated temperatures. The thickness-dependent nature of $J_c$ is also observed in $J_c(\theta)$ curves of the heteromultilayer film. As depicted in Figure 31(a–b), the 8L film exhibits a systematic decrease in the intensity of $c$-axis peaks alongside heightened sharpness and strength of $ab$-peaks compared to the 4L film, despite the 8L film showing higher $J_c$ across the entire angular range. The higher $J_c$ in the 8L film clearly suggests a greater number of effective pinning centers, despite no discernible difference in the shape of $J_c(\theta)$ compared to the 4L film. These findings underscore the intricate structural response of heteromultilayer films under high magnetic fields and temperatures. Hence, in the heteromultilayer films, enhancing YBCO crystallinity and interface quality is achieved by balancing interface-induced strain, mitigating other crystalline defects, and optimizing oxygen content in a heterolayer manner, resulting in significant enhancements in both $J_c(0)$ and $J_c(B)$.

# 5 Conclusions

This study focuses on maximizing the potential of YBCO for diverse practical uses by prioritizing the optimization of its critical current density ($J_c(0)$ and $J_c(B)$). Through extensive experiments on various YBCO thin film architectures integrated with BZO APCs, we thoroughly investigated their structural and superconducting characteristics. Our analysis and results indicate that manipulating the BZO concentration within the YBCO matrix can optimize nanorod density and improve flux pinning efficiency in high-field applications. We found that while flux pinning increases with nanorod density, a critical maximum BZO concentration of around 10 % exists. Beyond this threshold, the growth mechanism shifts, causing $c$-axis oriented BZO nanorods to grow along the $ab$-plane, significantly reducing effective pinning force. These insights into the critical threshold of BZO concentration and its impact on flux pinning mechanisms offer valuable guidance for future research in this field.

Substituting vicinally miscut STO substrates for STO leads to significant improvements in vortex pinning and critical current density within YBCO films. Our observations highlight the combined effects of step-edge strain and modified lattice-mismatch-induced BZO nanorod growth, which contributes to the creation of an optimized pinning landscape. Consequently, the slightly larger diameters, increased lengths, and more extensive penetration of nanorods through the YBCO film, coupled with their more random distribution and significant splaying, all contribute to enhanced flux pinning. These findings result in observed enhancements in $J_c$ within vicinally miscut STO substrate films. This study advances our understanding of the modified strain growth mechanism and flux pinning mechanisms in YBCO epitaxial films.

Additionally, the multilayer structured film, composed of alternating layers of BZO-doped YBCO with varying nanorod densities, showcases a synergy of improved intrinsic superconductivity and enhanced flux pinning, essential for fine-tuning critical current densities and leading to a notable increase in $J_c$, particularly evident in high-temperature and high-field ranges. Furthermore, multilayer films of BZO-added YBCO/Ca-doped YBCO with a heterolayer structure enhance crystalline quality and self-field critical current properties. This enhancement, seen in reduced lattice distortion, improved intrinsic superconducting properties, and superior growth of BZO nanorods, leads to enhanced $J_c(0)$ without affecting flux pinning. Consequently, a remarkable enhancement in $J_c$, especially at higher temperatures is

achieved compared to single-layer films.

Hence, multilayer structures demonstrate significant enhancements in both $J_{\mathrm{c}}(0)$ and $J_{\mathrm{c}}(B)$, offering promising prospects for diverse power applications. Strategic layer configuration with optimized electron mean free paths and higher BZO concentrations maximizes critical current density across varying magnetic fields and temperatures. The observed outcomes highlight the profound impact of layer thickness and dopant nanorod density on intrinsic superconducting properties and flux pinning. Adjusting these parameters significantly improves vortex pinning structure, crucial for achieving optimal critical current densities in diverse conditions.

In summary, our findings underscore the crucial role of BZO concentration, substrate choice, and multilayer structures in optimizing critical current density and flux pinning efficiency of YBCO films, paving the way for the further advancements in the design and fabrication of high-performance superconducting materials for various applications.

# List of References


[1] M. Paidpilli and V. Selvamanickam. Development of RE-Ba-Cu-O superconductors in the $u.s.$ for ultra-high field magnets. *Supercond. Sci. Technol.*, 35:043001, 2022.

[2] M. K. Wu, J. R. Ashburn, C. J. Torng, P. H. Hor, R. L. Meng, L. Gao, Z. J. Huang, Y. Q. Wang, and C. W. Chu. Superconductivity at 93K in a new mixed-phase Y-Ba-Cu-O compound system at ambient pressure. *Phys. Rev. Lett.*, 58:908, 1987.

[3] A. Goyal, D. P. Norton, J. D. Budai, M. Paranthaman, E. D. Specht, and D. M. Kroeger. High critical current density superconducting tapes by epitaxial deposition of $YBa_2Cu_3O_x$ thick films on biaxially textured metals. *Appl. Phys. Lett.*, 69:1795, 1996.

[4] Y. Iijima, N. Tanabe, Y. Ikeno, and O. Kohno. Biaxially aligned $YBa_2Cu_3O_{7-x}$ thin film tapes. *Physica C*, 185-189:1959, 1991.

[5] X. D. Wu, S. R. Foltyn, P. Arenct, J. Townsend, C. Adams I. H. Campbell, P. Tiwari, Y. Coulter, and D. E. Peterson. High current $YBa_2Cu_3O_{7-\delta}$ thick films on flexible nickel substrates with textured buffer layers. *Appl. Phys. Lett.*, 65:1961, 1994.

[6] K. Matsumoto and P. Mele. Artificial pinning center technology to enhance vortex pinning in YBCO coated conductors. *Supercond. Sci. Technol.*, 23:014001:1–12, 2010.

[7] K. Matsumoto, T. Horide, K. Osamura, M. Mukaida, Y. Yoshida, A. Ichinose, and S. Horii. Enhancement of critical current density of YBCO films by introduction of artificial pinning centers due to the distributed nano-scaled $Y_2O_3$ islands on substrates. *Physica C*, 412-414:1267, 2004.

[8] T. Aytug, M. Paranthaman, A. A. Gapud, S. Kang, H. M. Christen, K. J. Leonard, P. M. Martin, J. R. Thompson, D. K. Christen, R. Meng, I. Rusakova, C. W. Chu, and T. H. Johansen. Enhancement of flux pinning and critical currents in YBCO films by nanoscale iridium pretreatment of substrate surfaces. *J. Appl. Phys.*, 98:114309, 2005.

[9] J. L. MacManus-Driscoll, S. R. Foltyn, Q. X. Jia, H. Wang, A. Serquis, L. Civale, B. Maiorov, M. E. Hawley, M. P. Maley, and D. E. Peterson. Strongly enhanced current densities in superconducting coated conductors of $YBa_2Cu_3O_{7-x}$ + $BaZrO_3$. *Nat. Mater.*, 3:439, 2004.

[10] S. Kang, A. Goyal, J. Li, A. A. Gapud, P. M. Martin, L. Heatherly, J. R. Thompson, D. K. Christen, F. A. List, M. Paranthaman, and D. F. Lee. High performance high-$T_c$ superconducting wires. *Science*, 311:1911–1914, 2006.

[11] A. Goyal, S. Kang, K. J. Leonard, P. M. Martin, A. A. Gapud, M. Varela, M. Paranthaman, A. O. Ijaduola, E. D. Specht, J. R. Thompson, D. K. Christen, S. J. Pennycook, and F. A. List. Irradiation-free, columnar defects comprised of self-assembled nanodots and nanorods resulting in strongly enhanced flux-pinning in $YBa_2Cu_3O_{7-\delta}$ films. *Supercond. Sci. Technol.*, 18:1533, 2005.

[12] S. H. Wee, Y. L. Zuev, C. Cantoni, and A. Goyal. Engineering nanocolumnar defect configurations for optimized vortex pinning in high temperature superconducting nanocomposite wires. *Sci. Rep.*, 3:2310:1–9, 2013.

[13] S. Chen, M. A. Sebastian, B. Gautam, J. Wilt, T. Haugan, Z. Xing, and J. Wu. Enhancement of isotropic pinning force in YBCO films with $BaZrO_3$ nanorods and $Y_2O_3$ nanoparticles. *IEEE T. Appl. Supercond.*, 27:8000205:1–5, 2017.

[14] S. R. Foltyn, L. Civale, J. L. MacManus-Driscoll, Q. X. Jia, B. Maiorov, H. Wang, and M. Maley. Materials science challenges for high-temperature superconducting wire. *Nat. Mater.*, 6:631–642, 2007.

[15] J. Gutiérrez, A. Llordés, J. Gázquez, M. Gibert, N. Romà, S. Ricart, A. Pomar, F. Sandiumenge, N. Mestres, T. Puig, and X. Obradors. Strong isotropic flux pinning in solution-derived $YBa_2Cu_3O_{7-x}$ nanocomposite superconducting films. *Nat. Mater.*, 6:367–373, 2007.

[16] G. Blatter, M.V. Feigel'man, V.B. Geshkenbein, A.I. Larkin, and V.M. Vinokur. Vortices in high-temperature superconductors. *Rev. Mod. Phys.*, 66:1125–1388, 1994.

[17] B. Gautam, M. A. Sebastian, S. Chen, S. Misra, J. Huang, F. J. Baca, R. Emergo, T. Haugan, Z. Xing, H. Wang, and J. Z. Wu. Probing the effect of interface on vortex pinning effiency of one-dimensional $BaZrO_3$ and $BaHfO_3$ artificial pinning centers in $YBa_2Cu_3O_{7+x}$ thin films. *Appl. Phys. Lett.*, 113:212602, 2018.

[18] C. Cantoni, Y. Gao, S. H. Wee, E. D. Specht, J. Gazquez, J. Meng, S. J. Pennycook, and A. Goyal. Strain-driven oxygen deficiency in self-assembled, nanostructured, composite oxide films. *ACS Nano*, 5:4783–4789, 2011.

[19] A. V. Narlikar. *Superconductors*. Oxford University Press, 2014.

[20] W. Meissner and R. Ochsenfeld. *Naturwissenschaft*, 21:787, 1933.

[21] C. P. Poole Jr., H. A. Farach, R. J. Creswick, and R. Prozorov. *Superconductivity, Second Edition*. Academic Press, 2007.

[22] U. Gottlieb, J. C. Lasjaunias, J. L. Tholence, O. Laborde, O. Thomas, and R. Madar. Superconductivity in $TaSi_2$ single crystals. *Phys. Rev. B*, 45:4803–4806, 1992.

[23] Z. A. Ren, J. Kato, T. Muranaka, J. Akimitsu, M. Kriener, and Y. Maeno. Superconductivity in boron-doped SiC. *J. Phys. Soc. Jpn*, 76:103710, 2007.

[24] J. G. Bednorz and K. A. Müller. Possible high-$T_c$ in the Ba-La-Cu-O system. *Z. Phys. B*, 64: 189–193, 1986.

[25] J. Orenstein and A..J. Millis. Advances in the physics of high-temperature superconductivity. *Science*, 288:468, 2000.

[26] G. Yao, M. Gao, Y. Ji, W. Liang, L. Gao, S. Zheng, Y. Wang, B. Pang, Y. B. Chen, H. Zeng, H. Li, Z. Wang, J. Liu, C. Chen, and Y. Lin. Surface step terrace tuned microstructures and dielectric properties of highly epitaxial $CaCu_3$ $Ti_4O_{12}$ thin films on vicinal $LaAlO_3$ substrates. *Sci. Rep.*, 6:34683, 2016.

[27] L. N. Cooper. *Physical Review*, 104:1189, 1956.

[28] T. Matsushita. Flux pinning in superconducting 123 materials. *Supercond. Sci. Technol.*, 13:730, 2000.

[29] S. Eley, A. Glatz, and R. Willa. Challenges and transformative opportunities in superconductor vortex physics. *J. Appl. Phys.*, 130:050901, 2021.

[30] E. H. Brandt. The flux-line lattice in superconductors. *Rep. Prog. Phys.*, 58:1465, 1995.

[31] N. Miura, H. Nakagawa, T. Sekitani, M. Naito, H. Sato, and Y. Enomoto. High-magnetic-field study of high-$T_c$ cuprates. *Physica B*, 319:310–320, 2002.

[32] W. Buckel and R. Kleiner. *Superconductivity: Fundamentals and Applications*. Wiley-VCH, 2004.

[33] R. P. Huebener. *Magnetic Flux Structures in Superconductors*. Springer-Verlag, 1979.

[34] D. R. Harshman and A. P. Mills Jr. Concerning the nature of high-$T_c$, superconductivity: Survey of experimental properties and implications for interlayer coupling. *Phys. Rev. B*, 45:10684–10712, 1992.

[35] J. D. Jorgensen, M. A. Beno, D. G. Hinks, L. Soderholm, K. J. Volin, R. L. Hitterman, J. D. Grace, I. K. Schuller, C. U. Serge, K. Zhang, and M. S. Kleefisch. Oxygen ordering and the orthorhombic-to-tetragonal phase transition in $YBa_2Cu_3O_{7-x}$. *Phys. Rev. B*, 36:3608–3616, 1987.

[36] J. D. Jorgensen, B. W. Veal, A. P. Paulikas, L. J. Nowicki, G. W. Crabtree, H. Claus, and W. K. Kwok. Structural properties of oxygen-deficient $YBa_2Cu_3O_{7-\delta}$. *Phys. Rev. B*, 41:1863–1877, 1990.

[37] D. Larbalestier, A. Gurevich, D. M. Feldmann, and A. Polyanskii. High-$T_c$ superconducting materials for electric power applications. *Nature*, 414:368–377, 2001.

[38] W. J. Gallagher. Studies at IBM on anisotropy in single crystals of the high-temperature oxide superconductor $Y_1Ba_2Cu_30_{7-x}$ (invited). *J. Appl. Phys.*, 63:4216, 1988.

[39] U. Welp, W. K. Kwok, G. W. Crabtree, K. G. Vandervoort, and J. Z. Liu. Magnetic measurements of the upper critical field of YBCO single crystals. *Phys. Rev. Lett.*, 62:1908, 1989.

[40] W. Lang, I. Puica, K. Siraj, M. Peruzzi, J.D. Pedarnig, and D. Bäuerle. Critical current enhancement in YBCO towards the intrinsic depairing value in short current pulses. *Physica C*, 406-462: 827, 2007.

[41] D. Dimos, P. Chaudhari, and J. Mannhart. Superconducting transport properties of grain boundaries in $YBa_2Cu_3O_{7-x}$ bicrystals. *Phys. Rev. B*, 41:4038, 1990.

[42] Teruo Matsushita. *Flux pinning in superconductors*. Springer, Heidelberg, Germany, 2007.

[43] B. Dam, J. M. Huijbregtse, F. C. Klaassen, R. C. F. van der Geest, G. Doornbos, J. H. Rector, A. M. Testa, S. Freisem, J. C. Martinez, B. Stuble-Pumpin, and R. Griessen. Origin of high critical currents in $YBa_2Cu_3O_{7-\delta}$ superconducting thin films. *Nature*, 399:439–442, 1999.

[44] F. C. Klaassen, G. Doornbos, J. M. Huijbregtse, R. C. F. van der Geest, B. Dam, and R. Griessen. Vortex pinning by natural linear defects in thin films of $YBa_2Cu_3O_{7-\delta}$. *Phys. Rev. B*, 64: 184523:1–20, 2001.

[45] A. Palau, F. Vallés, V. Rouco, M. Coll, Z. Li, C. Pop, B. Mundet, J. Gázquez, R. Guzman, J. Gutierrez, X. Obradors, and T. Puig. Disentangling vortex pinning landscape in chemical solution deposition superconducting $YBa_2Cu_3O_{7-x}$ films and nanocomposites. *Supercond. Sci. Technol.*, 31:034004, 2018.

[46] P. Paturi and H. Huhtinen. Roles of electron mean free path and flux pinning in optimizing the critical current in YBCO superconductors. *Supercond. Sci. Technol.*, 35:065007:1–9, 2022.

[47] C. J. van der Beek, M. Konczykowski, A. Abal'oshev, I. Abal'osheva, P. Gierlowski, S. J. Lewandowski, M. V. Indenbom, and S. Barbanera. Strong pinning in high-temperature superconducting films. *Phys. Rev. B*, 66:24523, 2002.

[48] B. Maiorov, S. A. Baily, H. Zhou, O. Ugurlu, J. A. Kennison, P. C. Dowden, T. G. Holesinger, S. R. Foltyn, and L. Civale. Synergetic combination of different types of defect to optimize pinning landscape using $BaZrO_3$-doped $YBa_2Cu_3O_7$. *Nat. Mater.*, 8:398–404, 2009.

[49] J. Plain, T. Puig, F. Sandiumenge, X. Obradors, and J. Rabier. Microstructural influence on critical currents and irreversibility line in melt-textured $YBa_2Cu_3O_{7-x}$ reannealed at high oxygen pressure. *Phys. Rev. B*, 65:104526, 2002.

[50] K. H. Fischer and T. Nattermann. Collective flux creep in high-$T_c$ superconductors. *Phys. Rev. B*, 43:10372, 1991.

[51] M. P. A. Fisher. Vortex-glass superconductivity: A possible new phase in bulk high-$T_c$ oxides. *Phys. Rev. Lett.*, 62:1415, 1989.

[52] G. Blatter, M. V. Feigel'man, V. B. Geshkenbein, A. I. Larkin, and V. M. Vinokur. Vortices in high-temperature superconductors. *Reviews of Modern Physics*, 66:1125–1388, 1994.

[53] D. R. Nelson and V. M. Vinokur. Boson localization and correlated pinning of superconducting vortex arrays. *Phys. Rev. B*, 48:13060, 1993.

[54] G. W. Crabtree and D. R. Nelson. Vortex physics in high temperature superconductors. *Phys. Today*, 50:38–45, 1997.

[55] D. R. Nelson. Vortex entanglement in HTS. *Phys. Rev. Lett.*, 60:1973, 1988.

[56] A. Houghton, R. A. Pelcovits, and A. Sudbg. Flux lattice melting in high-$T_c$, superconductors. *Phys. Rev. B*, 40:6763–6770, 1989.

[57] J. M. Huijbregtse, F. C. Klaassen, A. Szepielow, J. H. Rector, B. Dam, R. Griessen, B. J. Kooi, and J. Th. M. de Hosson. Vortex pinning by natural defects in thin films of $YBa_2Cu_3O_{7-\delta}$. *Supercond. Sci. Technol.*, 15:395–404, 2002.

[58] R. M. Schalk, K. Kundzins, H. W. Weber, E. Stangl, S. Proyer, and D. Bäuerle. STM observation of dislocation chains suitable for flux pinning in YBCO films. *Physica C*, 257:341, 1996.

[59] B. Dam, N. J. Koeman, J. H. Rector, B. Stäuble-Pümpin, U. Poppe, and R. Griessen. Growth and etching phenomena observed by STM/AFM on pulsed-laser deposited $YBa_2Cu_3O_{7-\delta}$ films. *Physica C*, 261:1, 1996.

[60] J. M. Huijbregtse, B. Dam, R. C. F. van der Geest, F. C. Klaassen, R. Elberse, J. H. Rector, and R. Griessen. Natural strong pinning sites in laser-ablated YBCO thin films. *Phys. Rev. B*, 62: 1338, 2000.

[61] B. Dam, J. M. Huijbregtse, and J. H. Rector. Strong pinning linear defects formed at the coherent growth transition of pulsed-laser-deposited $YBa_2Cu_3O_{7-\delta}$ films. *Phys. Rev. B*, 65:064528:1–8, 2002.

[62] A. V. Pan and S. X. Dou. Comparison of small-field behavior in $MgB_2$, low- and high-temperature superconductors. *Phys. Rev. B*, 73:052506, 2006.

[63] J. Wang, J. H. Kwon, J. Yoon, H. Wang, T. J. Haugan, F. J. Baca, N. A. Pierce, and P. N. Barnes. Flux pinning in $YBa_2Cu_3O_{7-\delta}$ thin film samples linked to stacking fault density. *Appl. Phys. Lett.*, 92:082507, 2008.

[64] B. Schey, W. Biegel, M. Kuhn, and B. Stritzker. Large-area pulsed laser deposition of YBCO thin films homogeneity and surface. *Applied Physics A*, 69:S419, 1999.

[65] M. Miura, M. Yoshizumi, T. Izumi, and Y. Shiohara. Formation mechanism of $BaZrO_3$ nanoparticles in $Y_{1-x}Sm_xBa_2Cu_3O_y$-coated conductors derived from trifluoroacetate metalorganic deposition. *Supercond. Sci. Technol.*, 23:014013, 2010.

[66] A. Ignatiev, Q. Zhong, P. C. Chou, X. Zhang, J. R. Liu, and W. K. Chu. Large $j_c$ enhancement by ion irradiation for thick YBCO films prepared by photoassisted metalorganic chemical vapor deposition. *Appl. Phys. Lett.*, 70:1474, 1997.

[67] H. Yamasaki. Effect of particle size on the flux pinning properties of $YBa_2Cu_3O_{7-\delta}$ thin films containing fine $Y_2O_3$ nanoprecipitates. *Supercond. Sci. Technol.*, 29:065005, 2016.

[68] R. L. S. Emergo, F. J. Baca, J. Z. Wu, T. J. Haugan, and P. N. Barnes. The effect of thickness and substrate tilt on the BZO splay and superconducting properties of $YBa_2Cu_3O_{7-\delta}$ films. *Supercond. Sci. Technol.*, 23:115010, 2010.

[69] L. Civale, A. D. Marwick, T. K. Worthington, M. A. Kirk, J. R. Thompson, L. Krusin-Elbaum, Y. Sun, J. R. Clem, and F. Holtzberg. Vortex confinement by columnar defects in YBCO crystals: Enhanced pinning at high fields and temperatures. *Phys. Rev. Lett.*, 67:648, 1991.

[70] J. L. MacManus-Driscoll, S. R. Foltyn, Q. X. Jia, H. Wang, A. Serquis, L. Civale, B. Maiorov, M. E. Hawley, M. P. Maley, and D. E. Peterson. Strongly enhanced current densities in superconducting coated conductors of $YBa_2Cu_3O_{7-x}$+$BaZrO_3$. *Nat. Mater.*, 3:439–443, 2004.

[71] Ch. Jooss, R. Warthmann, H. Kronmuller, T. Haage, H.-U. Habermeier, and J. Zegenhagen. Vortex pinning due to strong quasiparticle scattering at antiphase boundaries in YBCO. *Phys. Rev. Lett.*, 82:632, 1999.

[72] T. G. Holesinger, L. Civale, B. Maiorov, D. M. Feldmann, J. Y. Coulter, D. J. Miller, V. A. Maroni, Z. Chen, D. C. Larbalestier, R. Feenstra, X. Li, Y. Huang, T. Kodenkandath, W. Zhang, M. W. Rupich, and A. P. Malozemoff. Progress in nanoengineered microstructures for tunable high-current, high-temperature superconducting wires. *Adv. Mater.*, 20:391–407, 2008.

[73] D. M. Feldmann, T. G. Holesinger, B. Maiorov, S. R. Foltyn, J. Y. Coulter, and I. Apodaca. Improved flux pinning in $YBa_2Cu_3O_7$ with nanorods of the double perovskite $Ba_2YNbO_6$. *Supercond. Sci. Technol.*, 23:095004, 2010.

[74] X. Song, Z. Chen, S. I. Kim, D. M. Feldmann, D. Larbalestier, J. Reeves, Y. Xie, and V. Selvamanickam. Evidence for strong flux pinning by small, dense nanoprecipitates in a Sm-doped $YBa_2Cu_3O_{7-\delta}$ coated conductor. *Appl. Phys. Lett.*, 88:212508, 2006.

[75] Z. Chen, D. M. Feldmann, X. Song, S. I. Kim, A. Gurevich, J. L. Reeves, Y. Y. Xie, V. Selvamanickam, and D. C. Larbalestier. Three-dimensional vortex pinning by nano-precipitates in a Sm-doped $YBa_2Cu_3O_{7-x}$ coated conductor. *Supercond. Sci. Technol.*, 20:S205, 2007.

[76] V. Selvamanickam, Y. Chen, Y. Zhang, A. Guevara, T. Shi, Y. Yao, G. Majkic, C. Lei, E. Galtsyan, and D. J. Miller. Effect of rare-earth composition on microstructure and pinning properties of Zr-doped (Gd, Y)$Ba_2Cu_3O_x$ superconducting tapes. *Supercond. Sci. Technol.*, 25:045012, 2012.

[77] T. G. Holesinger, B. Maiorov, O. Ugurlu, L. Civale, Y. Chen, X. Xiong, Y. Xie, and V. Selvamanickam. Microstructural and superconducting properties of high current metalorganic chemical

vapor deposition $YBa_2Cu_3O_{7-\delta}$ coated conductor wires. *Supercond. Sci. Technol.*, 22:045025, 2009.

[78] Z. Chen, F. Kametani, A. Gurevich, and D. Larbalestier. Pinning, thermally activated depinning and their importance for tuning the nanoprecipitate size and density in high $J_c$ $YBa_2Cu_3O_{7-x}$ films. *Physica C*, 469:2021, 2009.

[79] G. Ercolano, M. Bianchetti, S. C. Wimbush, S. A. Harrington, H. Wang, J. H. Lee, and J. L. MacManus-Driscoll. State-of-the-art flux pinning in $YBa_2Cu_3O_{7-\delta}$ by the creation of highly linear, segmented nanorods of $Ba_2$(Y/Gd)(Nb/Ta)$O_6$ together with nanoparticles of (Y/Gd)$_2O_3$ and (Y/Gd)$Ba_2Cu_4O_8$. *Supercond. Sci. Technol.*, 24:095012, 2011.

[80] F. Lu, F. Kametani, and E. E. Hellstrom. Film growth of $BaZrO_3$ -doped $YBa_2Cu_3O_{7-\delta}$ by using fluorine-free metal-organic deposition. *Supercond. Sci. Technol.*, 25:015011, 2012.

[81] S. C. Wimbush, J. H. Durrell, C. F. Tsai, H. Wang, Q. X. Jia, M. G. Blamire, and J. L. MacManus-Driscoll. Enhanced critical current in $YBa_2Cu_3O_{7-\delta}$ thin films through pinning by ferromagnetic $YFeO_3$ nanoparticles. *Supercond. Sci. Technol.*, 23:045019, 2010.

[82] M. Konishi, K. Takahashi, A. Ibi, T. Muroga, S. Miyata, H. Kobayashi, Y. Yamada, and Y. Shiohara. $J_c$–B characteristics of REBaCuO (RE = Sm, Er and [Gd, Er]) films on PLD-$CeO_2$ /IBAD-GZO/metal substrates. *Physica C*, 445-448:633–636, 2006.

[83] C. Cai, B. Holzapfel, J. Hänisch, L. Fernandez, and L. Schultz. Magnetotransport and flux pinning characterictics in RBaCuO (R=Gd,Eu,Nd) and ($Gd_{1/3}Eu_{1/3}Nd_{1/3}$)BaCuO high-$T_c$ superconducting thin films on $SrTiO_3$. *Phys. Rev. B*, 69:104531:1–8, 2004.

[84] N. M. Strickland, E. F. Talantsev, N. J. Long, J. A. Xia, S. D. Searle, J. Kennedy, A. Markwitz, M. W. Rupich, X. Li, and S. Sathyamurthy. Flux pinning by discontinuous columnar defects in 74 MeV Ag-irradiated $YBa_2Cu_3O_7$ coated conductors. *Physica C*, 469:2060–2067, 2009.

[85] P. Mele, K. Matsumoto, T. Horide, A. Ichinose, M. Mukaida, Y. Yoshida, S. Horii, and R. Kita. Ultra-high flux pinning properties of $BaMO_3$-doped $YBa_2Cu_3O_{7-x}$thin films (M = Zr, Sn). *Supercond. Sci. Technol.*, 21:032002, 2008.

[86] Y. Yamada, K. Takahashi, H. Kobayashi, M. Konishi, T. Watanabe, A. Ibi, T. Muroga, S. Miyata, T. Kato, T. Hirayama, and Y. Shiohara. Epitaxial nanostructure and defects effective for pinning in Y(RE)$Ba_2Cu_3O_{7-x}$ coated conductors. *Appl. Phys. Lett.*, 87:132502, 2005.

[87] A. Goyal, S. Kang, K. J. Leonard, P. M. Martin, A. A. Gapud, M. Varela, M. Paranthaman, A. O. Ijadoula, E. D. Specht, J. R. Thompson, D. K. Christen, S. J. Pennycook, and F. A. List. Irradiation free, columnar defects comprised of self-assembled nanodots and nanorods resulting in strongly enhanced flux pinning in $YBa_2Cu_3O_{7-\delta}$ films. *Supercond. Sci. Technol.*, 18:1533–1538, 2005.

[88] A. Crisan, V. S. Dang, P. Mikheenko, A. M. Ionescu, I. Ivan, and L. Miu. Synergetic pinning centres in $BaZrO_3$ -doped $YBa_2Cu_3O_{7-x}$ films induced by $SrTiO_3$ nano- layers. *Supercond. Sci. Technol.*, 30:045012, 2017.

[89] I. A. Sadovskyy, Y. Jia, M. Leroux, J. Kwon, H. Hu, L. Fang, C. Chaparro, S. Zhu, U. Welp, J.-M. Zuo, Y. Zhang, R. Nakasaki, V. Selvamanickam, G. W. Crabtree, A. E. Koshelev, A. Glatz, and W.-K. Kwok. Toward superconducting critical current by design. *Advanced Materials*, 28: 4593–4600, 2016.

[90] M. Yazdani-Asrami, A. Sadeghi, W. Song, A. Madureira, J. Murta-Pina, A. Morandi, and M. Parizh. Artificial intelligence methods for applied superconductivity: material, design, manufacturing, testing, operation, and condition monitoring. *Supercond. Sci. Technol.*, 35:123001, 2022.

[91] S. H. Wee, A. Goyal, E. D. Specht, C. Cantoni, Y. L. Zuev, V. Selvamanickam, and S. Cook. Enhanced flux pinning and critical current density via incorporation of self-assembled rare-earth barium tantalate nanocolumns within $YBa_2Cu_3O_{7-\delta}$ films. *Phys. Rev. B*, 81:140503, 2010.

[92] F. J. Baca, P. N. Barnes, R. L. S. Emergo, T. J. Haugan, J. N. Reichart, and J. Z. Wu. Control of BZO nanorod alignment in YBCO thin films by microstructural modulation. *Appl. Phys. Lett.*, 94:102512, 2009.

[93] S. A. Harrington, J. H. Durrell, B. Maiorov, H. Wang, S. C. Wimbush, A. Kursumovic, J. H. Lee, and J. L. MacManus-Driscoll. Self-assembled, rare earth tantalate pyrochlore nanoparticles for superior flux pinning in $YBa_2Cu_3O_7$ films. *Supercond. Sci. Technol.*, 22:2, 2008.

[94] J. J. Shi and J. Z. Wu. Influence of the lattice strain decay on the diameter of self assembled secondary phase nanorod array in epitaxial films. *J. Appl. Phys.*, 118:164301:1–7, 2015.

[95] J. Wu and J. Shi. Interactive modeling-synthesis- characterization approach towards controllable in situ self-assembly of artificial pinning centers in RE-123 films. *Supercond. Sci. Technol.*, 30: 103002, 2017.

[96] M. Peurla, H. Huhtinen, M. A. Shakhov, K. Traito, Yu. P. Stepanov, M. Safonchik, P. Paturi, Y. Y. Tse, R. Palai, and R. Laiho. Effects of nanocrystalline target and columnar defects on flux pinning in pure and BZO-doped YBCO films in fields up to 30 T. *Phys. Rev. B*, 75:184524:1–6, 2007.

[97] Y. Li, K. Zdun, L. Hope, J. Xie, S. Corcoran, Y. Qiao, J. Reeves, K. Lenseth, and V. Selvamanickam. Texture development and superconducting properties of YBCO thick films deposited on buffered metal substrates at various deposition rates. *IEEE T. Appl. Supercond.*, 13:2758–2761, 2003.

[98] Y. Zhao, J.-M. Zhu, G.-Y. Jiang, C.-S. Chen, W. Wu, Z.-W. Zhang, S. K. Chen, Y. M. Hong, Z.-Y. Hong, and Z.-J. Jin. Progress in fabrication of second generation high temperature superconducting tape at Shanghai Superconductor Technology. *Supercond. Sci. Technol.*, 32:044004, 2019.

[99] M. Peurla, P. Paturi, Yu. P. Stepanov, H. Huhtinen, Y. Y. Tse, A. C. Bódi, J. Raittila, and R. Laiho. Optimization of the $BaZrO_3$ concentration in YBCO films prepared by pulsed laser deposition. *Supercond. Sci. Technol.*, 19:767–771, 2006.

[100] D Uglietti. A review of commercial high temperature superconducting materials for large magnets: from wires and tapes to cables and conductors. *Supercond. Sci. Technol.*, 32:053001, 2019.

[101] C. V. Varanasi, J. Burke, L. Brunke, H. Wang, M. Sumption, and P. N. Barnes. Enhancement and angular dependence of transport critical current density in pulsed laser deposited $YBa_2Cu_3O_{7-x}$+$BaSnO_3$ films in applied magnetic fields. *J. Appl. Phys.*, 102:063909:1–5, 2007.

[102] S. H. Wee, A. Goyal, Y. L. Zuev, and C. Cantoni. High performance superconducting wire in high applied magnetic fields via nanoscale defect engineering. *Supercond. Sci. Technol.*, 21: 092001:1–4, 2008.

[103] X. Obradors and T. Puig. Coated conductors for power applications: materials challenges. *Supercond. Sci. Technol.*, 27:044003:1–17, 2014.

[104] A. Stangl, A. Palau, G. Deutscher, X. Obradors, and T. Puig. Ultra-high critical current densities of superconducting $YBa_2Cu_3O_{7-\delta}$ thin films in the overdoped state. *Sci. Rep.*, 11:8176:1–12, 2021.

[105] E. Rivasto, T. Hynninen, H. Huhtinen, and P. Paturi. Optimization of high-temperature superconducting bilayer structures using a vortex dynamics simulation. *J. Phys. Cond. Mat.*, 35: 075701:1–10, 2023.

[106] J. Zhang, H. Wu, G. Zhao, L. Han, and J. Zhang. Progress in the study of vortex pinning centers in high-temperature superconducting films. *Nanomaterials*, 12:4000:1–23, 2022.

[107] H. Huhtinen, M. Irjala, P. Paturi, and M. Falter. Optimal BZO doping in YBCO films grown on single crystal STO and NiW substrates. *IEEE T. Appl. Supercond.*, 21:2753–2757, 2010.

[108] A. Ichinose, K. Naoe, T. Horide, K. Matsumoto, R. Kita, M. Mukaida, Y. Yoshida, and S. Horii. Microstructures and critical current densities of YBCO films containing structure-controlled $BaZrO_3$ nanorods. *Supercond. Sci. Technol.*, 20:1144–1150, 2007.

[109] M. M. Aye, E. Rivasto, M. Z. Khan, H. Rijckaert, E. Salojärvi, C. Haalisto, E. Mäkilä, H. Palonen, H. Huhtinen, I. Van Driessche, and P. Paturi. Control of the nanosized defect network in superconducting thin films by target grain size. *Sci. Rep.*, 11:6010:1–11, 2021.

[110] M. M. Aye, M. Z. Khan, E. Rivasto, J. Tikkanen, H. Huhtinen, and P. Paturi. Role of columnar defect size in angular dependent flux pinning properties of YBCO thin films. *IEEE T. Appl. Supercond.*, 29:8000805:1–5, 2019.

[111] J. L. MacManus-Driscoll, B. Maiorov, J. Durrell, S. Foltyn, Q. X. Jia, L. Civale, H. Wang, A. Kursumovic, and D. E. Peterson. Guidelines for optimizing random and correlated pinning in rare-earth-based superconducting films. *Supercond. Sci. Technol.*, 19:S55–S59, 2006.

[112] E. F. Talantsev and J. L. Tallon. Universal self-field critical current for thin-film superconductors. *Nat. Commun.*, 6:7820:1–8, 2015.

[113] E. F. Talantsev, W. P. Crump, and J. L. Tallon. Universal scaling of the self-field critical current in superconductors: from sub-nanometre to millimetre size. *Sci. Rep.*, 7:10010:1–15, 2017.

[114] B. Gautam, M. A. Sebastian, S. Chen, T. Haugan, W. Zhang, J. Huang, H. Wang, and J. Wu. Microscopic adaptation of $BaHfO_3$ and $Y_2O_3$ artificial pinning centers for strong and isotropic pinning landscape in $YBa_2Cu_3O_{7-x}$ thin films. *Supercond. Sci. Technol.*, 31:025008, 2018.

[115] B. P. Uberuaga, P. P. Dholabhai, G. Pilania, and A. Chen. Semicoherent oxide heterointerfaces: Structure, properties, and implications. *APL Materials*, 7:100904, 2019.

[116] S. R. Foltyn, L. Civale, J. L. MacManus-Driscoll, Q. X. Jia, B. Maiorov, H. Wang, and M. Maley. Materials science challenges for high-temperature superconducting wire. *Nat. Mater.*, 6:631, 2007.

[117] P. Mele, K. Matsumoto, A. Ichinose, M. Kukaida, Y. Yoshida, S. Horii, and R. Kita. Systematic study of the $BaSnO_3$ insertion effect on the properties of $YBa_2Cu_3O_{7-x}$ films prepared by pulsed laser ablation. *Supercond. Sci. Technol.*, 21:125017:1–6, 2008.

[118] C. N. R. Rao, R. Nagarajan, and R. Vijayaraghavan. Synthesis of cuprate superconductors. *Supercond. Sci. Technol.*, 6:1–22, 1993.

[119] J. Raittila, H. Huhtinen, P. Paturi, and Y. P. Stepanov. Preparation of superconducting $YBa_2Cu_3O_{7-\delta}$ nanopowder by deoxydation in Ar before final oxygenation. *Physica C*, 371: 90–96, 2002.

[120] H. M. Smith and A. F. Turner. *Applied Optics*, 4:147, 1965.

[121] D. Dijkkamp, T. Venkatesan, X. D. Wu, S. A. Shaheen, N. Jisrawi, Y. H. Min-Lee, W. L. McLean, and M. Croft. Preparation of Y-Ba-Cu oxide superconductor thin films using pulsed laser evaporation from high $T_c$ bulk material. *Appl. Phys. Lett.*, 51:619, 1987.

[122] D. B. Chrisey and G. K. Hubler. *Pulsed Laser Deposition of Thin Films*. John Wiley Sons, 1994.

[123] M. Z. Khan, M. Malmivirta, X. Wu Y. Zhao, R. Jha, V. P. S Awana, H. Huhtinen, and P. Paturi. Angular and field dependent flux pinning in artificially doped YBCO films on IBAD-MgO based template. *Physica C*, 555:15–23, 2018.

[124] M. M. Aye, E. Rivasto, H. Rijckaert, S. Granroth, H. Palonen, H. Huhtinen, I. Van Driessche, and P. Paturi. Role of deposition distance on nanorod growth and flux pinning in BZO doped YBCO thin films: Implications for superconducting tapes. *ACS Applied Nano Materials*, 5: 18159–18167, 2022.

[125] H. Huhtinen, K. Schlesier, and P. Paturi. Growth and $c$-axis flux pinning of nanostructured YBCO/BZO multilayers. *Supercond. Sci. Technol.*, 22:075019:1–8, 2009.

[126] D. B. Williams and C. D. Carter. *Transmission Electron Microscopy: A Textbook for Materials Science*. New York : Springer, 1996.

[127] H. P. Wiesinger, F. M. Sauerzopf, and H. W. Weber. On the calculation of $J_c$ from magnetization measurements on superconductors. *Physica C*, 203:121–128, 1992.

[128] X. Wang, F. J. Baca, R. L. S. Emergo, J. Z. Wu, T. J. Haugan, and P. N. Barnes. Eliminating thickness dependence of critical current density in $YBa_2Cu_3O_{7-x}$ films with aligned $BaZrO_3$ nanorods. *J. Appl. Phys.*, 108:113911, 2010.

[129] E. Rivasto, M. Z. Khan, Y. Wu, Y. Zhao, C. Chen, J. Zhu, H. Huhtinen, and P. Paturi. Lattice defect induced nanorod growth in YBCO films deposited on an advanced IBAD-MgO template. *Supercond. Sci. Technol.*, 33:075008:1–8, 2020.

[130] C. V. Varanasi, P. N. Barnes, J. Burke, L. Brunke, I. Maartense, T. J. Haugan, E. A. Stinzianni, K. A. Dunn, and P. Haldar. Flux pinning enhancement in YBCO films with $BaSnO_3$ nanoparticles. *Supercond. Sci. Technol.*, 19:L37, 2006.

[131] P. Mele, K. Matsumoto, T. Horide, A. Ichinose, M. Mukaida, Y. Yoshida, and S. Horii. Insertion of nanoparticulate artificial pinning centres in $YBa_2Cu_3O_{7-x}$ films by laser ablation of a $Y_2O_3$-surface modified target. *Supercond. Sci. Technol.*, 20:616–620, 2007.

[132] T. Haage, J. Zegenhagen, J. Q. Li, H.-U. Habermeier, and M. Cardona. Transport properties and flux pinning by self-organization in YBCO films on vicinal $SrTiO_3$ (001). *Phys. Rev. B*, 56: 8404–8418, 1997.

[133] Douglas H. Lowndes, X.-Y. Zheng, Shen Zhu, J. D. Budai, and R. J. Warmack. Suppression of the spiral-growth mechanism in epitaxial $YBa_2Cu_3O_{7-x}$ films grown on miscut substrates. *Appl. Phys. Lett.*, 61:852–854, 1992.

[134] P. Berghuis, E. Di Bartolomeo, G. A. Wagner, and J. E. Evetts. Intrinsic channeling of vortices along the ab plane in vicinal $YBa_2Cu_3O_{7-\delta}$ films. *Phys. Rev. Lett.*, 79:2332–2335, 1997.

[135] J. Brötz, H. Fuess, T. Haage, and J. Zegenhagen. Controlled modification of interfacial strain and twinning in $YBa_2Cu_3O_{7-\delta}$ films on vicinal $SrTiO_3$ (001)... *Phys. Rev. B*, 57:3679–3682, 1998.

[136] J. H. Durrell, J. E. Evetts, R. Rössler, M. P. Delamare, J. D. Pedarnig, and D. Bäuerle. Effect of varying material anisotropy on critical current anisotropy in vicinal $YBa_2Cu_3O_{7-\delta}$ thin films. *Appl. Phys. Lett.*, 83:4999–5001, 2003.

[137] G. Yao, M. Gao, Y. Ji, W. Liang, L. Gao, S. Zheng, Y. Wang, B. Pang, Y. B. Chen, H. Zeng, H. Li, Z. Wang, J. Liu, C. Chen, and Y. Lin. Surface step terrace tuned microstructures and dielectric properties of highly epitaxial $CaCu_3Ti_4O_{12}$ thin films on vicinal $LaAlO_3$ substrates. *Sci. Rep.*, 6:34683:1–11, 2016.

[138] F. J. Baca, R. L. Emergo, J. Z. Wu, T. J. Haugan, J. N. Reichart, and P. N. Barnes. Microstructural characterization of $YBa_2Cu_3O_{7-\delta}$ films with $BaZrO_3$ nanorods grown on vicinal $SrTiO_3$ substrates. *IEEE T. Appl. Supercond.*, 19:3371–3374, 2009.

[139] V. Ogunjimi, B. Gautam, M. A. Sebastian, T. Haugan, and J. Wu. The effect of APC/YBCO interface on the angular range of effective pinning by one-dimensional artificial pinning centers in $YBa_2$ $Cu_3$ $O_{7-x}$ nanocomposite films. *Mater. Sci. Eng.*, 756:012025, 2020.

[140] T. Haage, J. Zegenhagen, Ch. Jooss, R. Warthmann, J. Q. Li, H.-U. Habermeier, and M. Cardona. Nanoscale engineering: Tailored properties by self-organization in $YBa_2Cu_3O_{7-\delta}$ thin films. *Physica C*, 282-287:557, 1997.

[141] J. D. Pedarnig, R. Rssler, M. P. Delamare, W. Lang, and D. Brle. Electrical properties, texture, and microstructure of vicinal $YBa_2Cu_3O_{7-\delta}$ thin films. *Appl. Phys. Lett.*, 81:2587–2589, 2002.

[142] T. Haugan, P. N. Barnes, R. Wheeler, F. Meisenkothen, and M. Sumption. Addition of nanoparticle dispersions to enhance flux pinning of the $YBa_2Cu_3O_{7-x}$ superconductor. *Nature*, 430:867, 2004.

[143] J. Z. Wu, J. J. Shi, J. F. Baca, R. Emergo, T. J. Haugan, B. Maiorov, and T. Holesinger. The effect of lattice strain on the diameter of $BaZrO_3$ nanorods in epitaxial $YBa_2Cu_3O_{7-\delta}$ films. *Supercond. Sci. Technol.*, 27:044010:1–7, 2014.

[144] J. Wu and J. Shi. Interactive modeling-synthesis-characterization approach towards controllable in situ self-assembly of artificial pinning centers in RE-123 films. *Supercond. Sci. Technol.*, 30: 103002:1–15, 2017.

[145] N. J. Long. Model for the angular dependence of critical currents in technical superconductors. *Supercond. Sci. Technol.*, 21:025007:1–8, 2008.

[146] E. Rivasto, M. Z. Khan, M. Malmivirta, H. Rijckaert, M. M. Aye, T. Hynninen, H. Huhtinen, I. Van Driessche, and P. Paturi. Self-assembled nanorods in YBCO matrix – a computational study of their effects on critical current anisotropy. *Sci. Reports*, 10:3169:1–14, 2020.

[147] S. R. Foltyn, Q. X. Jia, P. N. Arendt, L. Kinder, Y. Fan, and J. F. Smith. Relationship between film thickness and the critical current of $YBa_2Cu_3O_{7-\delta}$-coated conductors. *Appl. Phys. Lett.*, 75:3692–3694, 1999.

[148] Q. X. Jia, S. R. Foltyn, P. N. Arendt, and J. F. Smith. High-temperature superconducting thick films with enhanced supercurrent carrying capability. *Appl. Phys. Lett.*, 80:1601–1603, 2002.

[149] S. R. Foltyn, H. Wang, L. Civale, Q. X. Jia, P. N. Arendt, B. Maiorov, Y. Li, and M. P. Maley. Overcoming the barrier to 1000 A/cm width superconducting coatings. *Appl. Phys. Lett.*, 87: 162505:1–3, 2005.

[150] Y. L. Cheung, E. F. Maher, J. S. Abell, I. P. Jones, and Y. Y. Tse. Microstructural study of a YBCO multilayer coated conductor cylinder. *Supercond. Sci. Technol.*, 20:511–515, 2007.

[151] H. Kobayashi, Y. Yamada, A. Ibi, S. Miyata, Y. Shiohara, T. Kato, and T. Hirayama. Investigation of in-field properties of YBCO multi-layer film on PLD/IBAD metal substrate. *Physica C*, 463–465:661–664, 2007.

[152] S. Kang, K. J. Leonard, P. M. Martim, J. Li, and A. Goyal. Strong enhancements of flux pinning in YBCO multilayers with columnar defects comprised of self-assembled $BaZrO_3$ nanodots. *Supercond. Sci. Technol.*, 20:11, 2007.

[153] K. Matsumoto, I. Tanaka, T. Horide, P. Mele, Y. Yoshida, and S. Awaji. Irreversibility fields and critical current densities in strongly pinned $YBa_2Cu_3O_{7-x}$ films with $BaSnO_3$ nanorods: The influence of segmented $BaSnO_3$ nanorods. *J. Appl. Phys.*, 116:163903:1–7, 2014.

[154] Y. Liu and G. Du. Preparation and flux-pinning properties of multilayered yttrium barium copper oxide thin films containing alternating barium zirconate and yttria nanostructures. *Journal of Electronic Materials*, 40:1512–1516, 2011.

[155] M. Malmivirta, H. Rijckaert, V. Paasonen, H. Huhtinen, T. Hynninen, R. Jha, V. S. Awana, I. Van Driessche, and P. Paturi. Enhanced flux pinning in YBCO multilayer films with BCO nanodots and segmented BZO nanorods. *Sci. Reports*, 7:14682:1–8, 2017.

[156] J. Z. Wu, J. J. Shi nd F. J. Baca, R. Emergo, J. Wilt, and T. J. Haugan. Controlling $BaZrO_3$ nanostructure orientation in $YBa_2Cu_3O_{7-\delta}$ films for a three-dimensional pinning landscape. *Supercond. Sci. Technol.*, 28:125009, 2015.

[157] H. Yang, H. Wang, B. Maiorov, J. Lee, D. Talbayev, M. J. Hinton, D. M. Feldmann, J. L. MacManus-Driscoll, A. J. Taylor, L. Civale, and T. R. Lemberger. Self-assembled multilayers and enhanced superconductivity in $(YBa_2Cu_3O_{7-x})_{0.5}$:$(BaZrO_3)_{0.5}$ nanocomposite films. *J. Appl. Phys.*, 106:093914:1–4, 2009.

[158] R. Zhao, W. Li, J. H. Lee, E. M. Choi, Y. Liang, W. Zhang, R. Tang, H. Wang, Q. Jia, J. L. MacManus-Driscoll, and H. Yang. Precise tuning of $(YBa_2Cu_3O_{7-\delta})_{1-x}$ : $(BaZrO_3)_x$ thin films nanocomposite structures. *Adv. Funct. Mater.*, 24:5240–5245, 2014.

[159] J. He, R. F. Klie, G. Logvenov, I. Bozovic, and Y. Zhu. Microstructure and possible strain relaxation mechanisms of $La_2CuO_{4+\delta}$ thin films grown on $LaSrAlO_4$ and $SrTiO_3$ substrates. *J. Appl. Phys.*, 101:073906:1–6, 2007.

[160] T. Matsushita, M. Kiuchi, T. Yasuda, H. Wada, T. Uchiyama, and I. Iguchi. Thickness dependence of pinning properties in Bi-2212 superconductor. *Supercond. Sci. Technol.*, 18:1348, 2005.

[161] H. Zhang, J. Yang, S. Wang, Y. Wu, Q. Lv, and S. Li. Film thickness dependence of microstructure and superconductive property of PLD prepared YBCO layers. *Physica C*, 499:54–56, 2014.

[162] A. A. Gapud, D. Kumar, S. K. Viswanathan, C. Cantoni, M. Varela, J. Abiade, S. J. Pennycook, and D. K. Christen. Enhancement of flux pinning in YBCO thin films embedded with epitaxially grown $Y_2O_3$ nanostructures using multi-layering process. *Supercond. Sci. Technol.*, 18:1502, 2005.

[163] T. J. Haugan, P. N. Barnes, T. A. Campbell, N. A. Pierce, F. J. Baca, and I. Maartense. Flux pinning of Y-Ba-Cu-O films doped with $BaZrO_3$ nanoparticles by multilayer and single target methods. *IEEE T. Appl. Supercond.*, 17:3724, 2007.

[164] C. Cai, B. Holzapfel, J. Hänisch, and L. Schultz. Superconductivity suppression and flux-pinning crossover in artificial multilayers of ternary $RBa_2Cu_3O_{7-\delta}$ (R = Gd, Nd and Eu). *Phys. Rev. B*, 70:064504, 2004.

[165] A. V. Pan, S. V. Pysarenko, D. Wexler, S. Rubanov, M. Ionescu, and S. X. Dou. Multilayered deposition and its role in the enhancement of $YBa_2Cu_3O_7$ film performance. *Physica C*, 460-462:1379, 2007.

[166] A. Schmehl, B. Goetz, R. R. Schulz, C. W. Schneider, H. Bielefeldt, H. Hilgenkamp, and J. Mannhart. Doping-induced enhancement of the critical currents of grain boundaries in $YBa_2Cu_3O_{7-\delta}$. *Europhysics Letters*, 47:110–115, 1999.

[167] G. Hammerl, A. Schmehl, R. R. Schulz, B. Goetz, H. Bielefeldt, C. W. Schneider, H. Hilgenkamp, and J. Mannhart. Enhanced supercurrent density in polycrystalline $YBa_2Cu_3O_{7-\delta}$ at 77 K from calcium doping of grain boundaries. *Nature*, 407:162–164, 2000.

[168] V. Ogunjimi, M. A. Sebastian, D. Zhang, B. Gautam, J. Jian, J. Huang, Y. Zhang, T. Haugan, H. Wang, and J. Wu. Enhancing magnetic pinning by $BaZrO_3$ nanorods forming coherent interface by strain-directed Ca-doping in $YBa_2Cu_3O_{7-x}$ nanocomposite films. *Supercond. Sci. Technol.*, 34:104002, 2021.

[169] J. L. Tallon, D. M. Pooke, M. P. Staines, M. E. Bowden, N. E. Flower, R. G. Buckley, M. R. Presland, and R. L. Davis. Giant enhancement of oxygen mobility in high-$T_c$ superconductors by atomic substitution. *Physica C*, 171:61–68, 1990.

[170] J. T. Kucera and J. C. Bravman. Transport characterization of calcium-doped YBCO thin films. *Phys. Rev. B*, 51:8582–8590, 1995.

[171] Y. Zhao, H. K. Liu, and S. X. Dou. Effect of co-doping of Ca and Al on hole concentration and superconductivity in the YBCO system. *Physica C*, 179:207–213, 1991.

[172] M. M. Aye, E. Rivasto, T. Vaimala, Y. Zhao, H. Huhtinen, and P. Paturi. Improved crystalline quality and self-field $J_c$ in sequentially vacuum-multilayered YBCO thin films on buffered metallic templates. *IEEE T. Appl. Supercond.*, 33:6601806:1–6, 2023.

[173] A. Tuomola, E. Rivasto, M. M. Aye, Y. Zhao, H. Huhtinen, and P. Paturi. Defining optimal thickness for maximal self-field $J_c$ in YBCO/$CeO_2$ multilayers grown on buffered metal. *J. Phys. Cond. Mat.*, 35:475001:1–9, 2023.

[174] J. Ye and K. Nakamura. Quantitative structure analyses of YBCO thin films: Determination of oxygen content from x-ray-diffraction patterns. *Phys. Rev. B*, 48:7554–7564, 1993.

[175] T. Horide, F. Kametani, S. Yoshioka, T. Kitamura, and K. Matsumoto. Structural evolution induced by interfacial lattice mismatch in self-organized $YBa_2Cu_3O_{7-\delta}$ nanocomposite film. *ACS Nano*, 11:1780–1788, 2017.

[176] T. Horide, M. Ishimaru, and K. Matsumoto. Observation of inhomogeneous depinning in $YBa_2Cu_3O_7$ composite multilayers. *Supercond. Sci. Technol.*, 32:085001, 2019.

[177] M. Peurla, H. Huhtinen, Y. Y. Tse, J. Raittila, and P. Paturi. Structural properties of YBCO thin films deposited from different kinds of targets. *IEEE T. Appl. Supercond.*, 17:3608–3611, 2007.

[178] M. Malmivirta, L. Yao, H. Huhtinen, H. Palonen, S. van Dijken, and P. Paturi. Three ranges of the angular dependence of cirtical current of $BaZrO_3$ doped $YBa_2Cu_3O_{7-\delta}$ thin films grown at different temperatures. *Thin Solid Films*, 562:554–560, 2014.

[179] K. Develos-Bagarinao, H. Yamasaki, and K. Ohki. Flux pinning properties of YBCO/DyBCO multilayers. *J. Appl. Phys.*, 104:063907, 2008.

TURUN
YLIOPISTO
UNIVERSITY
OF TURKU

Painosalama, Turku, Finland 2024

ISBN 978-951-29-9779-4 (PRINT)
ISBN 978-951-29-9780-0 (PDF)
ISSN 0082-7002 (PRINT)
ISSN 2343-3175 (ONLINE)